WEAR AT HIGH SLIDING SPEEDS AND HIGH CONTACT PRESSURES

A PhD Dissertation
Presented to
The Academic Faculty

By

Matthew James Siopis

In Partial Fulfillment
of the Requirements for the Degree
Doctor of Philosophy in the
George W. Woodruff School of Mechanical Engineering

Georgia Institute of Technology
May 2015

WEAR AT HIGH SLIDING SPEEDS AND HIGH CONTACT PRESSURES

Approved by:

Dr. Richard W. Neu, Co-Advisor
George W. Woodruff School of Mechanical Engineering
Georgia Institute of Technology

Dr. Scott Bair
George W. Woodruff School of Mechanical Engineering
Georgia Institute of Technology

Dr. Richard S. Cowan, Co-Advisor
Georgia Tech Manufacturing Institute
Georgia Institute of Technology

Dr. Naresh Thadhani
School of Materials Science and Engineering
Georgia Institute of Technology

Dr. Jeffrey L. Streator
George W. Woodruff School of Mechanical Engineering
Georgia Institute of Technology

Date Approved: December 9, 2014

I dedicate this dissertation to my wife Lara.

ACKNOWLEDGEMENTS

First and foremost, I would like to acknowledge and thank my wife, Lara Siopis, for her never ending patience. Words cannot express how grateful I am for her support. Additionally I would like to thank my parents, James and Janet Siopis, along with my brother, Mike Siopis and sister-in-law, Caitlin Trainor for their continued support and encouragement of my academic endeavors.

I am grateful to my advisers Dr. Richard Neu and Dr. Richard Cowan for their guidance and mentorship as well as providing me with the freedom to explore the research areas presented in this dissertation. Additionally, I would like to thank the committee members Dr. Jeffrey Streator, Dr. Scott Bair, and Dr. Naresh Thadhani for their technical expertise.

I would also like to thank Steven Sheffield, J.D. Huggins, and Ben Loeffler for their insight and expertise in the area of fabrication which was essential to the completion of the research presented in this dissertation. I would like to acknowledge all past and present labmates / peers for their insightful conversations and support. They are, in no particular order, Robert Amaro, Mike Hirsch, Patxi Fernandez-Zelaia, Daniel Smith, Mike Kirka, Ben Adair, Matt O'Rourke, Brian Clark, Ashley Goulding, Kyle Brindley, and Andy Radzicki. Lastly, I would like to thank and acknowledge the Office of Naval Research, code 352, for their partial support of these research efforts.

TABLE OF CONTENTS

LIST OF TABLES

LIST OF FIGURES

NOMENCLATURE

α	Heat partition coefficient
α_T	Coefficient of thermal expansion ($°C^{-1}$)
a_c	Tribometer acceleration (m / s^2)
A	Heat dissipation constant ($MPa^{1/4} \cdot m / s$)
A_n	Nominal contact area (mm^2)
β	Dimensionless bulk heating parameter
B	Critical normalized wear rate
χ	Thermal diffusivity (m^2 / s)
C	Hugoniot experimental fit parameter (m / s)
c	Specific heat capacity ($J / kg \cdot K$)
ΔT	Temperature rise (°C)
δ	Geometric factor
E	Modulus of elasticity (GPa)
E_{in}	Heat energy input (J)
E_{gen}	Heat energy generated (J)
E_{out}	Heat energy removed (J)
$E_{storage}$	Heat energy stored (J)
$\tilde{F}$	Normalized contact pressure
f	Coefficient of friction
F_B	Wedge inertia load (N)
G	Geometric constant ($m^{-1/2}$)
G_N	Guider normal load (N)
G_S	Guider shear load (N)

H_o	Room temperature hardness (MPa)
h	Melt film thickness (m)
K	Thermal conductivity (W / m · K)
k	Nondimensional wear coefficient
Γ	Material property constant ($Pa^{-3/4}$)
λ	Turbulent viscosity constant ($Pa \cdot s^2 / m$)
L	Latent heat of fusion (kJ / kg)
l	Slider length (mm)
μ_G	Slider-guider coefficient of kinetic friction
μ_R	Wedge-ramp coefficient of kinetic friction
m_w	Wedge mass (g)
μ	Dynamic (absolute) viscosity (Pa · s)
N	Rotational speed (RPM)
Φ	Ratio of diffusion to dwell time
Ψ	Melt lubrication proportionality constant ($s / m \cdot MPa^{1/4}$)
P_N	Normal planar shock pressure (MPa)
Pe	Peclet number
q	Heat flux (W / m^2)
ρ	Mass density (kg / m^3)
r_o	Radius of a circular nominal contact area (m)
R_a	Arithmetic surface roughness (μm)
Re	Reynolds number
σ	Contact pressure (MPa)
σ_o	Reference contact pressure (MPa)
σ_r	Dimensionless pressure ratio

σ_{UTS}	Ultimate tensile strength (MPa)
s	Hugoniot experimental fit parameter
S_T	Thermal stress (MPa)
$S_{y,c}$	Compressive yield strength (MPa)
θ	Ramp angle (degrees)
τ_d	Dwell time (sec)
τ_h	Diffusion time (sec)
T	Temperature (°C)
T_∞	Temperature of the melt lubrication film (°C)
T_m	Melting point (°C)
T_o	Initial temperature (°C)
T^*	Equivalent metal temperature (°C)
t	Time (sec)
υ	Poisson's ratio
U	Shock velocity (m / s)
u	Particle velocity (m / s)
u_{guider}	Guider particle velocity (m / s)
u_{slider}	Slider particle velocity (m / s)
V	Volumetric wear (mm^3)
$\hat{V}$	Volume worn per distance slid (mm^3 / mm)
$\bar{V}$	Guider volume (m^3)
v	Slider velocity (m / s)
v_c	Critical slider velocity (m / s)
v_{gouge}	Gouge onset velocity (m / s)
v_m	1D melt velocity (m / s)

$\tilde{v}$	Normalized velocity
W	Normal contact load (N)
w	Slider width (mm)
$\widetilde{W}$	Normalized wear rate
W_N	Ramp normal load (N)
W_S	Ramp shear load (N)
x	Distance slid (mm)
ζ	Aspect ratio
z	Diffusion depth (m)

SUMMARY

The findings and analysis of the mechanical wear experiments presented in this dissertation provides the knowledge necessary to design more efficient and effective tribological systems under extreme sliding contact. A novel inertia loaded wedge experiment is employed at Georgia Tech utilizing a lab scale electromagnetic launcher to study mechanical wear of a 6061-T6 aluminum slider on a C110-H2 copper guider under conditions that have not been attained in prior studies. Sliding speeds in the range of 0 – 1,200 m/s and contact pressures between 100 – 225 MPa were achieved.

Three distinct wear regions were identified: plasticity dominated wear, severe plastic deformation and melt lubrication. The plasticity dominated wear region occurred at lower velocities, 0 – 800 m/s and is representative of localized plastic shearing. The severe plastic deformation wear region occurred at mid-range velocities between 800 – 1,000 m/s and is characteristic of thermal softening resulting in bulk shearing / plastic deformation. The melt lubrication region occurred at high velocities, >1,000 m/s and is representative of large scale melting.

Several different studies were conducted to explore the effects of pressure and velocity as well as guider mechanical and thermal properties on slider wear rates in the melt lubrication region. Normalized wear rates in the melt lubrication region were proportional to velocity. A critical velocity demarcated the shift from severe plastic deformation to melt lubrication and was found to decrease with increasing pressure. Additionally, the normalized wear rate in the melt lubrication region was correlated to the

product of velocity and pressure raised to the ¼ power, which is consistent with melt lubrication theory.

Different tribomaterial pairings were tested to investigate the effects of guider material properties on slider wear. For all tests the slider material is 6061-T6 aluminum. It was found that the mechanical properties of the guider had a negligible effect on slider wear in the severe plastic deformation and melt lubrication regions.

The effects of the guider thermal properties on slider wear in the melt lubrication region was investigated by selecting materials with vastly different volumetric thermal masses ($\rho \cdot c$). A guider material with a large volumetric thermal mass resulted in a high critical velocity and a larger heat partition coefficient. These findings indicate that the condition under which heat transfer occurs is highly transient.

Utilizing the results from the pressure – velocity and guider material property studies, a constitutive model was developed. The model is in a general form and is capable of predicting normalized wear rates in the melt lubrication region for a 6061-T6 aluminum slider at contact pressures between 100 – 225 MPa and peak velocities of 1,200 m/s for a variable guider material. The model can be used as a tool for designing more efficient and effective tribological systems subjected to these sliding conditions.

Using the new insights from this investigation a materials selection exercise for guider durability was conducted. For high sliding speeds it is beneficial to select a guider material with a large volumetric thermal mass, high ultimate tensile strength, low density, a high melting point, and high compressive strength with moderate ductility.

CHAPTER 1: Introduction

1.1 Overview

Tribology can be defined as the science and engineering of interacting surfaces in relative motion, which encompasses the topics of wear, friction and lubrication. Tribological interactions can be found in bearings, cams, gears, internal combustion engines, turbine engines, etc. These tribological interactions can incur wear which reduces performance, increases energy consumption, and over time may result in component replacement or failure. There are several different forms of wear that include, but are not limited to adhesion, abrasion, erosion, corrosion, and surface fatigue, all of which through surface engineering or the use of lubrication may be minimized. While the negative effects of many tribological interactions are well known, there are many essential tribological interactions that are commonly found in everyday life. For example the friction between your feet and the ground is necessary to walk, the friction between a brake pad and rotor is necessary to slow down a moving car, and the friction between a pencil and piece of paper allows you to write. While man has known about friction and lubrication for thousands of years, dating back to 3200 - 3500 BC [16], it wasn't until a 1966 report from the Committee of the British Department of Education and Science that the term tribology was actually coined [17].

Several studies have been conducted over the years to try and quantify the economic impact of wear. It was estimated in a 1966 report by Jost [17] that wear cost the U.K. approximately 1% of the GNP. In a 1977 study sponsored by ASME it was estimated that the energy cost to the U.S. associated with equipment failure due to wear was equal to 1.3% of the total U.S. energy consumption [18]. In 1996 Bhushan cited according to

some estimates that up to 6% of the GNP [19] was lost by neglecting tribology and more recently in 2005 it was reiterated by Jost that based on investigations conducted in the U.K., Germany, U.S., Canada, and China that the application of tribological principles and practices could yield a savings of 1.0 to 1.4% of the GNP for industrialized nations [20]. In all cases the economic impact on industrialized nations has been fairly consistent over the past forty plus years and as energy and material costs continue to rise, more attention must be drawn to extending the service life and efficiency of machinery to offset these costs. This means understanding the influence and role that tribology has on machinery and accounting for it through the development and implementation of materials, manufacturing processes, lubrication or simply minimizing surface interactions through design.

1.2 Research Background

1.2.1 Overview

The subject of this dissertation is on a specific facet of tribology related to lubrication by a melting solid. Melt wear, like most tribological interactions, is complex and encompasses all three aspects of tribology: friction, lubrication, and wear. In most applications it is typical to add lubrication to a system to reduce the coefficient of friction and remove heat in order to reduce component wear. In the case of melt wear, the sliding contact is initially unlubricated or dry and due to heat generated at the contact interface one or both of the sliding bodies may melt providing self-lubrication. If melt wear occurs at the contact interface it can be both beneficial and detrimental to a system's performance. The melt may be beneficial in the sense that it acts as a lubricant and reduces friction and detrimental in that one or both of the sliding solids is wearing away

which may result in a decrease in component performance or life and potentially result in failure. A well-known and studied system that exhibits this behavior is that of a skate on ice. Melt wear can also be commonly found in engineering systems that contain metal on metal contact in a high sliding speed and high contact pressure system. Typical engineering applications that experience high sliding speeds include, but are not limited to ultrahigh speed machining at the tool-chip interface (>300 m/s) [21], rocket sleds used for aerospace research and development at the slipper-rail interface (2,300 m/s) [22], large caliber guns at the projectile-barrel interface (1,500 m/s) [13], and lastly electromagnetic launchers at the armature-rail interface (2,500 m/s) [23].

1.2.2 Experimental Research

As previously mentioned one of the more commonly found self-lubricating tribological systems is that of a skate on ice [24] or ski on snow [25]. Initially it was hypothesized that pressure was the mechanism responsible for melting the ice. It wasn't until years later that the notion of friction as a major contributor was recognized [26, 27]. It has been shown through simple energy calculations that only a small fraction of the frictional heat generated at the contact interface is necessary to produce localized melting [11]. A series of experiments at the Research Station at Jungfraujoch in Switzerland using a ski on ice/snow apparatus tested the hypothesis that frictional heat is the primary mechanism responsible for melt wear. Several key findings were made and they are as follows: 1) The coefficient of kinetic friction is nearly independent of load, apparent area of contact and sliding speed, with the exception of high loads and low sliding speeds. 2) The low coefficient of kinetic friction value for a ski on ice is due to melting at the ski-ice interface. At lower temperatures melting only occurs at local areas of contact and at high

temperatures a more continuous layer of water develops. 3) The effect of temperature on friction is much greater for ice than that of metals. 4) The coefficient of kinetic friction increases as the temperature decreases. 5) The thermal conductivity of the sliding body influences the coefficient of kinetic friction. A slider with a higher thermal conductivity dissipates heat away from the contact interface at a higher rate resulting in a larger coefficient of kinetic friction, as shown in Figure 1.1. 6) Lastly, the role of thermal conductivity suggests that frictional heat plays a major role in the melt wear process.

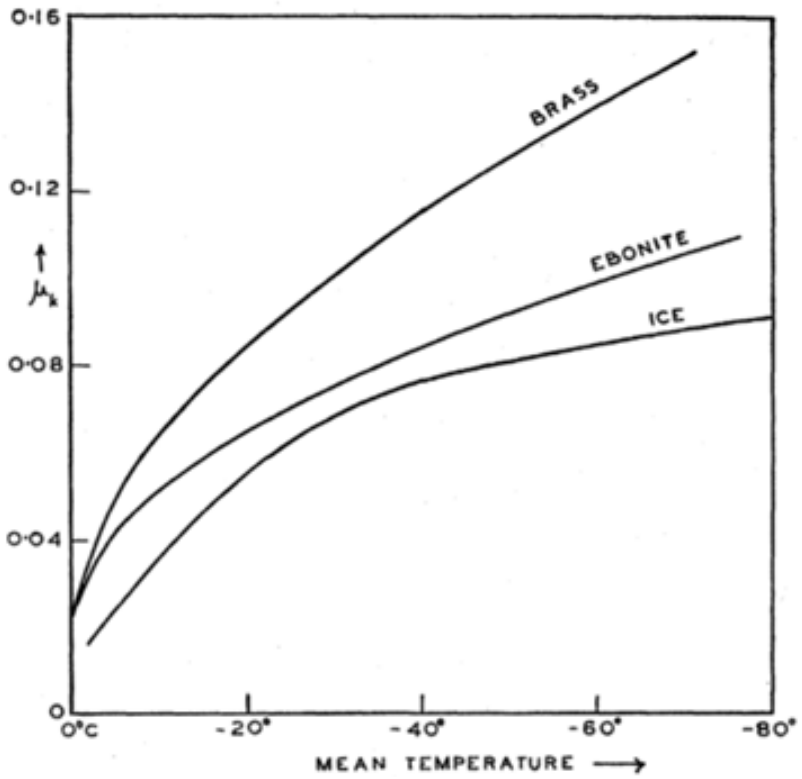

Figure 1.1 - Effects of temperature and ski material, thermal conductivity, on the coefficient of kinetic friction. The thermal conductivity of brass is greater than ebonite by three orders of magnitude [9, 11].

The melt wear study of a ski on ice is a practical experiment due to the reasonably low melting temperature of ice. However, for the case of metal on metal contact, where melting temperatures may be as much as two orders of magnitude higher than that of ice, has proven to be more difficult to study. An original experimental setup published by Bowden and Freitag [12], as shown in Figure 1.2, utilized a method developed for an ultracentrifuge [28] to study the behavior of two sliding metal surfaces at velocities up to 1,000 m/s. An electromagnet was used to vertically suspend and rotate a half inch steel

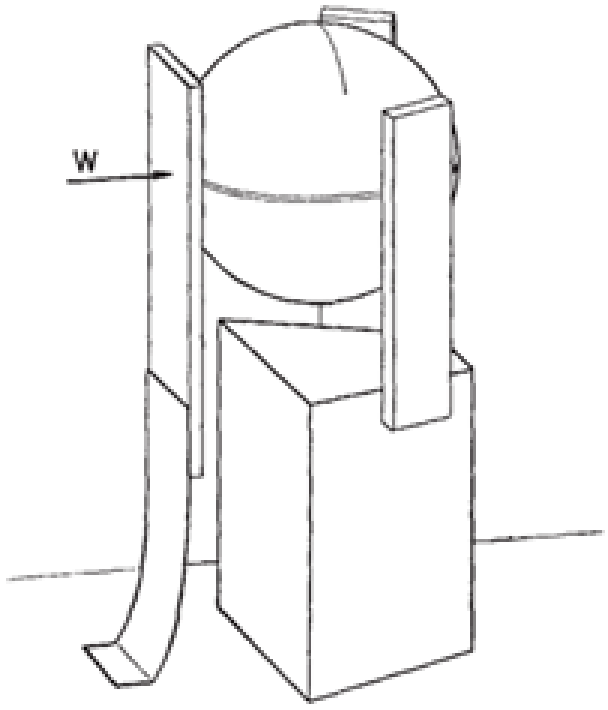

Figure 1.2 - A schematic of the electromagnet tribometer developed by Bowden and Freitag [12].

ball. Three vertical surfaces, two rigid and one free, were equally positioned around the ball. Upon releasing a spring the free surface presses the ball into the two rigid surfaces. The deceleration of the spinning ball under a known load was used to calculate the coefficient of friction. Friction coefficients and micrographs of the worn vertical surfaces for two different materials, copper and bismuth, using a steel ball bearing under a 20 gram load were collected. For both materials the coefficient of friction decreased towards a steady state value as the sliding speed of the ball increased, as shown in Figure 1.3.

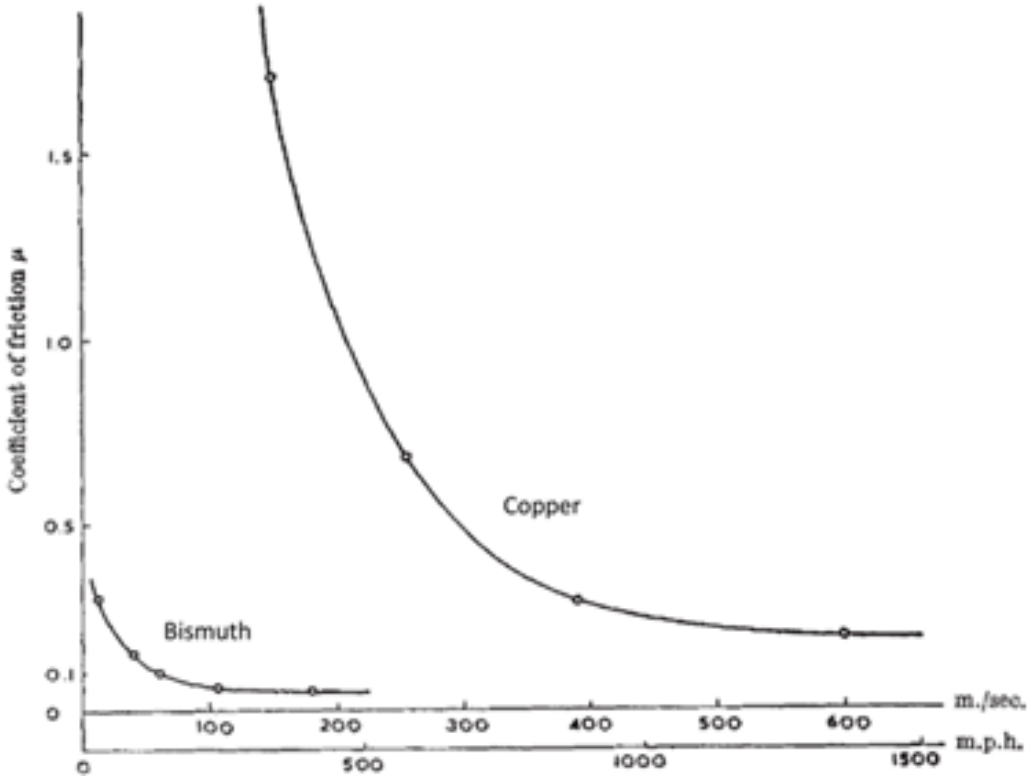

Figure 1.3 - Coefficient of friction vs. sliding speed for copper and bismuth on steel at high sliding speeds [12].

Bismuth which has both a lower melting temperature and thermal conductivity than that of copper reached a steady state coefficient of friction at a lower sliding speed than copper. An example of the molten metal splatter near the edge of a contact crater from a 300 m/s test using bismuth, as shown in Figure 1.4, provides evidence that regions of the contact interface are molten. From these tests it was observed that the coefficient of friction is not constant, but rather it decreases to a lower value at higher sliding speeds.

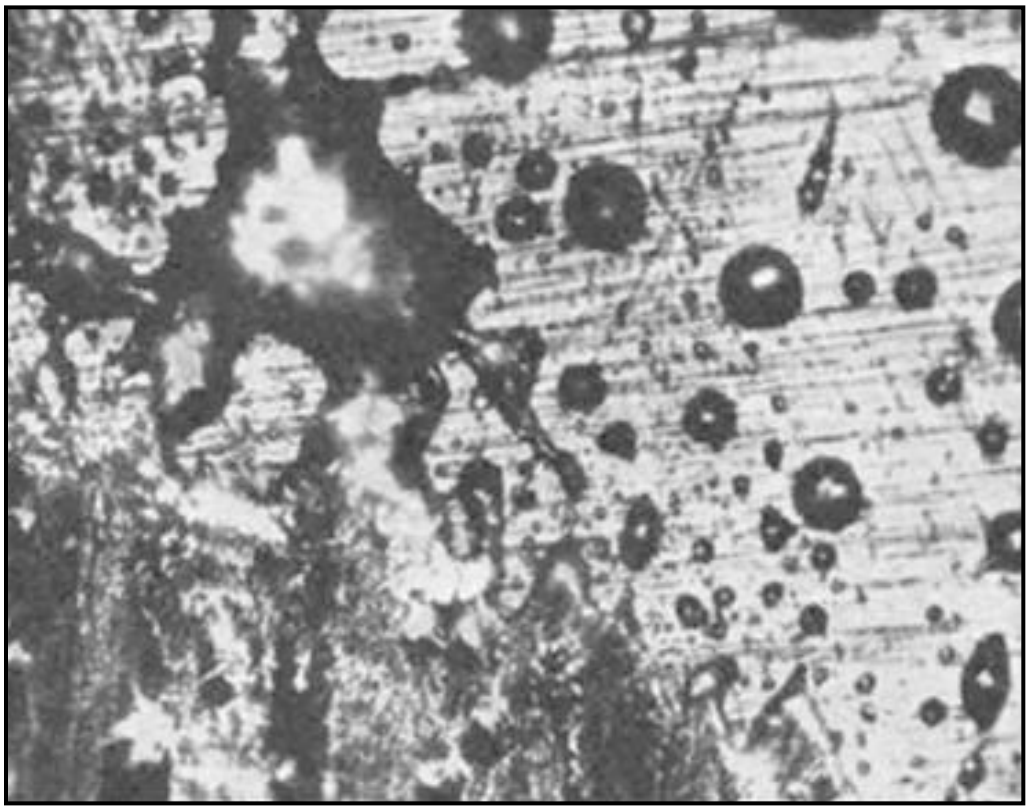

Figure 1.4 - High sliding speed (300 m/s) wear of Bismuth showing remnants of molten metal splatter [12].

The response of the coefficient of friction can be attributed to thermal softening or melting of localized regions of contact and based on the results no apparent large scale melting occurred.

In addition to the original copper and bismuth experiments a more complete set of results using the same electromagnet test apparatus was extended to include aluminum, aluminum alloys, antimony, molybdenum, tungsten, and diamond [29]. The majority of the experiments were conducted at loads in the range of 15 to 40 grams. The velocity range for each test differed depending on the material pair. A sensitivity analysis of the coefficient of friction versus load for copper was conducted at loads of 10 to 200 grams. The results showed that the coefficient of friction was independent of load under the sliding speeds tested. From these experiments it was observed that the coefficient of friction of metal on metal contact at high sliding speeds reduced to a relatively low value. This was consistent with previous work. The low coefficient of friction can be attributed to high temperatures at localized regions of contact. It was also shown, using heat transfer theory [30], that a very steep temperature gradient exists near the region of contact. For the case of copper it was calculated that at a distance of 1 μm below the contact surface the temperature reduced to 12% of the surface temperature, consequently creating a soft metal interface with low shear strength on a hard metal substrate. Limited knowledge or data of the stress-strain behavior of metals at high strain rates and high temperatures makes it exceedingly difficult to analyze the contact interface. From these experiments it was concluded that the response of the contact interface, that is friction and wear, is determined by the physical properties and the results suggest that adhesion was still valid under the conditions of the experiments.

A similar electromagnet test apparatus was developed to study wear at high sliding speeds and large loads [8]. An electromagnet was used to suspend and rotate a steel ball, except for this case the ball was dropped from a short distance onto a 30° inclined specimen, as shown in Figure 1.5. The apparatus was able to capture the normal and tangential loads on an inclined specimen through the use of a piezoelectric sensor. Two methods, one using contact forces and time and the other using geometry and deflection

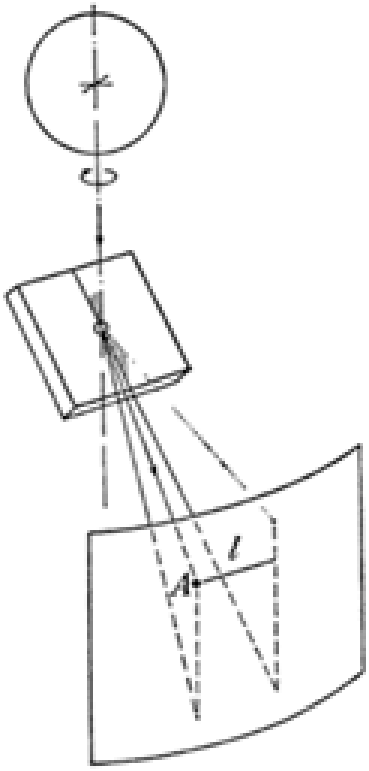

Figure 1.5 - High sliding speed impact experimental apparatus used by Bowden and Persson [8].

of the ball, were used to calculate the coefficient of friction. This new method provided a means to study high sliding speeds, up to 700 m/s, at relatively large loads, in the kilogram range, two orders of magnitude higher than the previous experimental technique. The experiments included the use of a steel ball against several different materials of interest, of them bismuth was revisited. The wear marks of the bismuth specimen from the impact spinning ball test were similar to those produced from the vertical flat plate spinning ball test for velocities up to 200 m/s. A comparison of the evolution of the coefficient of friction as a function of sliding speed for the two different techniques is compared in Figure 1.6. The solid line represents the results of the vertical flat plate, spinning ball test at low loads, 0.008 kg, up to 200 m/s, and the circles and triangles represent the impact spinning ball test at 0.5 kg and 6 kg at velocities approaching 600 m/s. The results show good correlation between the two different tests at low speeds. For the impact spinning ball test at high speeds the appearance of the wear marks shows a rapid increase in the size and a more prominent smearing of the material with increased sliding speed. The smeared appearance of the wear marks at high sliding speeds combined with the molten metal splatter near the trailing edge provided evidence that at high speeds a molten layer was present and melting had occurred on a large scale.

From the experiments with bismuth, a hypothesis that melting on a large scale is primarily dependent on the melt temperature and thermal conductivity of the metal was developed. The hypothesis was tested through several experiments over a range of sliding speeds using Wood's alloy, which has a melting temperature of 65°C and a thermal conductivity of 0.032 cal cm^{-1} s^{-1} $°C^{-1}$, and bismuth, with a melting temperature of 271°C and a thermal conductivity of 0.016 cal cm^{-1} s^{-1} $°C^{1}$. The comparison of Wood's alloy to

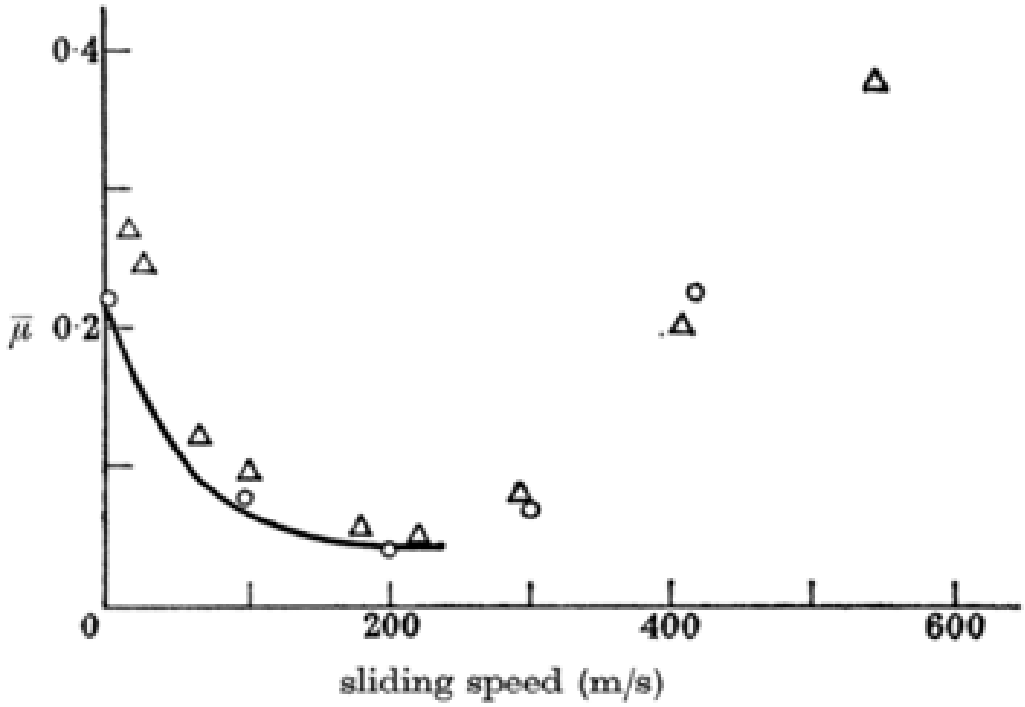

Figure 1.6 - The evolution of the coefficient of friction for steel on bismuth as a function of sliding speed for two different test techniques [8, 9].

bismuth is shown in Figure 1.7. Additional experiments were conducted using steel on lead, steel on tin, steel on silver nitrate, steel on copper, and steel on steel. The melting temperature and thermal conductivities of these materials is summarized in Table 1.1. The material response in both appearance and coefficient of friction of Wood's alloy, lead, tin, and silver nitrate at high sliding speeds was similar to that of bismuth. Each of the materials experienced a transition velocity at which the coefficient of friction began to increase. This speed marks the formation of large scale melting and can be correlated to the material melting temperature. The transition velocities for bismuth, Wood's alloy,

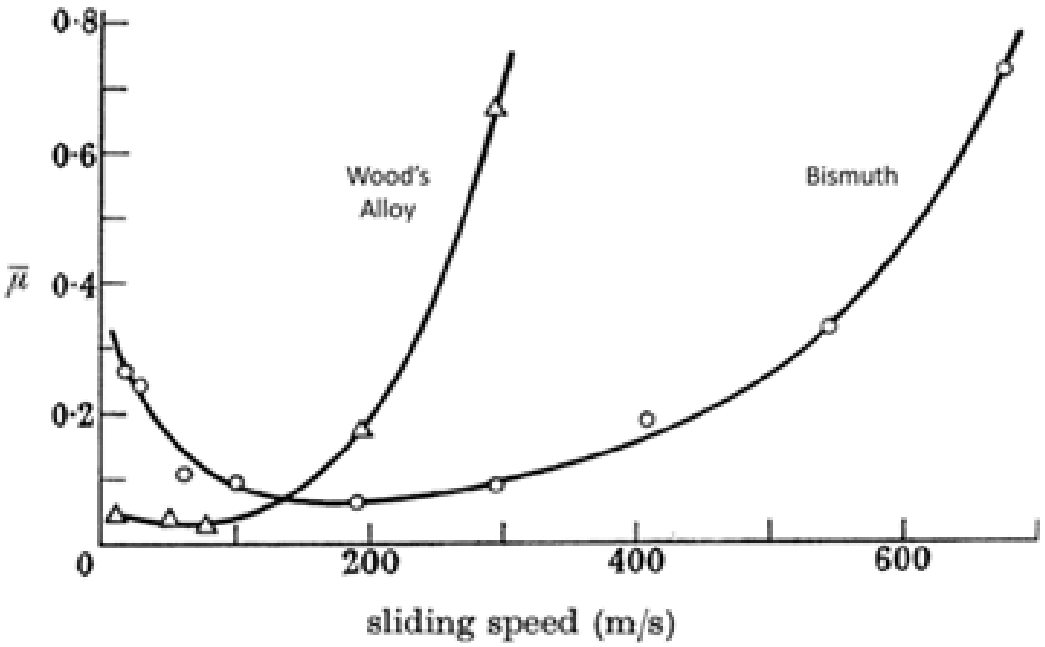

Figure 1.7 - A comparison of the coefficient of friction for steel on Wood's alloy (triangles) and steel on bismuth (circles) [8].

Table 1.1 - Melting point and thermal conductivity properties for materials tested using the impact spinning ball test.

	Melting Point (°C)	Thermal Conductivity (cal cm^{-1} s^{-1} $°C^{-1}$)
Bismuth	271	0.016
Wood's Alloy	65	0.032
Lead	328	0.082
Tin	232	0.145
Silver Nitrate	210	0.002
Copper	1080	0.910
Steel	1500	0.100

lead, tin, and silver nitrate follow the trend that lower melting temperatures result in lower transition speeds. For steel on copper and steel on steel experiments the transition velocity was never achieved due to the higher melting points and velocity limitations of the experimental setup. Instead thermal softening or melting occurred only at localized regions of contact leading to low coefficient of friction values, as shown in Figure 1.8. An alternative or modified test configuration capable of higher sliding speeds is necessary to explore the large scale melting region for copper and steel. It was concluded that a continuous molten film developed over the nominal area of contact for the lower melting temperature tribomaterials. This differed from previous experimental results

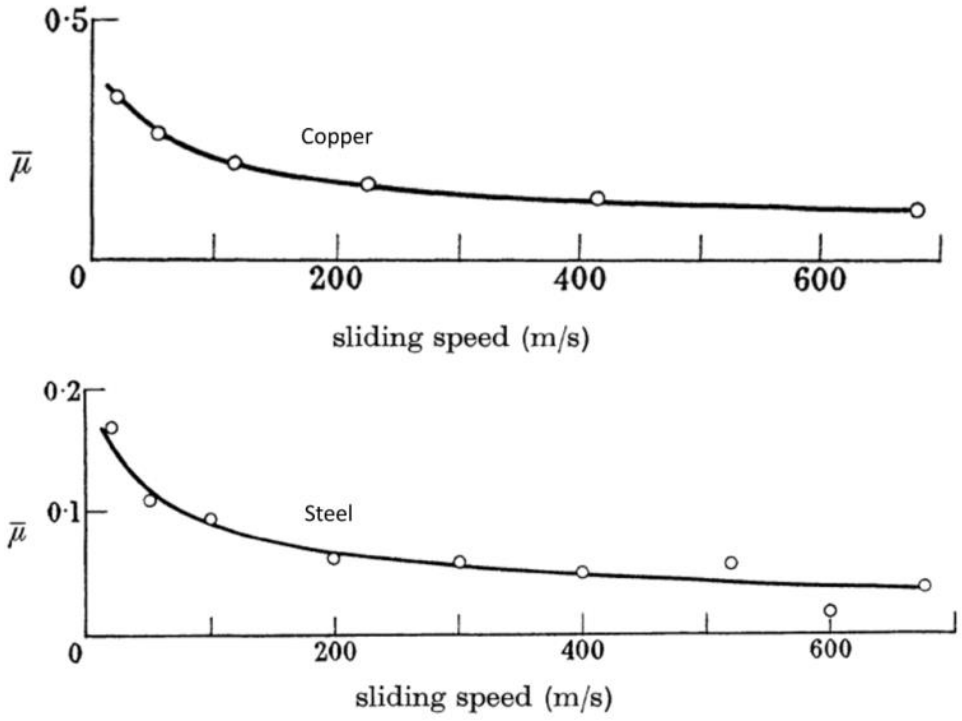

Figure 1.8 - The response of coefficient of friction for copper on steel and steel on copper using the impact spinning ball test [8, 9].

where thermal softening or melting only occurred at localized regions of contact. For a continuous molten metal film the resistance to sliding is influenced by the shearing of that film and heating at the contact interface, which is primarily viscous in nature and consequently the heat generated increases with increasing velocity resulting in accelerated wear rates.

There have been many different test apparatuses developed and used to study tribological properties of different material pairs. Many one of a kind test apparatuses, like the aforementioned vertical flat plate and impact spinning ball, were developed specifically to replicate a component configuration and service condition. Some of the most commonly used tribological test apparatuses include the pin-on-disk, pin-on-flat, pin-on-cylinder, thrust washers, pin-into-bushing, rectangular flats on a rotating cylinder, crossed cylinders, and four ball [14]. The control factors for each of these apparatuses, such as geometry, load, velocity, etc. are defined based on design and equipment limitations. Of the apparatuses listed, the most commonly used apparatus to study wear at high sliding speeds is the pin-on-disk apparatus.

Sternlicht and Apkarian conducted a set of experiments to study electrical sliding contacts at high sliding speeds using a pin-on-disk apparatus [31]. This work differed from previous melt wear work in that the combined effects of friction and Joule heating at the contact interface were under investigation. Test conditions included electrical current densities and velocities up to 930 MA/m^2 and 610 m/s, respectively. Given the conditions of the experiments it was expected that a molten film would be present and viscosity, rather than elasticity, would be used to characterize the deformation process. Experiments and analysis showed that the surface temperatures were high enough to melt

at least one of the sliding materials and that a molten layer existed. It was assumed that the molten layer was continuous and in doing so hydrodynamic theory was applied to calculate wear rates, which proved to be within reason when compared to experimental results.

Earles and Kadhim [32] also utilized a pin-on-disk apparatus to study wear for a steel pin, steel disk material pair at velocities up to 200 m/s. Like previous research, a low coefficient of friction was observed at high sliding speeds. It was shown from experiments that the coefficient of friction was proportional to $N^{1/2}U$, where N is normal load and U is velocity. The term $(N^{1/2}U)^n$ was first introduced by Bowden and Thomas [33], where n is one for small values of $N^{1/2}U$ and n is ½ for large values. It can be implied that the term $(N^{1/2}U)^n$ is proportional to the average surface temperature at the contact interface. For large values of $N^{1/2}U$ there was microscopic evidence that a viscous layer had been smoothed out across the trailing edge of the pin and as $N^{1/2}U$ increased the smooth shiny layer eventually spanned across a larger portion of the contact interface. It was concluded that the contact was lubricated due to localized melting, resulting in a low coefficient of friction.

The most complete set of pin-on-disk experimental results at high sliding speeds, up to 550 m/s, was published by Montgomery [13]. The experimental data was compiled from several experiments funded by the U.S. Army over a span of ten years. The experiments were conducted to gain a deeper understanding of the mechanism responsible for wear in rotating bands of projectiles for large caliber cannons. A frictional rate of heat generation parameter in the form of fPV, where f is the measured coefficient of friction, P is applied pressure and V is the sliding speed, was used to characterize the

heat generated at the contact interface and to correlate it to wear rates. Several pin materials, gilding metal, copper, projectile steel and annealed iron on a gun steel disk were thoroughly investigated and several miscellaneous materials, copper-nickel alloy, zinc, aluminum, nylon, and nickel were tested to a lesser extent. The results of these experiments are similar to the aforementioned high speed experiments in that the coefficient of friction decreased with increasing sliding speed. This meant that increasing the frictional rate of heat generation, which subsequently includes velocity, resulted in a decreasing coefficient of friction value. From the experimental data the wear rates for the set of materials tested were found to be proportional to the reciprocal of the melting point, as shown in Figure 1.9. The conclusion was drawn that wear at high sliding speeds is due to surface melting which acts as a lubricant and that the wear rate is predominantly a function of melting temperature, while thermal conductivity may have a secondary effect.

Lastly, a more recent set of novel experiments developed by Stefani and Parker [4] at the Institute for Advanced Technology (IAT) at the University of Texas were conducted to study mechanical wear. The experiments utilized a medium caliber electromagnetic launcher (EML) to obtain high sliding speeds and high contact pressures. Several tests were conducted using aluminum wedges on copper rails with similar sliding speeds and different contact pressures. Wear results from the experiments for five different contact pressures are shown in Figure 1.10. Three key findings from the test include that wear as a function of sliding distance appears to be nonlinear, measurable wear does not begin until 50 cm of travel, at which point the sliding speed is approximately 1,000 m/s, and the wear rate increases with increasing contact pressure. Similarities may be drawn between

the critical velocity at which the wear became significant in these tests and the critical velocity from the aforementioned experiments at which the coefficient of friction began to steadily increase. The experimental methodology that was used in the IAT experiments is the one employed in the GT minor caliber EML as will be discussed in a later section of this dissertation.

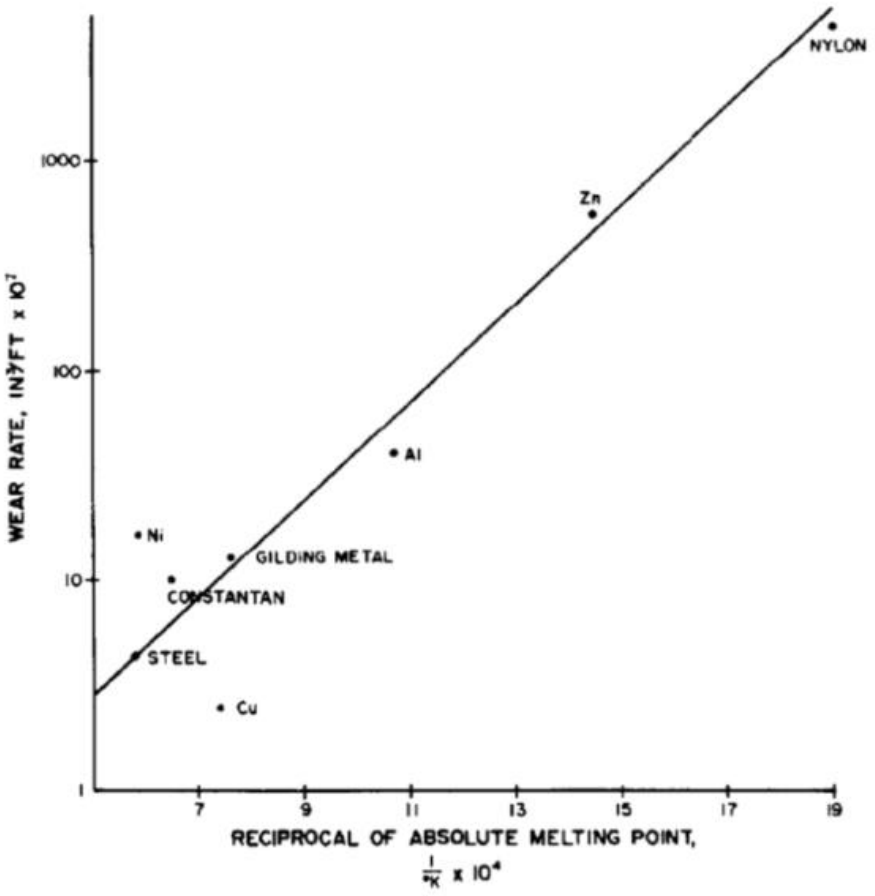

Figure 1.9 - Wear rate as a function of the reciprocal of the melting point of various materials for a fixed rate of heat generation [13].

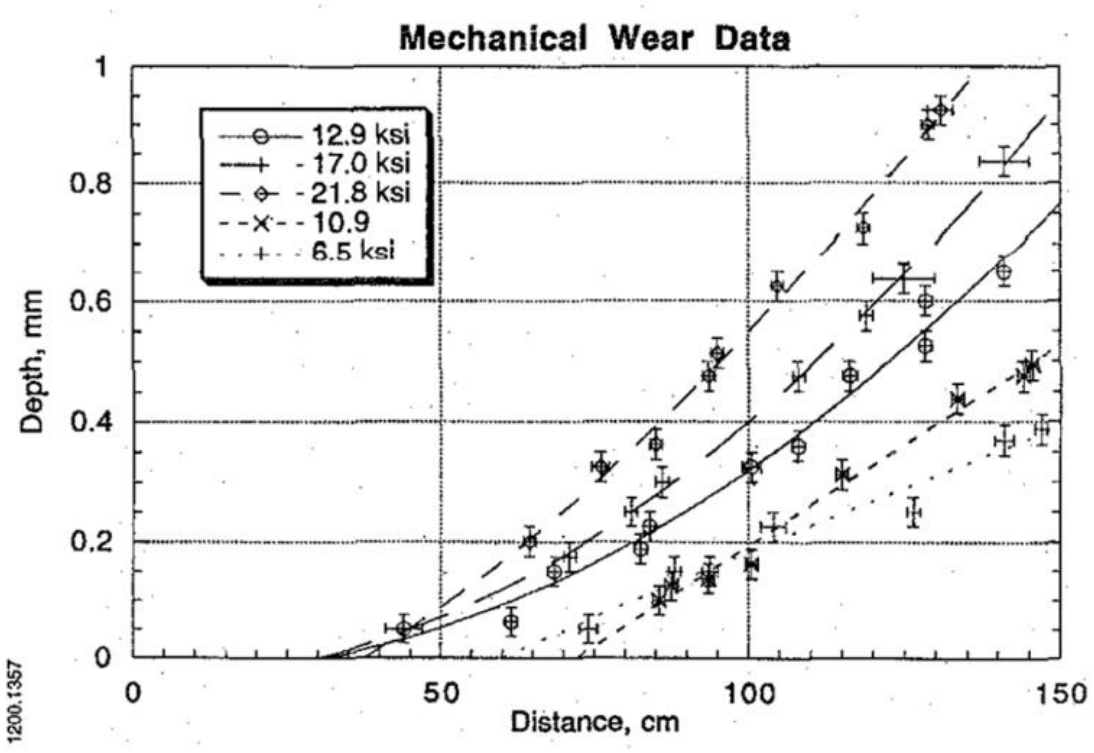

Figure 1.10 - Mechanical wear data from high sliding contact experiments to study the effects of contact pressure on wear [2, 4].

1.2.3 Wear Mechanism Maps

A broad approach to understanding wear mechanisms and their interactions is through the use of wear mechanism maps. Wear mechanism maps are an attempt to provide order by defining the dominant wear mechanisms, trends, and models for a given tribomaterial pairing. Several decades worth of wear data characterizing the dry sliding behavior of steel on steel was compiled and organized by Lim and Ashby [10] using this novel approach. A wear mechanism map for the dry sliding behavior of steel on steel as a

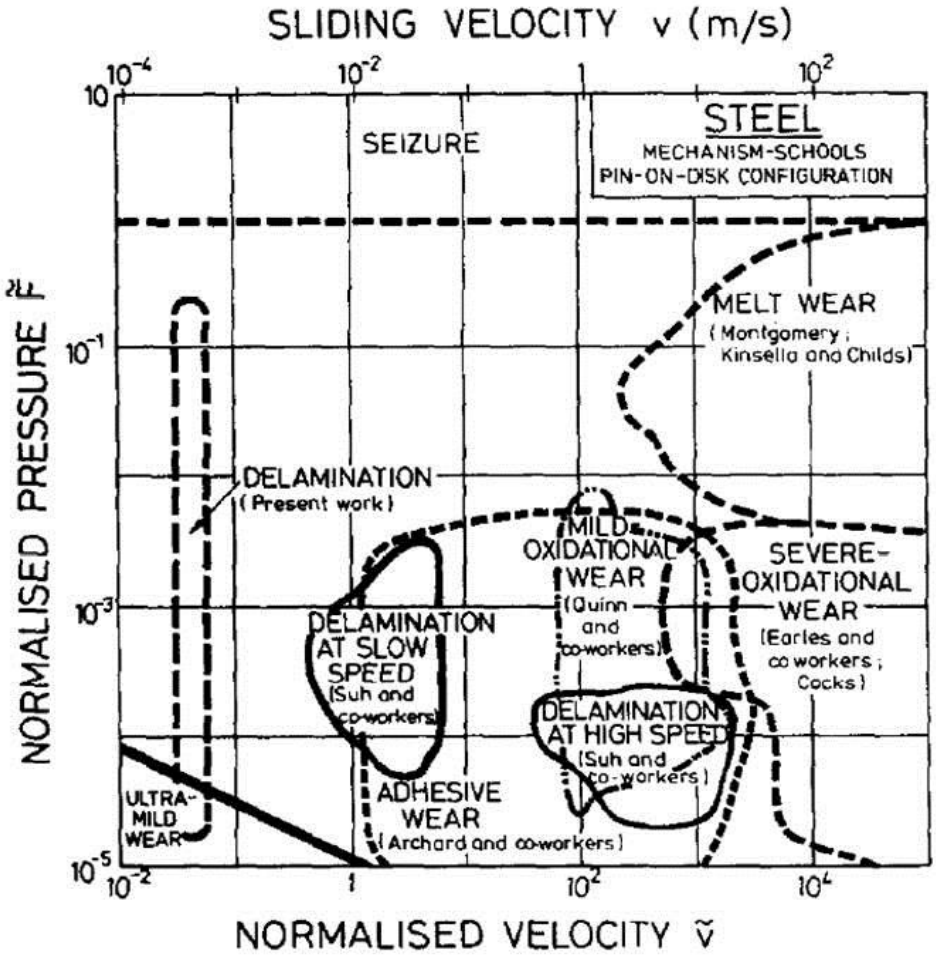

Figure 1.11 - Wear mechanism map for the dry sliding of steel on steel [10].

function of normalized pressure and velocity is shown in Figure 1.11. The different mechanisms are identified based on compiled experimental data and observations. Normalized pressure is defined

$$\tilde{F} = \frac{\sigma}{\sigma_{UTS}} \tag{1.1}$$

where σ is the nominal contact pressure and σ_{UTS} is the room temperature ultimate tensile strength of the slider material. Normalized velocity is defined

$$\tilde{v} = \frac{vr_o}{\chi} \tag{1.2}$$

where v is the slider velocity, r_o is the radius of a circular nominal contact area, and χ is the thermal diffusivity.

Regions of different wear mechanism schools were identified and physical wear models based off of the dominant wear mechanism for each region were developed. These physical models were fitted or calibrated to the empirical data within each wear mechanism region. Distinct boundaries between wear mechanism regions were defined and lines of constant normalized wear rates, based on the wear models, are shown in Figure 1.12. Normalized wear rate is defined

$$\tilde{W} = \frac{\hat{V}}{A_n} \tag{1.3}$$

where $\hat{V}$ is the volume worn per distance slid and A_n is the nominal contact area. The region of interest under high sliding speeds and high contact pressures is the melt wear region and beyond. The upper bound or right edge of sliding velocity, from the actual experimental data for the melt wear region is 550 m/s. Utilizing the wear mechanism map for dry sliding behavior of steel on steel for sliding velocities greater than 550 m/s would be an extrapolation and caution is required. Under high sliding speeds and high contact

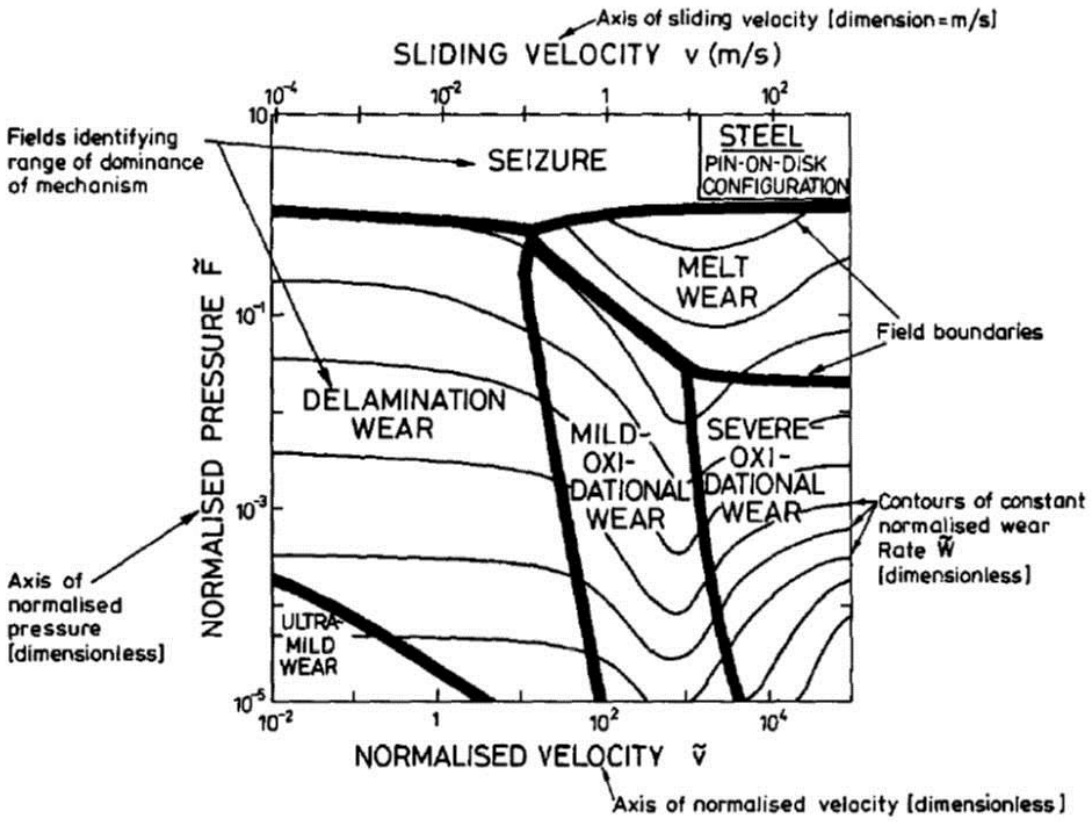

Figure 1.12 - Wear mechanism map for dry sliding of steel on steel with empirically fit wear models with contours of constant wear coefficients [10].

pressures, melting of the sliding solid can occur locally (melt wear) or on a large scale (melt lubrication). Current wear mechanism maps do not distinguish between these mechanisms. Extrapolation of the existing wear mechanism map beyond the upper bound could lead to improperly characterizing the type of wear and the normalized wear rate. There is an inherent need for additional data to extend the existing wear mechanism maps and develop new physical wear models to properly categorize regions with sliding velocities greater than 550 m/s.

1.2.4 Theoretical Wear Modeling

Experiments have shown that under high sliding speeds and high contact pressures there is evidence that melting of one of the solids provides lubrication, albeit locally or on a large scale at the contact interface. If the melting of the sliding solids occurs locally it is referred to as melt wear and if it occurs on a large scale it is referred to as melt lubrication. To this point the investigation into the topic of melt wear / lubrication has largely been experimental and theoretical modeling has been rather limited. One of the earlier theoretical models published by Wilson [34] is based on hydrodynamic lubrication theory derived from the Reynolds equation and several assumptions. Wilson analyzed both the case of the melting slider and guider. From his analyses he made the conclusion that these hydrodynamic systems are capable of supporting large loads and providing low friction. Additionally, both the load supporting capability and friction are proportional to the square root of the sliding speed. It was noted that further work was needed to address heat transfer losses at the contact interface, temperature dependent viscosity properties, and the effects of material softening. Wilson's model was altered by Bicego et al. [35] to include both viscous dissipation and heat conduction through the melt lubrication film.

Conventional hydrodynamic theory based on two parallel plates with relative motion has been used as the basis for prior models. Stiffler [36] was one of the first to propose that the melting slider mass was capable of supporting large loads under the conditions of melt lubrication. The model is based on the same premise as that used to model porous bearings. It was concluded that for high sliding speeds, those specifically related to a copper slider on a steel guider, that the temperature differential across the melt lubrication film is negligible and is approximately the melt temperature of the slider.

Additionally, changes in the melt lubricant film density were not probable and therefore the conditions necessary to form a thermal wedge were unlikely, and the rate of heat energy dissipated via "squeeze film" is negligible when compared to that of Couette flow. The theoretical coefficient of friction results from Stiffler's model compared well to experimental data. The wear model is defined as follows

$$\hat{V} = \frac{Wh^3}{l^2 \mu v \delta} \tag{1.4}$$

where $\hat{V}$ is the worn volume per distance slid, W is the load, h is the melt film thickness, l is the length of the slider, μ is the dynamic viscosity, v is the slider velocity, and δ is a geometric factor equal to one for large ratios of slider length to width. The melt film thickness h is defined as follows

$$h = \left\{ \frac{(\mu v l)^2 \delta}{\left[\rho\sigma\left(L + c(T_m - T_o)\right)\right]} \right\}^{\frac{1}{4}} \tag{1.5}$$

where ρ is the density, σ is the contact pressure, L is the latent heat of fusion, c is the specific heat, T_m is the melt temperature, and T_o is the initial temperature. The model can also be represented as a 1D melt velocity, v_m, in the form

$$v_m = \frac{\mu^{\frac{1}{2}}\sigma^{\frac{1}{4}}v^{\frac{3}{2}}}{\rho^{\frac{3}{4}}l^{\frac{1}{2}}\delta^{\frac{1}{4}}[L + c(T_m - T_o)]^{\frac{3}{4}}} \tag{1.6}$$

A more general wear model published by Lim and Ashby [10] was developed based on steel pin and steel disk data compiled from melt wear experiments. Observations from these experiments indicated that the wear incurred was due to melting of one or both of the sliding contacts. From experimental data a wear model was developed. The melt wear model utilizes the 1D heat equation, considers frictional heat as the sole heat source, and partitions the heat between the slider and guider based on thermal properties and sliding speed. Heat transfer via conduction was incorporated into the model, while convection and radiation were neglected. Additionally it was assumed that all the melted material was ejected from the contact interface and that the melt provides lubrication, which results in low coefficient of friction values at high sliding speeds. Agreement between the melt wear model and the experimental data is reasonable. Unlike previous models, the melt wear model only considers frictional heat using coefficients of friction acquired from experimentation. Viscous heating due to the shearing of the liquid film is not considered. Lim and Ashby's melt wear model is as follows

$$\widetilde{W} = \left(\frac{T_m - T_o}{T^*}\right)\frac{H_o}{L}\frac{1}{\beta\tilde{v}}\left[\alpha f\tilde{F}\tilde{v}\frac{T^*\beta}{(T_m - T_o)} - 1\right] \tag{1.7}$$

where $\widetilde{W}$ is the normalized wear rate, T_m is the melting temperature, T_o is the initial temperature, T^* an equivalent metal temperature, H_o is the room temperature hardness of the metal, L is the latent heat, β is the dimensionless bulk heating parameter, $\tilde{v}$ is the normalized velocity, α is the heat partition coefficient, f is the coefficient of friction, and $\tilde{F}$ is the normalized pressure.

Stefani and Parker [4] revisited wear at high sliding speeds through a series of novel mechanical wear experiments using a lab scale EML. The work was spurred by the need to better understand the influence of mechanical and electrical heat generation at the contact interface of EML components. It was noted that the majority of published experimental data was at velocities below 100 m/s, well outside the operating range observed in EMLs. Additionally their work was unique in the sense that at the time the majority of the emphasis in EML component wear had been placed on the electrical component of the sliding contact. Several wear models [37-40] focusing on Joule heating as the primary heat source had been developed to predict the transition from non-arcing to arcing electrical contact. The mechanical wear experiments they conducted provided new data for melt lubrication modeling. Several melt lubrication models were developed following these experiments, most of which were extensions of existing models. One of the first models to reinvestigate melt lubrication was a thermal hydraulic model [41] based on the modeling done by Stiffler [36]. The thermal hydraulic model differed from Stiffler's in that it assumed a portion of the melt film solidified under the slider. The results were able to predict reasonable melt velocities, but lacked the dependence on pressure and velocity that was observed in experiments. Several observations were made

from the model. The first is that the slider melt temperature is reached at approximately 700 m/s, but it isn't until 1000 m/s that a quasi-steady-state molten film is achieved. Reduced heat transfer to the guider, a higher melt viscosity, and a higher film thermal conductivity provided a better correlation to experimental data. It was concluded that film solidification under the slider did not need to be captured in the model. A follow up melt lubrication model [42] was developed that incorporated the effects of turbulence on the laminar viscosity term. The results significantly over predicted the melt velocity and were strongly dependent on the slider velocity and less dependent on contact pressure. These trends tend to disagree with those observed from experiments. It was concluded that a thermal hydraulic model was not adequate in modeling high velocity, high pressure, mechanical wear and that this may be the result of another physical process such as viscoplastic heating or some complex combination of melting and shearing of the slider material.

More recently, Wei and Batra [43] modeled and simulated high speed sliding and addressed thermal softening, melting, and melt lubrication, as it pertains to slider wear. Two heat sources, frictional and plastic dissipation, were considered in an attempt to better understand the contribution of each towards the temperature rise in the slider and subsequent melting. Additionally, like the aforementioned models they applied melt lubrication theory to develop a model capable of predicting both the melt film thickness and melt velocity. Several findings or conclusions were made. The first is that two boundary layers exist at the slider-guider interface, a deformation layer and a thermal layer. The second finding is that for large values of heat flux at the slider-guider interface, friction or viscous dissipation, rather than plastic dissipation, is the main

contributor to the local temperature rise. Finally, it's difficult to achieve steady-state melt lubrication and the process itself can best be described by the transient melt lubrication solution. It was recommended that the strength of the slider material near its melting temperature needs to be considered. Additional experimental data is required to gain a deeper understanding of the influence of the slider and guider thermal and mechanical properties on the wear process.

CHAPTER 2: Experimental Methodology

2.1 Experimental Overview

The experiments conducted at Georgia Tech under high sliding speeds and high contact pressures are based off of wedge experiments conducted at the Institute for Advanced Technology (IAT) at the University of Texas [4]. A similar approach with two inertia loaded wedges was been developed and employed in the Georgia Tech minor caliber electromagnetic launcher (EML). The Georgia Tech EML system is composed of a breech, containment and catch tank, as shown in Figure 2.1, and electric power supply, as shown in Figure 2.2 [44]. The breech provides the physical connection between the power supply and the rails. The containment is the steel laminate structure comprised of two halves that are clamped together with high strength steel bolts. Inside the containment resides the bore. The bore consists of two C110-H2 copper flat rails, and two

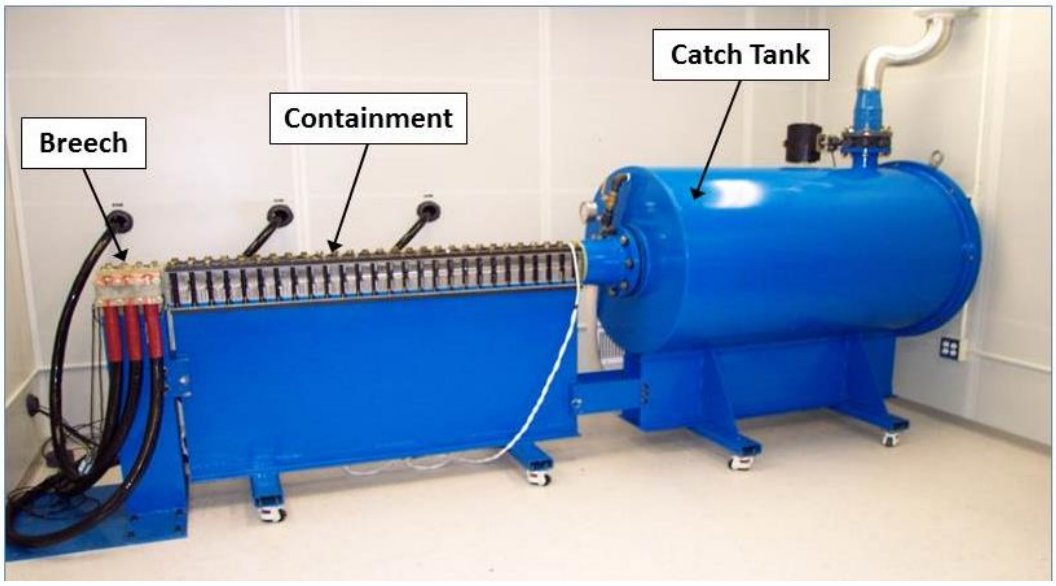

Figure 2.1 - Georgia Tech lab scale electromagnetic launcher.

sidewall G-10 glass composite insulators. The bore configuration is a 14.0 millimeter by 12.5 millimeter rectangle, and the overall length of the containment is 1.56 meters long. A cross-sectional view of the Georgia Tech minor caliber EML bore is shown in Figure 2.3. The catch tank is constructed out of steel and contains a one foot long steel slug at the back of the tank. The tank itself is loaded with cloth dunnage as to provide a soft

Figure 2.2 - Georgia Tech six module, capacitor bank electrical power supply.

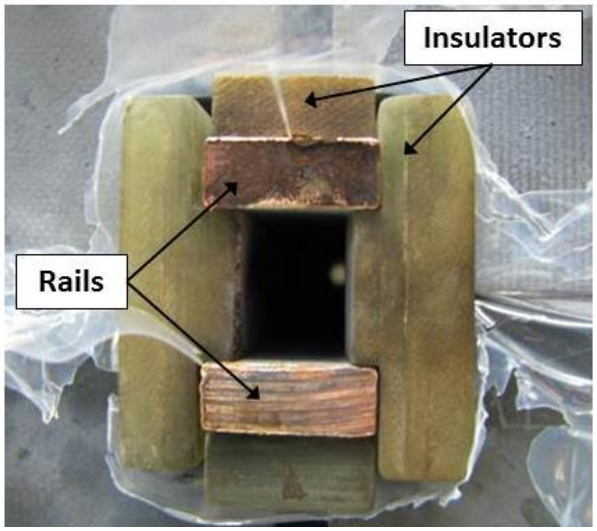

Figure 2.3 - Georgia Tech lab scale electromagnetic launcher bore.

catch for retrieval of the launch packages. The power supply consists of six independently triggerable sub modules. Each sub module contains five 210 μF capacitors giving each module the capability to store 17.1 kJ at 5.7 kV for a total stored energy of 0.1MJ.

The actual operation of the Georgia Tech minor caliber EML is based on the physics of a single turn inductor. An armature, which acts as a fuse, is placed between the rails to complete the electrical circuit. The power supply stores the electrical energy and when discharged it generates a pulse of electrical current. The electrical current travels down one rail, crosses over the armature and returns down the opposing rail, as shown in Figure 2.4. A magnetic field, created from the pulsed electrical current, encircles each of

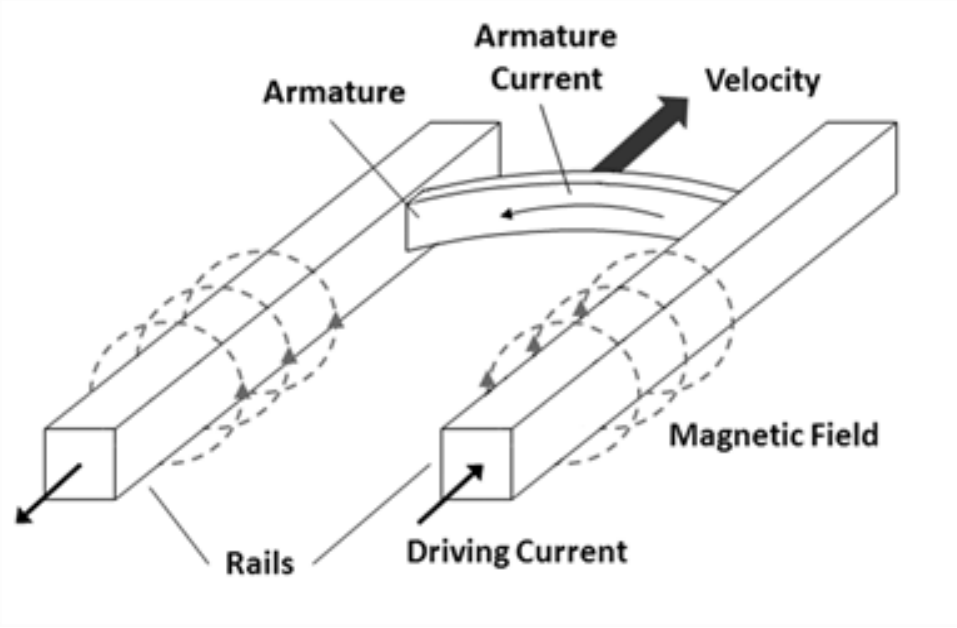

Figure 2.4 -Schematic of an electromagnetic launcher (EML).

the conductive rails. The interaction of the electrical current and magnetic field generates Lorentz forces that try to push the rails apart and accelerates the armature down the length of the rails [45]. Typical electrical currents are between 250-300 kA, producing velocities on the order of 1,000 m/s. The total launch duration is approximately 2 milliseconds long.

2.2 Experimental Setup

The method developed using the Georgia Tech EML is capable of studying mechanical wear, with a negligible electrical component, at sliding speeds up to 1,200 m/s and contact pressures up to 225 MPa. The methodology involves modifying the sidewall insulators as shown in Figure 2.5. The sidewall insulators are fabricated out of G-10 glass fiber composite and have been modified with a 7.57 millimeter deep channel milled down the length of the insulator. The channel is able to accommodate a 6.35 square millimeter bar, 1.56 meters in length. The bar, embedded in the insulator, is referred to as the guider and the insulator design provides the flexibility of interchanging guider materials as desired.

The tribo-slider is shown in Figure 2.6 and has a mass of approximately 10 grams. The aft end of the tribo-slider, referred to as the armature, is fabricated out of 6061-T6 aluminum and is used to propel the tribo-slider down the rails and out of the containment. A ramp with a 25 degree angle from centerline, fabricated from G-10 is used to translate the inertia load, generated from the mass of the wedge and the acceleration of the tribo-slider, into a normal contact load on the guider. Each of the wedges contains a wear tab, also referred to as the slider, which wears and deposits material onto the guiders. The wedges are machined out of 6061-T6 aluminum bar stock, can accommodate a slider

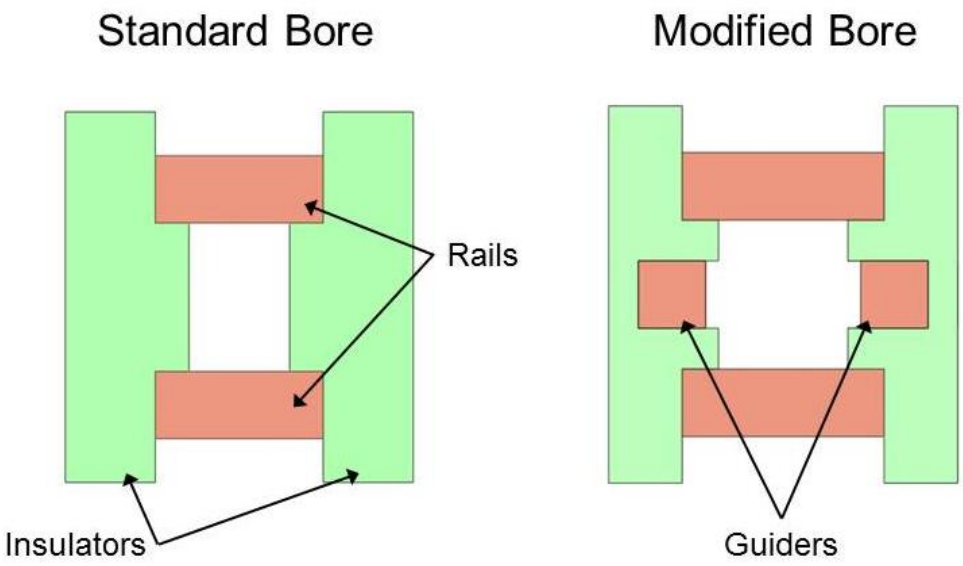

Figure 2.5 - Cross-sectional view of the standard (left) and modified (right) GT minor caliber EML bore.

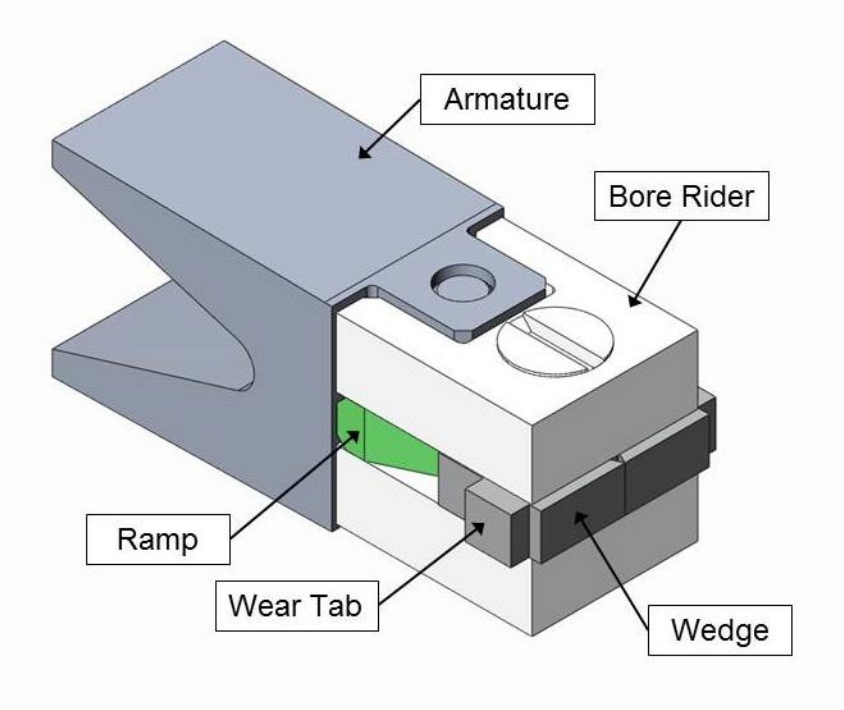

Figure 2.6 -A solid model of a fully assembled tribo-slider.

contact area up to 3.18 square millimeters and provide the flexibility of selecting different tribomaterial pairings as desired. Finally, two nylon bore riders are used to support and align the wedges during loading and prior to launch. An overhead view of a loaded tribo-slider with the bore riders and sidewall insulators removed is shown in Figure 2.7. Additionally, a half open view of the EML bore with a modified sidewall insulator and loaded tribo-slider is shown in Figure 2.8.

A key design attribute of the modified bore and tribo-slider is that it provides electrical isolation of the guiders and wedges from the top and bottom rails through the G-10 sidewall insulators and G-10 ramp. The G-10 electrically isolates the guiders and

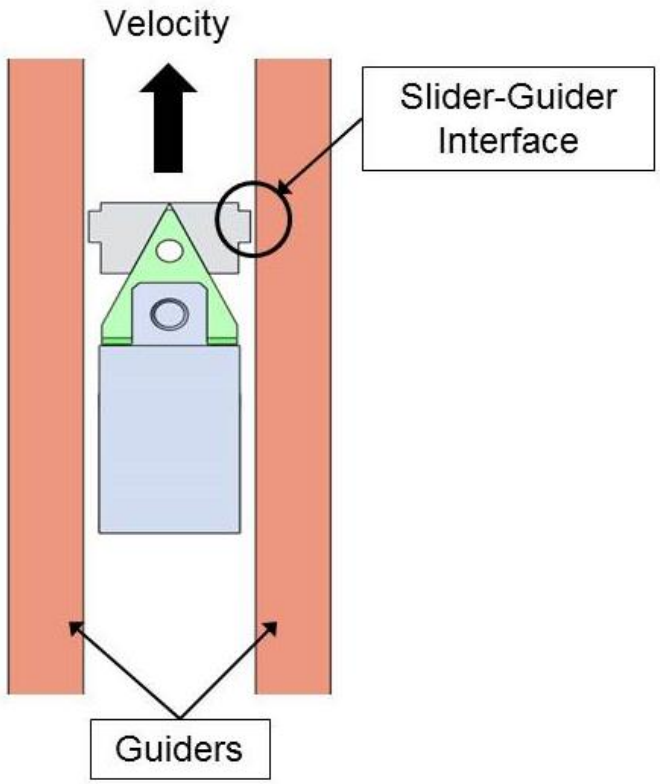

Figure 2.7 - Overhead view of a tribo-slider and guiders.

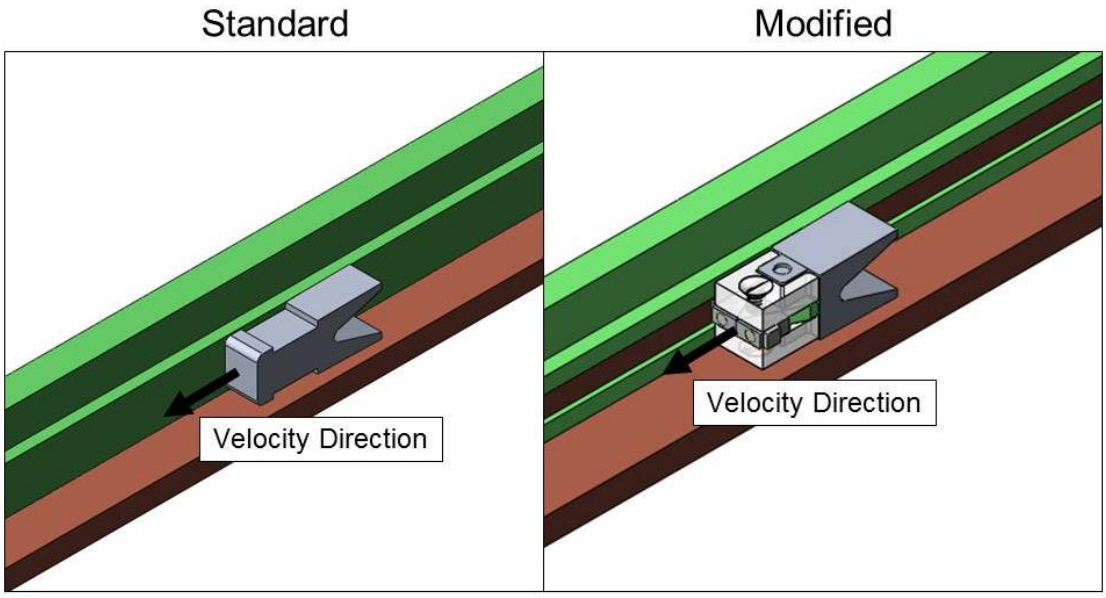

Figure 2.8 - A half open view of the standard bore and armature (left) and modified bore and tribo-slider (right).

wedges from the direct path of the electrical current, used to generate the tribo-slider propulsive force. However, the magnetic field that develops around both the electromagnetic launcher rails and armature due to the electrical current passing through the system, as shown in Figure 2.4, can induce eddy currents in the guiders. These eddy currents result in heat dissipation via Joule heating. It has been shown that the high magnetic field region is concentrated in the interior of the armature legs and throat region [46]. The contact interface between with the slider and guider occurs out in front of the armature where the magnetic field is less intense. For this reason the component of Joule heating at the contact interface can be considered negligible relative to the heat dissipation process due to the physical interaction of the slider and guider.

2.3 Test Conditions and Analysis

For testing, the mass of the tribo-slider was held constant along with the electrical current profile for each EML launch. This provides a near constant acceleration for approximately the first 0.50 to 0.60 meters of travel. The contact pressure generated at the slider-guider interface is controlled via the tribo-slider acceleration, ramp angle and the mass of the wedge. An inertia load, due to the tribo-slider acceleration and wedge mass, generates a body force on the wedge. This body force can be decomposed using the wedge geometry / ramp angle to calculate the contact forces at the slider – guider interface. Additional design considerations were taken to ensure that the center of the slider contact area was aligned with the wedge center of mass as to avoid any unwanted moments and to ensure uniform contact. A quasi-static analysis in the form of a free body diagram, as shown in Figure 2.9, is used to analyze the system. It is important to note

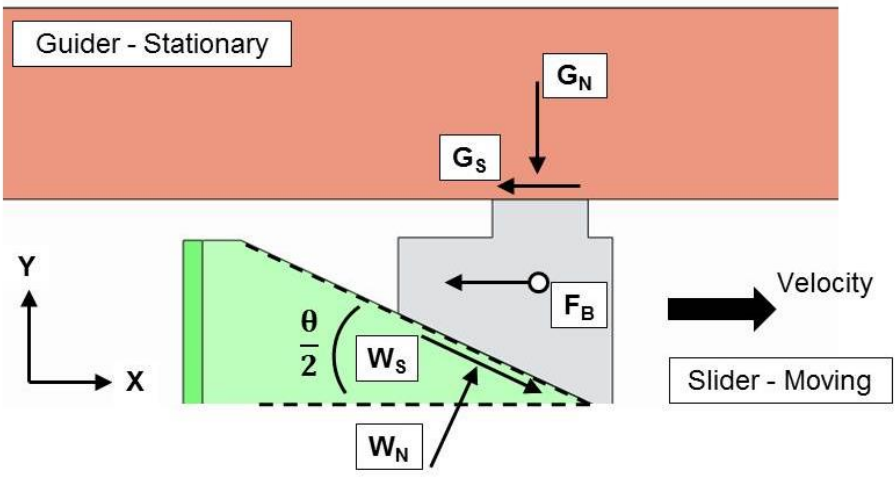

Figure 2.9 – An inertia loaded wedge system used to generate contact pressures at the slider-guider interface.

when analyzing the system that the slider is moving relative to the guider. The guider shear load reacts on the slider in the opposite direction of the tribo-slider travel. The ramp normal and shear loads are the result of the wedge inertia load. These loads are necessary to accelerate the wedge mass with the rest of the tribo-slider. The sum of the forces in the x and y-directions are as follows

$$\sum F_x = W_N \sin\frac{\theta}{2} + W_S \cos\frac{\theta}{2} - G_S - F_B = 0 \tag{2.1}$$

$$\sum F_y = W_N \cos\frac{\theta}{2} - W_S \sin\frac{\theta}{2} - G_N = 0 \tag{2.2}$$

where F_B, is the wedge inertia force, W_N, is the ramp normal force, W_S, is the ramp shear force, G_N, is the guider normal force, G_S, is the guider shear force, and $\frac{\theta}{2}$ is the ramp angle. Equations 2.1 and 2.2 contain five unknowns. In order to solve the system of equations three additional equations are needed. They are as follows

$$G_S = \mu_G G_N \tag{2.3}$$

$$W_S = \mu_R W_N \tag{2.4}$$

$$F_B = m_w a_c \tag{2.5}$$

where μ_G, is the coefficient of kinetic friction at the slider-guider interface, μ_R, is the coefficient of kinetic friction at the wedge-ramp interface, m_w, is the wedge mass, and a_c is the tribo-slider acceleration. Both the mass of the wedge and tribo-slider acceleration are known. Combining Equations 2.1 – 2.5 and rearranging the terms to solve for the guider normal force

$$G_N = \frac{m_w \cdot a_c \left(\cos\frac{\theta}{2} - \mu_R \sin\frac{\theta}{2}\right)}{\left[\mu_G \left(\mu_R \sin\frac{\theta}{2} - \cos\frac{\theta}{2}\right) + \sin\frac{\theta}{2} + \mu_R \cos\frac{\theta}{2}\right]} \tag{2.6}$$

The guider normal force is of interest in this case as it is used to calculate the pressure at the slider-guider interface. It is important to note that the resultant form of the guider normal force, Equation 2.6, is a function of the wedge mass, tribo-slider acceleration, the coefficient of kinetic friction at the wedge-ramp interface, and the coefficient of kinetic friction at the slider-guider interface. Simplifying assumptions can be made to further reduce this equation. These assumptions require insight into the coefficient of kinetic friction at the wedge-ramp and slider-guider interfaces. In order to correctly characterize the sliding behavior between the wedge and ramp it is important to understand there is a relative velocity difference between the two due to slider wear. As the slider wears the wedge moves down the ramp and there is a relative velocity between the wedge and ramp. For a representative set of test conditions the average velocity between the 6061-T6 aluminum wedge and G-10 glass fiber reinforced epoxy ramp is on the order of 1 m/s

and the ramp normal load is on the order of 1000 N. Published data shows a coefficient of kinetic friction for a glass fiber reinforced epoxy on aluminum at a sliding speed of 5.3 m/s and a contact load of 72 N to be 0.04 [47]. As shown in Equation 2.6, the coefficient of kinetic friction (μ_R) at the wedge-ramp interface affects the resultant guider normal load. A coefficient of kinetic friction on the order of 0.01 at the wedge-ramp interface reduces the guider normal load by approximately 2.5%. Similarly for the slider-guider interface at high sliding speeds, just prior to achieving melt lubrication, the coefficient of kinetic friction can be estimated at 0.01. This estimation is based on a wide range of published data using different tribomaterial pairings and load conditions at high sliding speeds [8, 10, 12]. A coefficient of kinetic friction on the order of 0.01 increases the guider normal load by approximately 2.2%. Thus the overall net effect of the wedge-ramp and slider-guider coefficient of kinetic frictions for these conditions is a 0.3% decrease in guider normal load. Based on these conditions it is assumed that the change in the guider normal load due to changes at the wedge-ramp and slider-guider interface negate each other. By making this assumption Equation 2.6 reduces to the following form

$$G_N = \frac{m_w a_c}{\tan\frac{\theta}{2}} \tag{2.7}$$

This form is consistent with the method used by Stefani and Parker in which they assume the wedge is allowed to move freely [4].

Mass measurements of each wedge and the launch package were taken prior to each test using a Mettler Toledo XS64 scale. Instrumentation in the form of position (b-dots) [48-50] and electrical current (Rogowski coils) [51] sensors were used to obtain the tribo-

slider position as a function of time during the EML launch. Acceleration and velocity were calculated using a second order polynomial fit of the position data coupled with the equations of motion. A representative b-dot sensor (position) plot and velocity plot for an EML launch are shown in Figures 2.10 and 2.11. The EML launch data combined with the wedge mass and geometry provides enough information to define and correlate the test conditions, pressure and velocity, to slider wear / deposition on the guider.

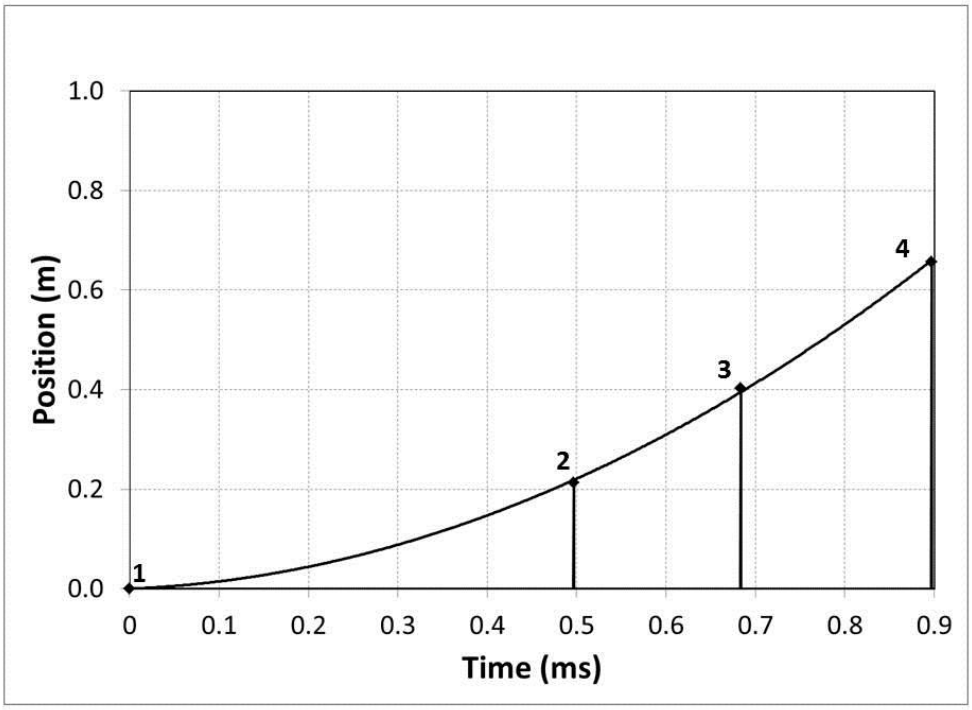

Figure 2.10 Tribo-slider position data from magnetic field sensors (b-dots) as a function of time.

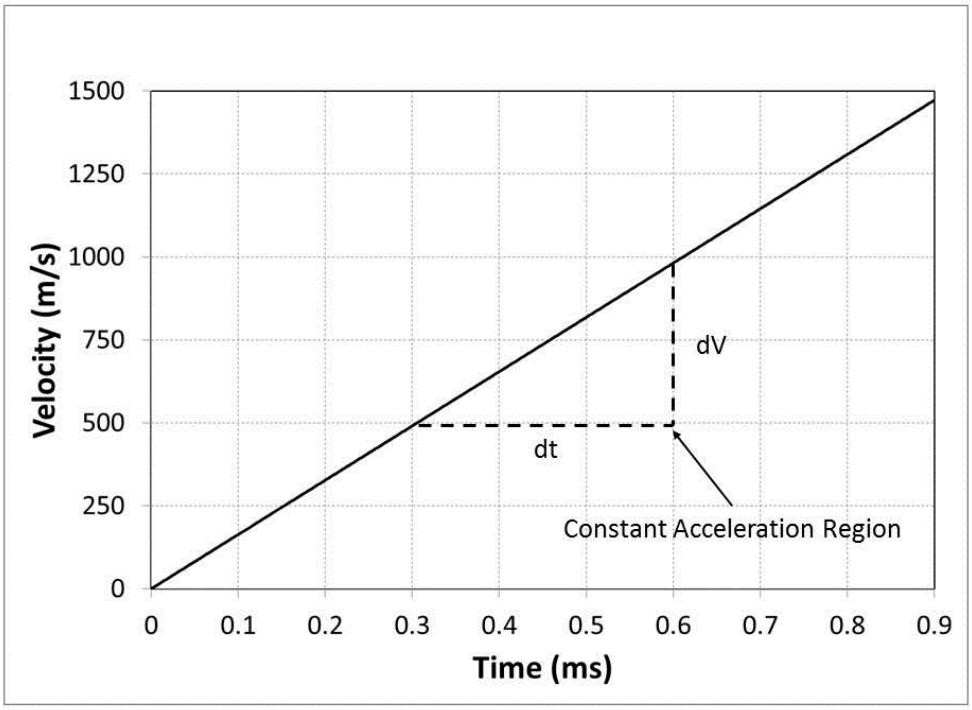

Figure 2.11 – Tribo-slider velocity versus time.

2.4 Slider Wear and Analysis

2.4.1 Slider Wear Overview

The experimental setup provides a combination of material properties and operating conditions that result in worn slider material and deposition on the guiders. The slider deposition is in the form of a visible and distinct "track" of material as shown in Figure 2.12. The track is approximately the width of the wear tab (slider) on the wedge. The appearance of the slider deposition varies as a function of location on the guider and in turn can be related to the operating parameters pressure and velocity through the relationships described in section 2.2. Two different techniques are used to analyze the deposition. The first is optical microscopy, which offers a qualitative assessment of the

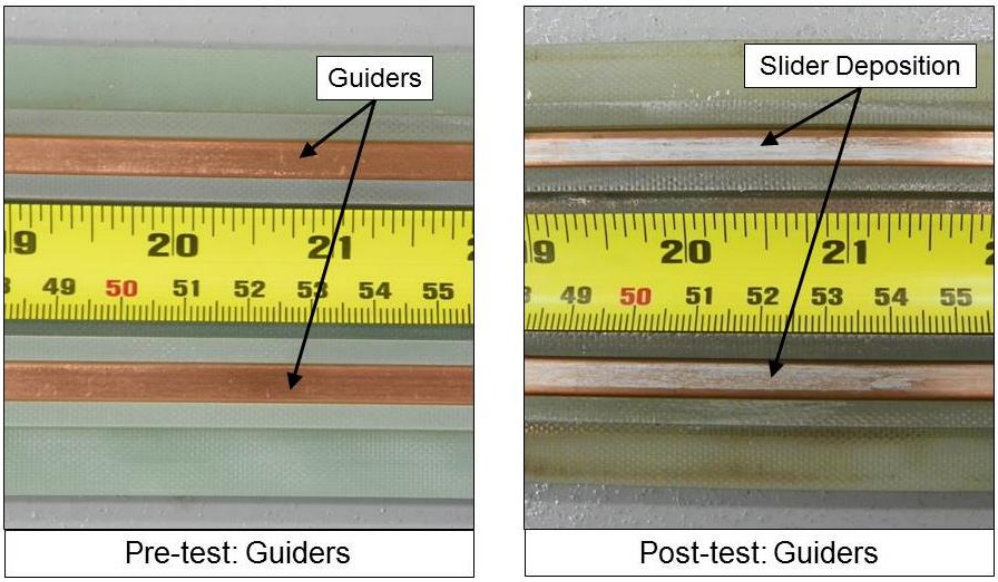

Figure 2.12 - Visual appearance of the guiders pre-test (left) and post-test (right).

deposition and the second is 3D profilometry, which provides a quantitative assessment of the deposition.

Prior to analysis, the 1.56 meter long guiders are removed from the EML bore. The initial slider position is visually identified and several measurements and cuts are made to produce 12 centimeter long guider specimens. Additionally, the wedges are retrieved from the soft catch following each test. An example of a wedge pre-test and post-test is shown in Figure 2.13. The forward end of each wedge sustains impact damage during deceleration in the catch tank. Slider wedge measurements are taken via a scale and an optical microscope. Wedge mass measurements, to quantify wear, have shown to be difficult to use due to the impact damage on the forward end of the wedge. Wedge slider height measurements taken using an optical microscope have shown to be more consistent and are used for comparison to wear deposition measurements taken with the 3D profilometer.

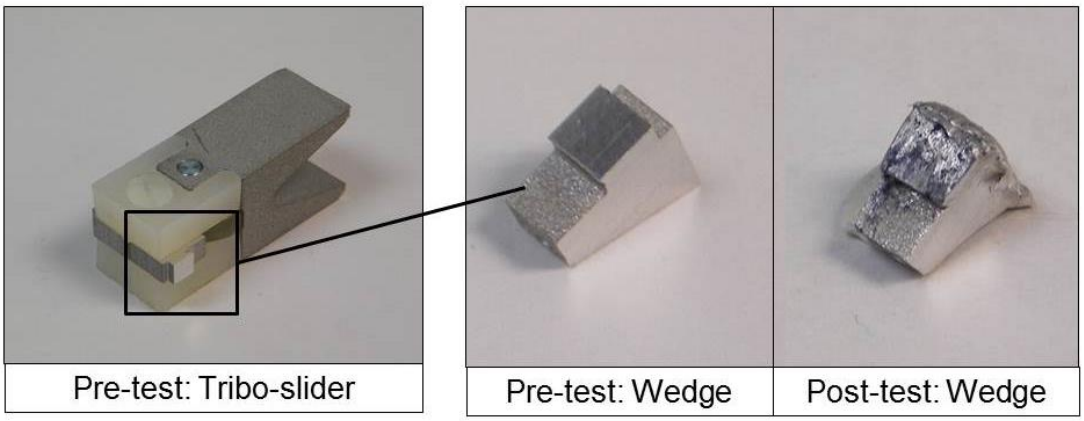

Figure 2.13 - A fully assembled tribo-slider (left) and wedge (center) prior to testing. Retrieval of the wedge from the soft catch post-test shows visible impact damage is sustained during deceleration (right).

2.4.2 Slider Wear Analysis

Following each test the guider specimens are viewed under a Leica DM 4000 optical microscope to identify changes in the appearance of the slider deposition as a function of guider location. Typical identifying attributes include deposition form, consistency, color, and distribution. A micrograph from an aluminum slider on copper guider test at 101 MPa and 1,070 m/s is shown in Figure 2.14. The reddish-brown material is the copper guider and the dark gray, spherical protrusions that are somewhat uniformly dispersed over the surface are the deposited aluminum from the slider. A more in depth look at the evolution of wear as a function of pressure and velocity is discussed in Chapter 3.

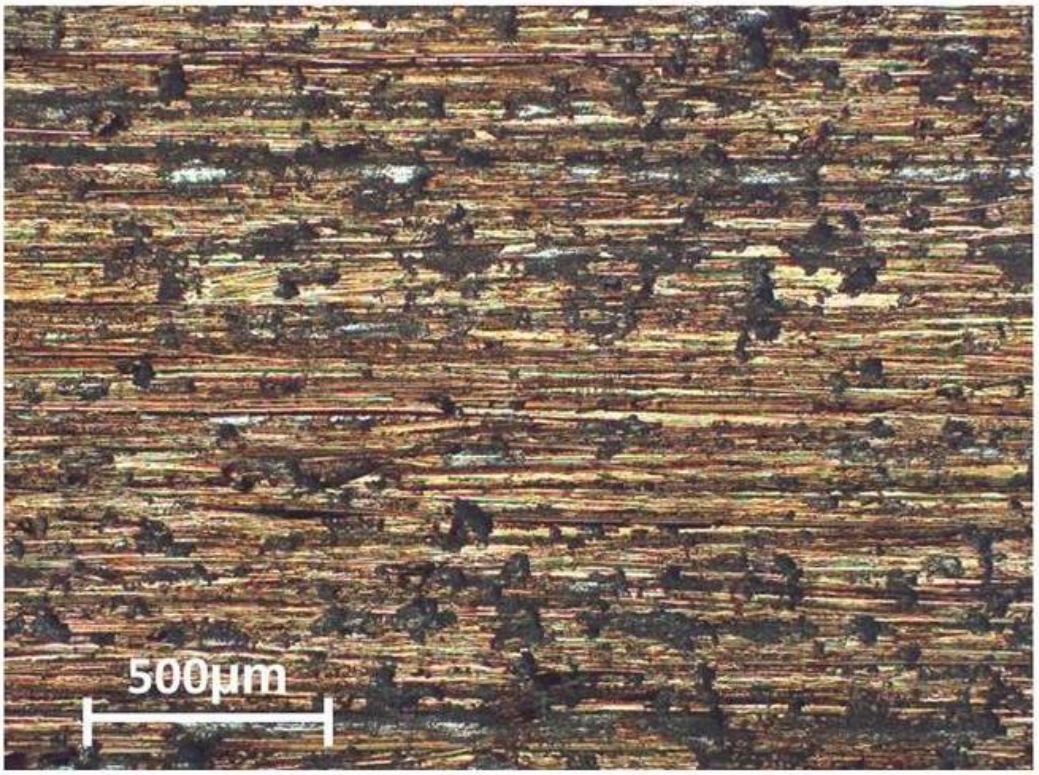

Figure 2.14 - A micrograph of slider deposition from an aluminum slider on copper guider test at 101 MPa and 1,070 m/s.

After each guider specimen undergoes a qualitative assessment the specimen is then prepared for 3D profilometry. The aluminum deposition on each guider is quantified using a Zygo NewView 6k scanning white light interferometer (non-contact optical profilometry), as pictured in Figure 2.15. Discrete deposition measurements at incremental locations along the length of each guider provide wear data as a function of position, velocity, pressure and tribomaterial pairing. Prior to each scan the guider location of interest is marked into three different segments, a left reference area, a test area and a right reference area, as shown in Figure 2.16. The test area was masked using a steel fixture and the reference areas were cleaned by "flaking" off the deposition

Figure 2.15 - The Zygo NewView 6k scanning white light interferometer (non-contact optical profilometer) used to measure the aluminum deposition.

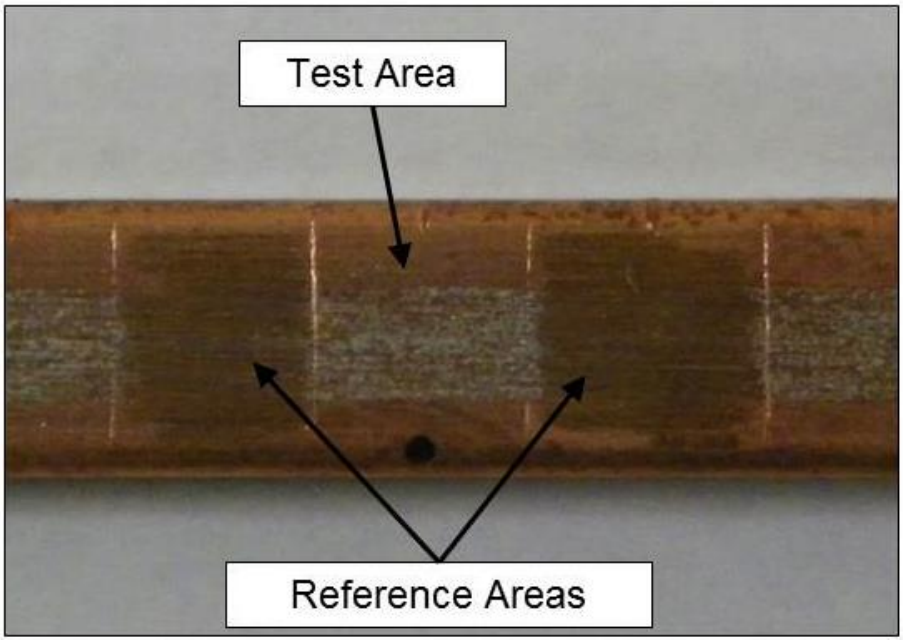

Figure 2.16 - Example of a cleaned guider specimen. Reference areas and a test area are required for volume measurements using the 3D profilometer.

followed by a sodium hydroxide swab to remove any residual aluminum, as sodium hydroxide reacts with aluminum in a corrosive manner. The removal of the deposition to the left and right of the desired test area is necessary in order to properly characterize the guider surface roughness and any deformation that may have taken place due to contact with the slider. The MetroPro 8.1.5 software package that is part of the scanning white light interferometer system utilizes these reference areas to define a plane from which to take a volume measurement on in the test area. Due to the size of the scan, 10 millimeters by 5 millimeters, it is necessary to use an application within the MetroPro 8.1.5 software called "stitch.app." The stitch application takes several smaller scans and combines them to form a larger representative scan of the test area. Due to the large scan area, an extended scan length option is necessary to capture the full range of depth. The combination of the large scan area coupled with the extended scan created a pixel-to-pixel resolution of 2.18 micrometers with a vertical resolution of 0.02 micrometers. Typical deposition thickness, when averaged over the measurement area, is on the order of 10 micrometers, making the error due to vertical resolution approximately 0.2% of the measurement. An example of a scanned test area is shown in Figure 2.17. The red spherical shaped protrusions are the slider deposition and the blue underlying material is the guider surface defined through the use of the reference areas.

Each test may have as many as eighteen different slider deposition locations that were quantified. A total of five volumetric deposition measurements were taken at each location in order to properly characterize the variation in the slider deposition. A statistical analysis was conducted to determine the mean and standard deviation for each set of five measurements. Using the methodology, as outlined in section 2.3, each mean

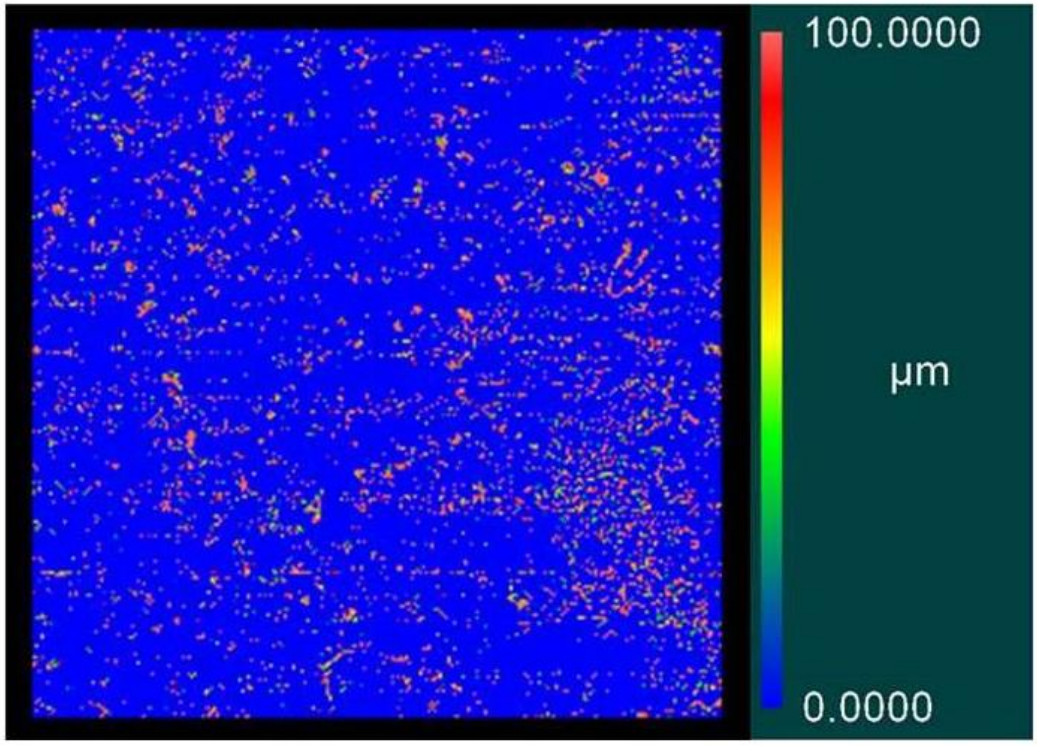

Figure 2.17 - An example of a scan in the test area of the melt lubrication region using a scanning white light interferometer.

volumetric slider deposition measurement, for a given location, can be related to velocity and contact pressure so that further analysis can be performed. Before such analysis is conducted there is a final calculation that is performed on the volumetric wear data. In tribology when quantifying wear rates instead of per unit time they are quoted per distance slid. This is often due to the manner in which the tests are conducted. Volumetric wear of metal-metal sliding contacts, depending on the operating conditions, can be relatively small and require large distances under steady state conditions to quantify the worn material via mass loss or height change. For a specific material pairing

the volumetric wear, as defined by Archard and Holm [52, 53] can be predicted using the following definition

$$V = \frac{k \cdot W \cdot x}{H_o} \tag{2.8}$$

where k is a nondimensional wear coefficient dependent on the tribomaterial pairing, W is the normal load, x is the distance slid, and H_o is the room temperature hardness. For dry sliding contacts of aluminum and aluminum alloys on steel it has been shown that wear coefficients are on the order of 10^{-5} to 10^{-8} [13, 54, 55]. For the sliding conditions of the tests outlined in this dissertation, the operating parameters are representative of extreme metal-metal sliding contact and result in relatively large amounts of volumetric wear over short sliding distances with wear coefficients for aluminum on copper, steel, and titanium on the order of 10^{-3}. The high wear coefficients, combined with the 3D profilometry measurement technique, requires that only a short distance slid is necessary to capture the local volumetric wear rate. A distance of 3.2 millimeters, equal to one slider length, is the distance over which the volumetric wear measurements are taken using the MetroPro 8.1.5 software and because the 3.2 millimeter distance slid is relatively small, the change in velocity of the slider over this distance is also relatively small, approximately 0.2 to 1.5%. The resultant form is a volumetric wear rate in units of cubic millimeters per millimeter.

In addition to putting the volumetric wear data in a rate form, it is also useful to normalize it relative to the nominal area of contact. In doing so the normalized

volumetric wear rate data takes on a dimensionless form which provides distinct advantages when comparing and scaling data across different geometries and test setups. The normalized volumetric wear rate, while dimensionless, is often displayed in units of millimeter per millimeter. This is to remind the reader that wear rates, in Tribology, are with respect to distance slid, not time. The normalized wear rate is defined as

$$\widetilde{W} = \frac{V}{A_n \cdot x} \tag{2.8}$$

where V is the volume of worn material, A_n is the nominal contact area of the slider and x is the distance slid .

2.4.3 Data Interpretation

At the end of each test, a set of volumetric wear data is collected from the guider, put into rate form, and normalized. The data can be plotted as function of guider location (position), velocity or some combination of operating parameters such as the product of pressure and velocity. The focus of this research is wear at high sliding speeds and high contact pressures. Based on literature reviewed in Chapter 1, it is expected that slider-guider interface will be molten and a melt layer or film will support the slider load. The primary wear mechanism is melt lubrication and the source of heat in this case is viscous dissipation. For this reason the appearance of the deposition is important when surveying the guider specimens so as to focus the 3D profilometry measurements in the region of

interest. The melt lubrication region, depending on the test conditions for the experiments conducted, initiates between 25 and 35 centimeters of travel and ends at approximately 45 to 50 centimeters of travel providing 10 to 25 centimeters of guider to analyze. The precursor to the melt lubrication region is marked by a high wear rate that steadily decreases until a critical velocity is achieved at which point a molten metal film capable of supporting the contact load has formed. The melt lubrication region continues until the acceleration begins to decrease at approximately 45 to 50 centimeters, at which point the aluminum deposition begins to lessen due to lighter contact loads.

Each set of 3D profilometry measurements is compared to the optical microscopy qualitative assessment to ensure that the aluminum deposition appearance and the location at which the melt lubrication region initiates and ends correlates well with each other. Normalized wear rates in the melt lubrication region showed a linear dependence on velocity, as will be discussed in Chapter 3. There were instances when a data point deviated from this trend. In these instances the guider specifications were inspected. There are two reasons for the guider specification to be out of tolerance. During installation the guiders are seated into the sidewall insulators and flatness measurements are taken to ensure that guider "waviness" is minimized. This waviness in the guiders has two effects. The first being loss of contact if the slider moves from a high to low spot on the guider. This often results in an unusually low slider deposition. The second is an increase in the guider normal force due to slider movement from a low to high spot on the guider. This results in an unusually high slider deposition. If the guider was found to be out of spec in the location in question then the data point was removed from the set.

2.4.4 Data Error Assessment

The slider deposition was quantified using a scanning white light interferometer at discrete locations along the length of the guider following the completion of a test. Each test may have as many as eighteen different slider deposition locations that were quantified and related to a set of operating conditions (pressure and velocity). A total of five volumetric deposition measurements were taken at each location to characterize the variation in the slider deposition. A statistical analysis was conducted to determine the mean and standard deviation for each set of five measurements. From this analysis the normalized wear rate and the associated uncertainty, with a 95% confidence interval, were calculated using Equation 2.8. An uncertainty of 5-10% of the calculated normalized wear rate value is typical for the wear regions quantified (severe plastic deformation and melt lubrication) in this dissertation.

There are three potential sources of error that contributed to the 5-10% uncertainty. The first source of error is due to the resolution of the scanning white light interferometer, which varies depending on the depth of the scan. In order to properly capture the full vertical range of the slider deposition an extended scan was required, resulting in a vertical resolution of 0.02 micrometers. Typical deposition thickness in the wear regions investigated, when averaged over the measurement area, is on the order of 10 micrometers, making the error due to the vertical resolution approximately 0.2%.

The second source of error is due to the length over which the volumetric wear measurements are taken. A set of five measurements was incrementally taken over a distance of 5 millimeters to adequately capture the variability in slider deposition at each location. As it was discussed previously, in Section 2.3, the slider velocity increases as

the slider travels down the guider. This means for each set of five measurements the slider deposition measured is for a range of velocities. For analysis purposes the average velocity is reported. For a measurement distance of 5 millimeters the velocity increases by approximately 0.2 to 1.5%. The changing velocity results in a different set of contact conditions that may influence the rate of slider deposition.

The third and final source of error is related to the surface topography of the guider. Material processing techniques used in forming each guider and deformation due to the interaction of the slider – guider contact results in a guider arithmetic mean surface roughness of $\leq$ 1 micrometer. Typical slider deposition, when averaged over the measurement area in the wear region of interest, is on the order of 10 micrometers. The MetroPro 8.1.5 software package, that is part of the scanning white light interferometer system, takes a best fit plane of the reference areas on each side of the test area so as to average out the effects of the guider topography and calculates the volume of material in the test area above the best fit plane. Both the slider deposition and the guider topography are included in this volume calculation. In doing so, error is introduced due to the statistical distribution of the guider topographical features (peaks and valleys). For an arithmetic mean surface roughness of 1 micrometer and an average deposition thickness of 10 micrometers, the resultant error in the volumetric measurement can be ±10%.

Of the three sources of error introduced, the third source of error is the largest and compares well to the measured 5-10% uncertainty. This suggests that as the slider deposition increases the contribution of the error introduced through the MetroPro software calculation decreases. Conversely, for smaller amounts of slider deposition, less than 10 micrometers, this error becomes increasingly more significant. The average slider

deposition in the wear regions of interest quantified in this dissertation are on the order of 10 micrometers.

CHAPTER 3: Experimental Results - Wear Regimes

3.1 Overview

The main objective to studying high velocity wear is to gain a fundamental understanding of the effects that the operating conditions, such as pressure and velocity, and tribomaterial pairings have on normalized wear rates. Limitations in the available diagnostic capabilities, due to the time scale of the test (microseconds), makes it difficult to assess normal loads, shear loads, and temperatures at the slider-guider interface using traditional measurement techniques. For this reason only the pressure and velocity operating parameters are known / calculated, as discussed in Chapter 2. A combination of qualitative (optical microscopy) and quantitative (3D non-contact profilometry) assessment techniques are used in conjunction with theory and existing literature to identify the wear type and the associated mechanism(s) responsible for the slider wear.

The experimental technique used to study slider wear at high sliding speeds and high contact pressures covers a wide range of velocities, 0 – 1,200 m/s, and pressures, 100 – 225 MPa, for a 6061-T6 aluminum slider on a C110-H2 guider. The normalized contact pressure, velocity and wear rates for the experiments conducted, as defined by Equations 1.1 – 1.3, are summarized in Table 3.1. An aluminum alloy wear mechanism map [15], as shown in Figure 3.1, is used to evaluate the conditions of the experiments conducted in this dissertation versus those compiled from literature. The wear mechanism map and contours of normalized wear rates are empirically calibrated to wear data for aluminum alloys using the concepts and models developed by Lim and Ashby [10]. Five regions are defined: oxidation dominated wear, plasticity dominated wear, severe plastic

Table 3.1 - Normalized pressure, velocity and wear rates for 6061-T6 aluminum experiments.

Slider Material	σ (MPa)	σ_{UTS} (MPa)	v (m/s)	r_o (m)	χ (m^2/s)	$\tilde{F}$	$\tilde{v}$	$\tilde{W}$
6061-T6	100-225	310	0 – 1200	1.8×10^{-3}	6.6×10^{-5}	0.3-0.7	$0 – 3.3 \times 10^{4}$	$10^{-3} – 10^{-2}$

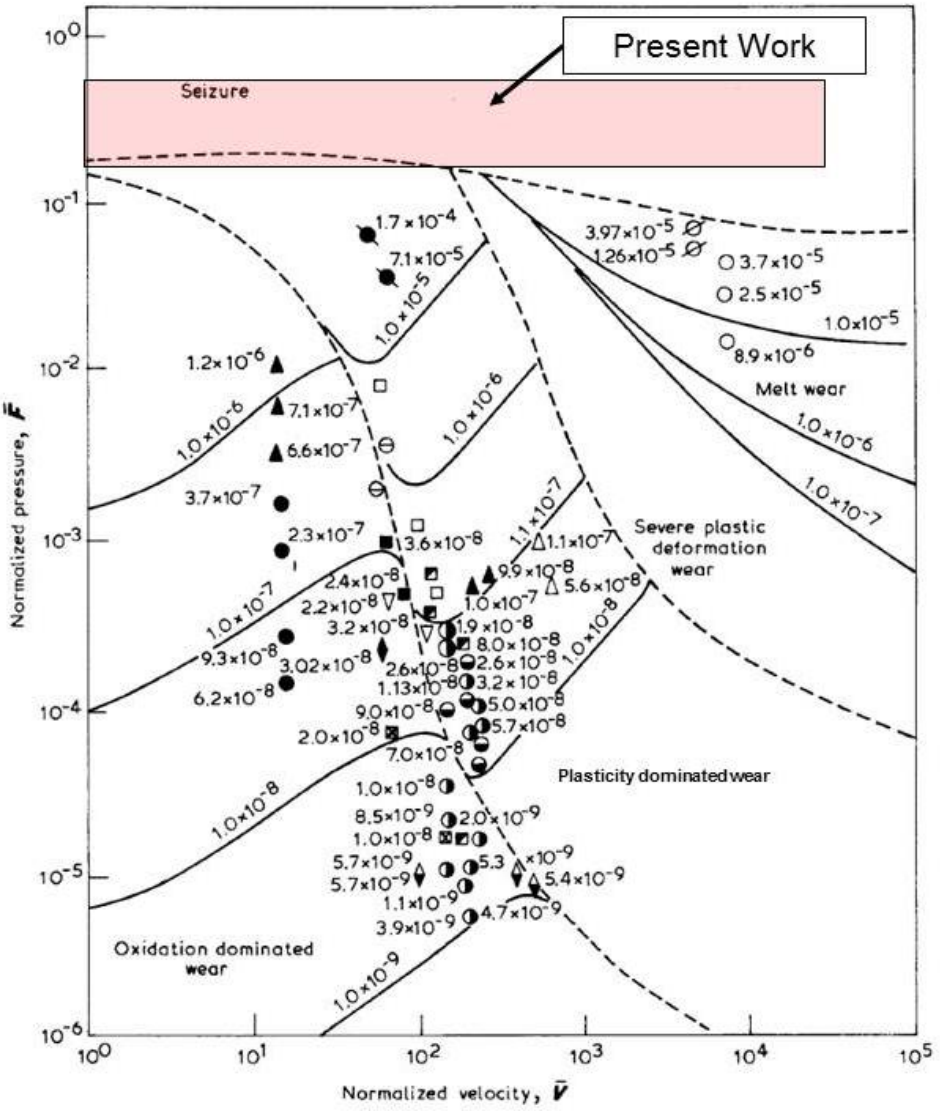

Figure 3.1 - An aluminum alloy wear mechanism map [15].

deformation, melt wear and seizure.

Each region is defined by the dominant wear mechanism. The wear debris in the oxidation dominated region is the result of high flash temperatures, due to frictional heat dissipation, that result in oxidation of the aluminum contact interface. When the oxide film reaches a critical thickness it spalls off leaving behind a wear fragment. The plasticity dominated region is characteristic of Archard's wear [52, 53] in which the softer material is plastically deformed and sheared off as it adheres to the harder material. The underlying mechanism for this failure has been attributed to subsurface crack nucleation and propagation and the wear in this region can also be referred to as delamination [56]. The severe plastic deformation region is the result of thermal softening at the asperity level due to frictional heat dissipation at the contact interface resulting in localized plastic flow. When the heat dissipation is large enough the localized plastic flow transitions to localized melting and is representative of melt wear. Finally, seizure occurs when the contact load is large enough such that the real area of contact is equivalent to the nominal area of contact and can result in plastic indentation, large scale material flow or large scale metallic transfer.

The slider operating conditions of the work presented in this dissertation are highlighted in red on the map and predominately operate in the seizure wear region, adjacent to the plasticity, severe plastic deformation and melt wear regions. The seizure boundary line is hypothetical as there is no experimental wear data for model calibration. If the seizure boundary line was shifted to a normalized pressure of 10^0 and the adjacent wear regions were extrapolated, then three different types of wear: plasticity dominated wear, severe plastic deformation and melt wear would be expected. Additionally as

discussed in Chapter 1, for high sliding speeds and large contact loads a fourth wear region, melt lubrication, may exist. The normalized wear rate data collected from the experiments conducted in this dissertation provides new wear data that can be used to validate existing wear mechanisms and to identify / define new mechanisms.

A qualitative assessment of the slider wear for 6061-T6 aluminum on a C110-H2 copper guider is made for sliding speeds in the range of 200 – 1,200 m/s at a contact pressure of 101 MPa. It is anticipated that at low sliding speeds, less than 1,000 m/s, the wear mechanisms are plasticity dominated wear and severe plastic deformation and for sliding speeds in excess of 1,000 m/s the expected wear mechanism is melt lubrication. The primary region of interest for this dissertation is at sliding speeds in the range of 1,000 – 1,200 m/s. A quantitative assessment was made in this range for several different contact pressures between 100 – 225 MPa. Both the qualitative and quantitative results are discussed in the following sections.

3.2 Qualitative Analysis of Slider Deposition

A qualitative assessment was made for each of the tests conducted as to correlate the changes in the wear regions identified using optical microscopy to those measured using 3D non-contact profilometry. In general three distinct wear regions presented themselves: plasticity dominated wear, severe plastic deformation and melt lubrication. The plasticity dominated wear region occurred at lower velocities, less than 800 m/s ($\tilde{v}$ = $2.2 \cdot 10^4$), while severe plastic deformation occurred at mid-range velocities, 800 to 1,000 m/s ($\tilde{v}$ = $2.2 - 2.7 \cdot 10^4$), and melt lubrication at velocities greater than 1,000 m/s ($\tilde{v}$ = $2.7 \cdot 10^4$). A total of eight tests with varying contact pressure and slider-guider material pairings were conducted, as summarized in Table 3.2. For all eight tests the slider material was held

Table 3.2 - Slider-guider material pairings and conditions for all eight tests.

Test No.	Slider Material	Guider Material	Contact Pressure (MPa)	Peak Velocity (m/s)
1	6061-T6	C110-H2	101	1210
2	6061-T6	C110-H2	122	1180
3	6061-T6	C110-H2	124	1210
4	6061-T6	C110-H2	130	1190
5	6061-T6	C110-H2	225	1180
6	6061-T6	1045 Steel	135	1140
7	6061-T6	1018 Steel	134	1150
8	6061-T6	Titanium G2 CP	144	1170

constant as 6061-T6, while four different guider materials were explored, C110-H2, 1018 steel, 1045 steel, and titanium grade 2 commercial purity. Three sets of micrographs, one set for each wear region, are presented. Within each set there are four micrographs, one for each of the different slider-guider material pairings. In general the perceived difference between the slider deposition and the guider is easier to differentiate for the 6061-T6 slider and C110-H2 guider material pairing due to the contrasting colors of the materials. These differences are more difficult to observe for the 6061-T6 slider deposition on the 1018 steel, 1045 steel, and titanium guiders as the materials are similar in color.

A micrograph of the plasticity dominated wear region for a 6061-T6 aluminum slider on a C110-H2 guider at a contact pressure of 101 MPa and a sliding speed of 700 m/s is shown in Figure 3.2. The reddish brown colored material is the C110-H2 copper guider, while the darker gray material is the deposited 6061-T6 aluminum. Visually the slider

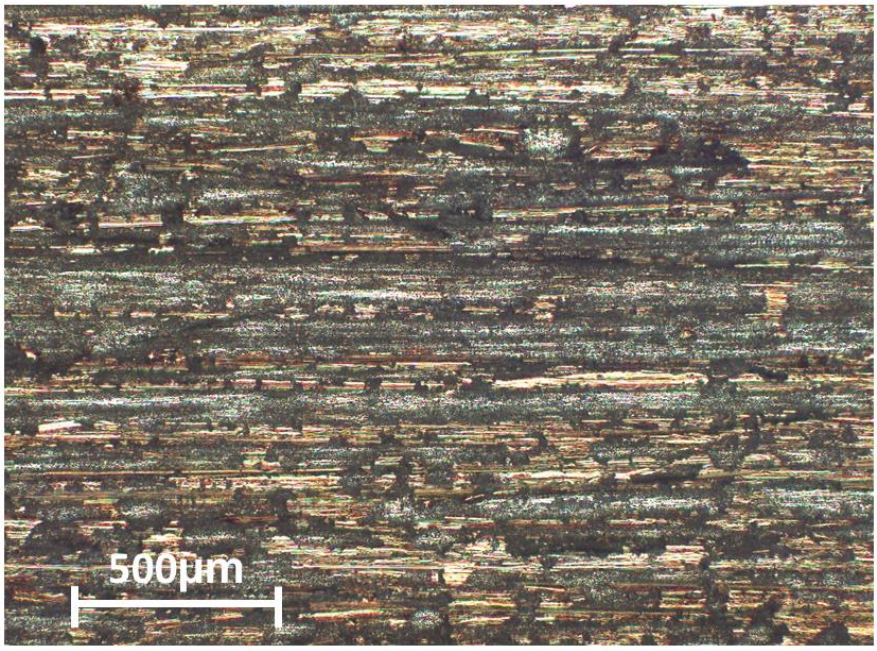

Figure 3.2 - A micrograph of the plasticity dominated wear region for a 6061-T6 aluminum slider on C110-H2 guider at a sliding speed of 700 m/s and a contact pressure of 101 MPa.

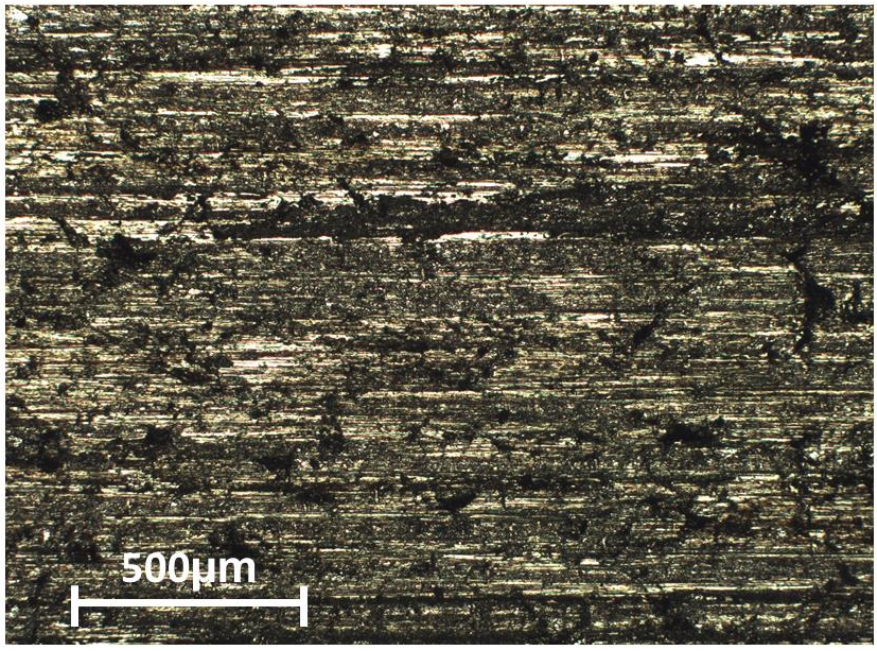

Figure 3.3 - A micrograph of the plasticity dominated wear region for a 6061-T6 aluminum slider on 1018 steel guider at a sliding speed of 490 m/s and a contact pressure of 134 MPa

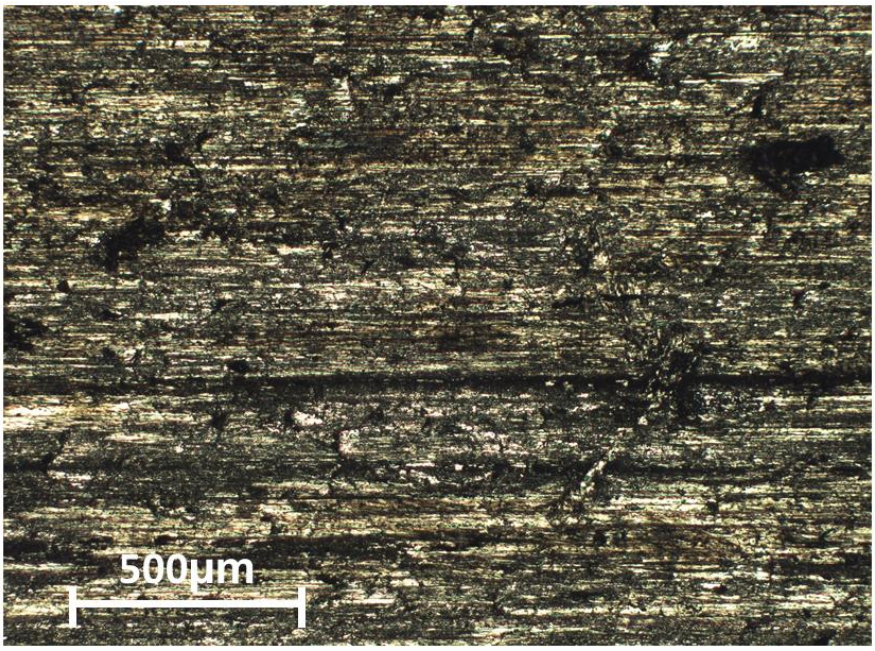

Figure 3.4 - A micrograph of the plasticity dominated wear region for a 6061-T6 aluminum slider on 1045 steel guider at a sliding speed of 560 m/s and a contact pressure of 135 MPa.

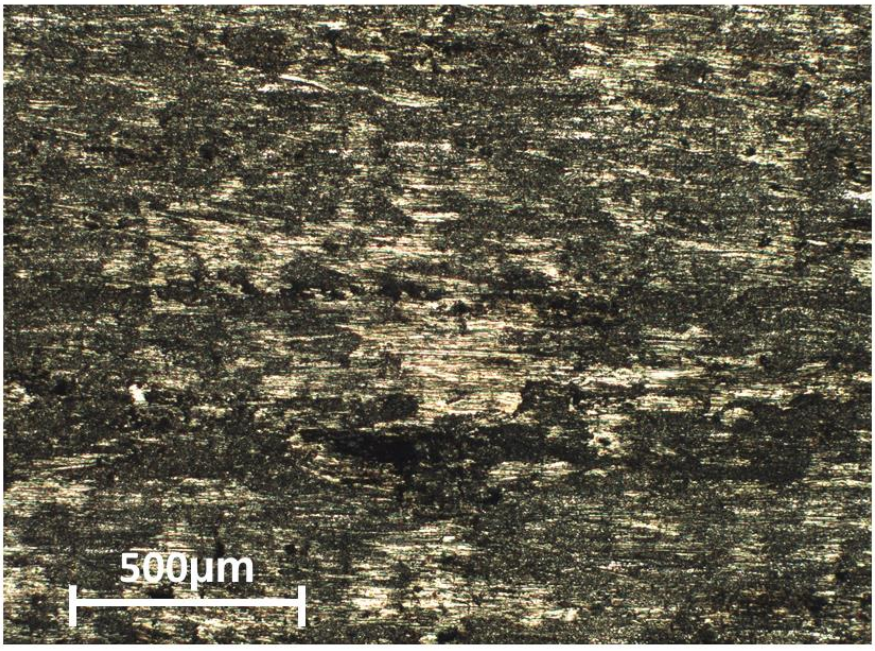

Figure 3.5 - A micrograph of the plasticity dominated wear region for a 6061-T6 aluminum slider on titanium commercial purity grade 2 guider at a sliding speed of 580 m/s and a contact pressure of 144 MPa.

deposition in the plasticity dominated wear region has a shiny appearance and is representative of uniformly smeared aluminum, leaving behind a track of material approximately equal to the width of the slider. Additional micrographs for a 6061-T6 aluminum slider on a 1018 steel, 1045 steel, and titanium commercial purity grade 2 guider in the plasticity dominated wear region are shown in Figures 3.3 – 3.5.

A micrograph of the severe plastic deformation wear region for a 6061-T6 aluminum slider on a C110-H2 guider at a contact pressure of 101 MPa and a sliding speed of 930 m/s is shown in Figure 3.6. The reddish brown color material is the C110-H2 copper guider, while the darker gray material is the 6061-T6 aluminum. The severe plastic deformation wear region deposition differs in appearance from the plasticity dominated wear region. In general the deposition is representative of larger shapeless pieces of randomly distributed material with non-uniform coverage. Visually the deposition had a more matte finish rather than a shiny appearance. The change from plasticity dominated wear to severe plastic deformation can be thought of as a change from localized heating at the asperity level to larger scale heating, to a point where the temperature gradients between asperities begin to interact causing a bulk temperature rise at the surface. This rise in temperature results in thermal softening and in turn large scale shearing / plastic deformation of the slider surface. Additional micrographs for a 6061-T6 aluminum slider on a 1018 steel, 1045 steel, and titanium commercial purity grade 2 guider in the severe plastic deformation region are shown in Figures 3.7 – 3.9.

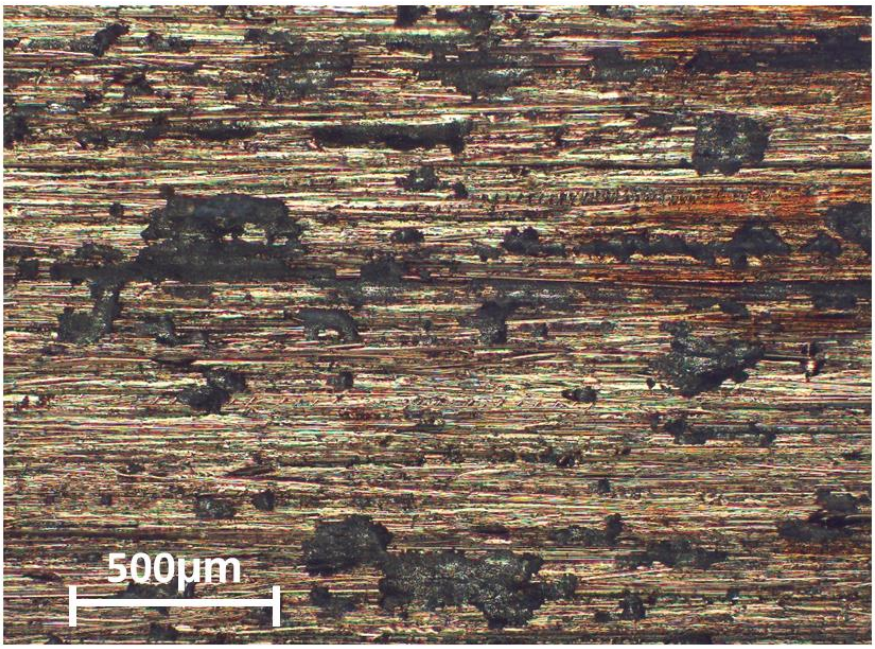

Figure 3.6 - A micrograph of the severe plastic deformation wear region for a 6061-T6 aluminum slider on C110-H2 guider at a sliding speed of 930 m/s and a contact pressure of 101 MPa.

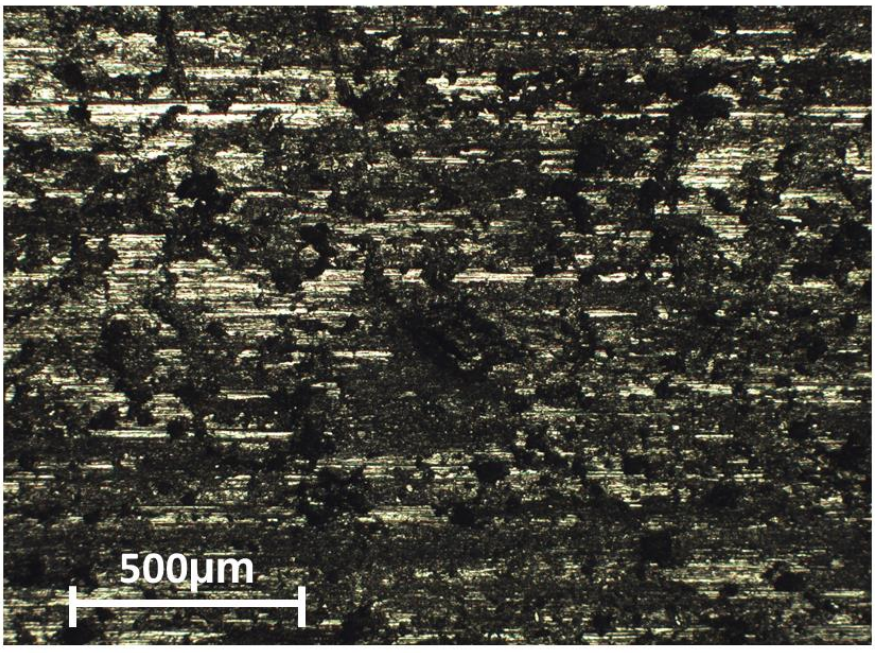

Figure 3.7 - A micrograph of the severe plastic deformation wear region for a 6061-T6 aluminum slider on 1018 steel guider at a sliding speed of 910 m/s and a contact pressure of 134 MPa.

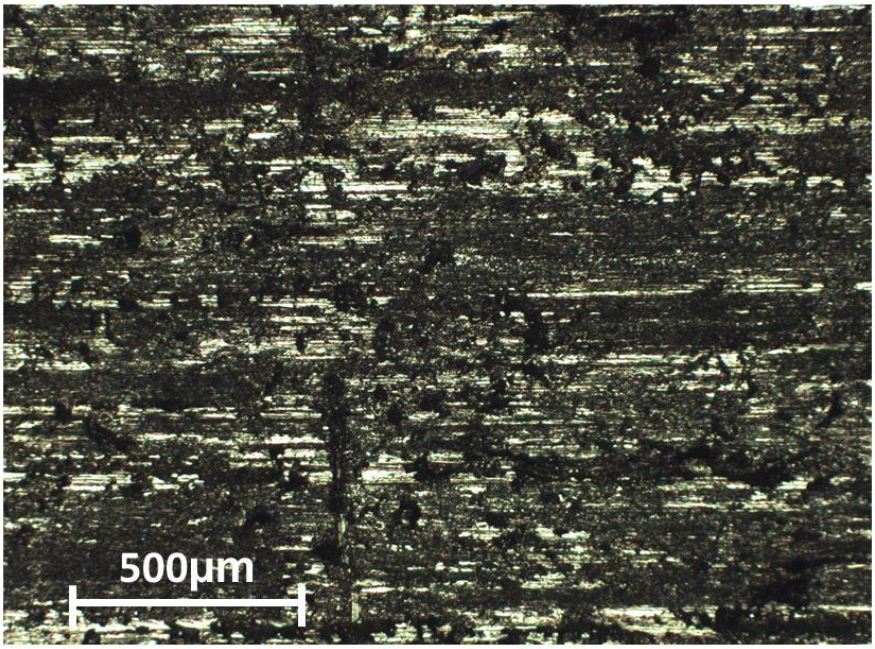

Figure 3.8 - A micrograph of the severe plastic deformation wear region for a 6061-T6 aluminum slider on 1045 steel guider at a sliding speed of 930 m/s and a contact pressure of 135 MPa.

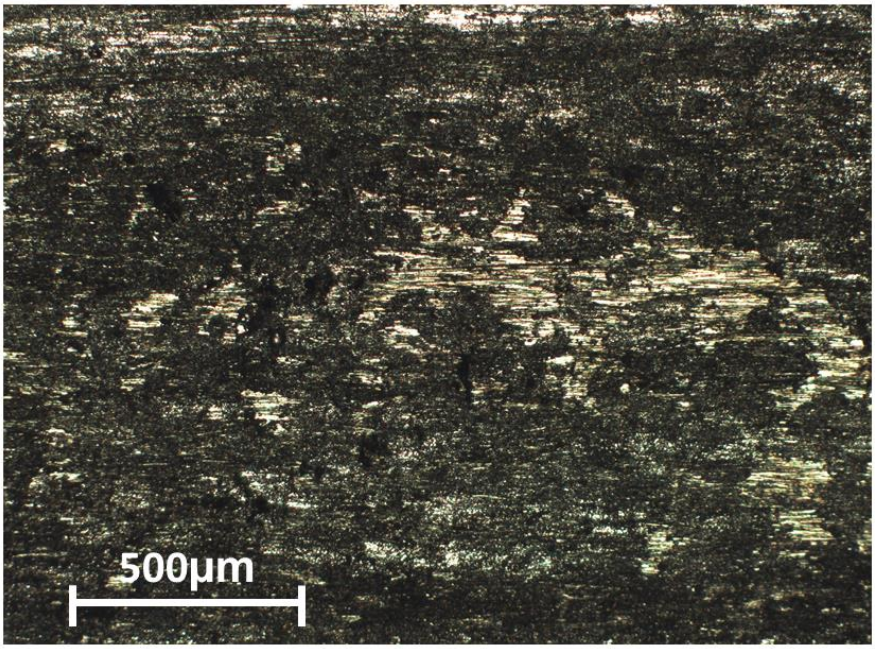

Figure 3.9 - A micrograph of the severe plastic deformation wear region for a 6061-T6 aluminum slider on titanium commercial purity grade 2 guider at a sliding speed of 800 m/s and a contact pressure of 144 MPa.

Lastly, a micrograph of the melt lubrication wear region for a 6061-T6 aluminum slider on a C110-H2 guider at a contact pressure of 101 MPa and a sliding speed of 1,070 m/s is shown in Figure 3.10. The reddish brown color is the C110-H2 copper guider and the darker gray material is the 6061-T6 aluminum deposition. The deposition in the melt lubrication wear region differs from both the plasticity dominated and severe plastic deformation regions. In general the melt lubrication wear deposition is hemispherical in shape and more uniformly dispersed. Visually the deposition has a matte finish. The deposition coverage appeared to increase with increasing velocity and this was confirmed through the use of 3D profilometry as discussed in section 3.3. Additional micrographs of for a 6061-T6 aluminum slider on a 1018 steel, 1045 steel, and titanium commercial purity grade 2 guider in the melt lubrication region are shown in Figures 3.11 – 3.13.

The transition from severe plastic deformation to melt lubrication is the result of an increase in heat dissipation due to the shearing /plastic deformation of the slider surface. Under these conditions the resultant heat generated is sufficient to melt the slider interface and to form a melt film capable of supporting large contact loads. Upon cooling the aluminum film solidifies and takes on a hemispherical shape, exposing the underlying guider material. This is a product of how the aluminum wets and adheres to the surface. The solidified aluminum protrusions can have a height on the order of 100 micrometers. Volumetric measurements of the slider deposition in the melt lubrication region combined with the slider nominal contact area results in an average melt film thickness on the order of 10 micrometers, prior to solidification. This differs from the plasticity dominated wear region. In the plasticity dominated region the slider material is smeared across the guider surface providing more uniform coverage. The slider deposition in this

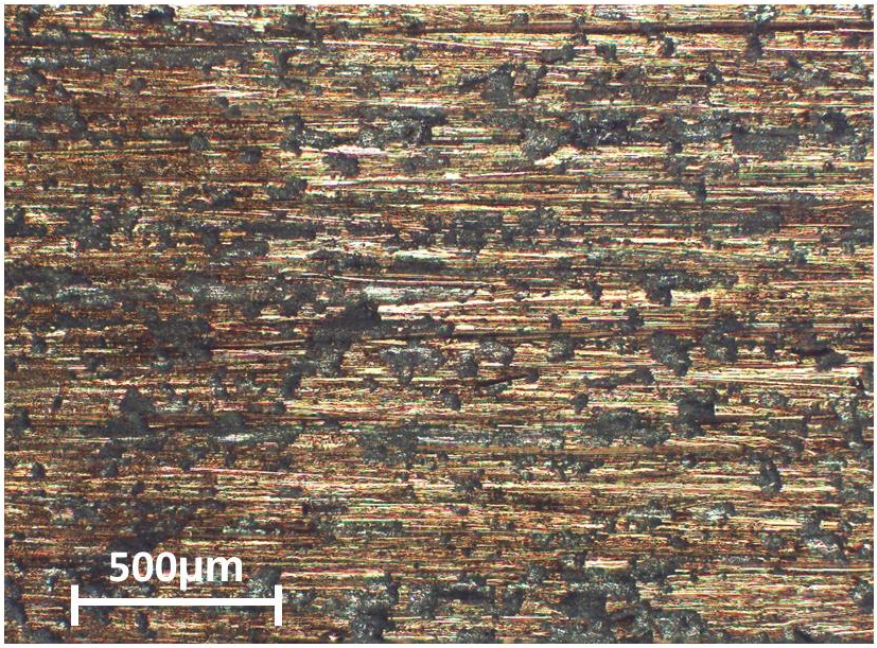

Figure 3.10 - A micrograph of the melt lubrication wear region for a 6061-T6 aluminum slider on C110-H2 guider at a sliding speed of 1,140 m/s and a contact pressure of 101 MPa.

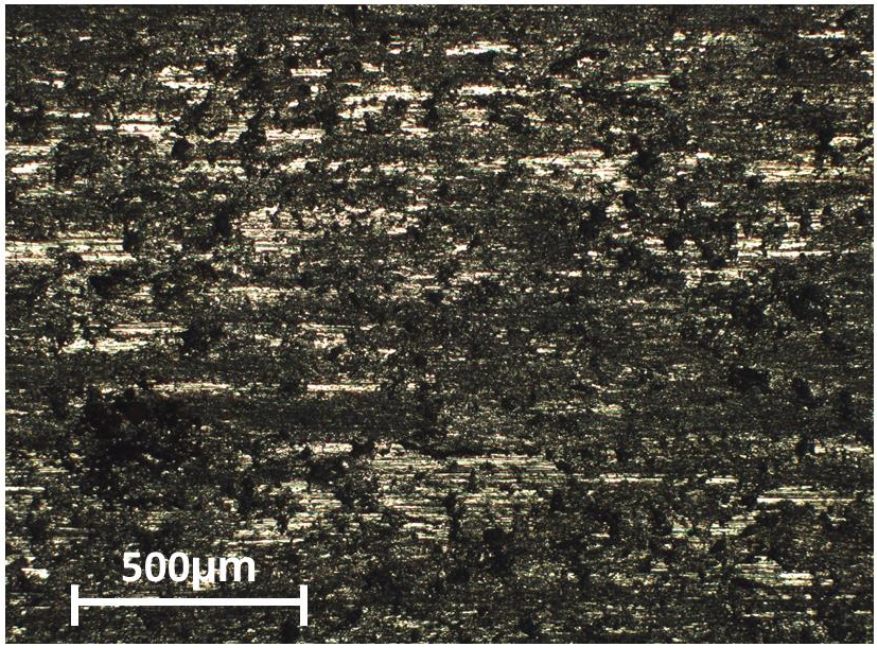

Figure 3.11 - A micrograph of the melt lubrication wear region for a 6061-T6 aluminum slider on 1018 steel guider at a sliding speed of 1,100 m/s and a contact pressure of 134 MPa.

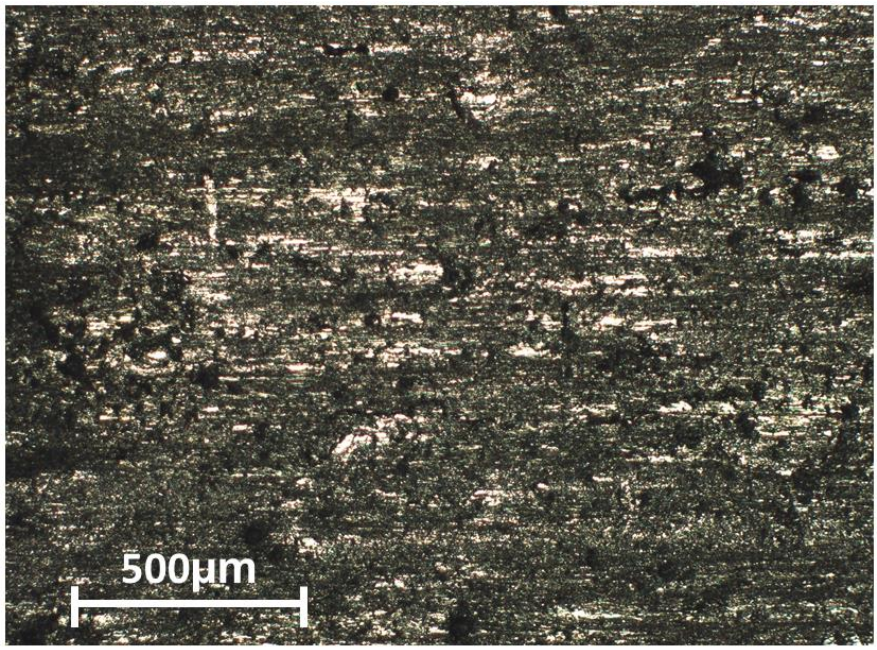

Figure 3.12 - A micrograph of the melt lubrication wear region for a 6061-T6 aluminum slider on 1045 steel guider at a sliding speed of 1,120 m/s and a contact pressure of 135 MPa.

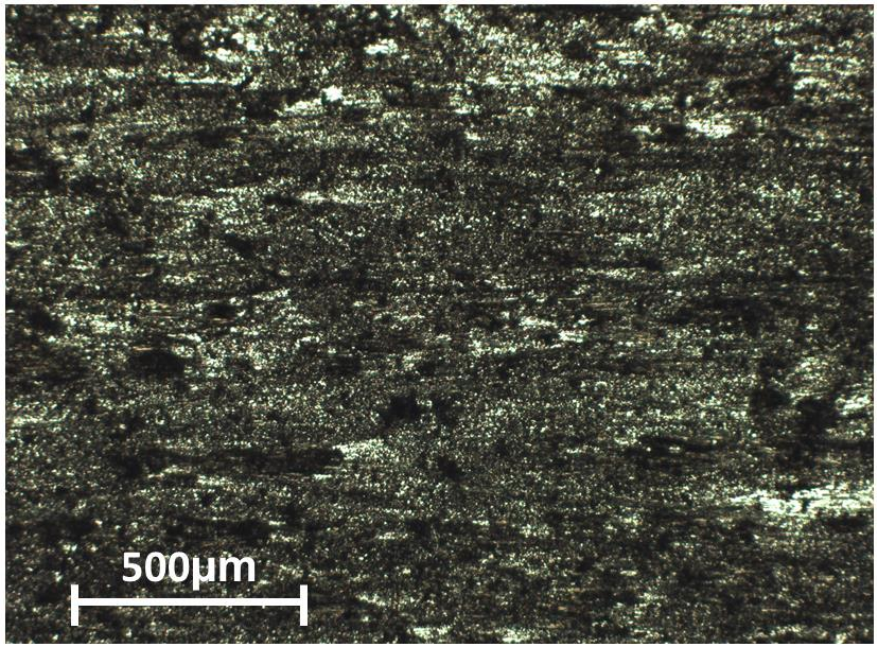

Figure 3.13 - A micrograph of the melt lubrication wear region for a 6061-T6 aluminum slider on titanium commercial purity grade 2 guider at a sliding speed of 1,020 m/s and a contact pressure of 144 MPa.

region has an average thickness between 0.1 – 1 micrometers.

As discussed earlier the development of a melt film capable of supporting large contact loads is considered hydrodynamic in nature and the primary heating mechanism is viscous dissipation. These conditions are representative of melt lubrication, rather than melt wear. The wear mechanism map for aluminum alloys, shown in Figure 3.1, does not differentiate between melt wear and melt lubrication regions. This distinction needs to be recognized. Additionally, the qualitative results show that the seizure wear region needs to be shifted upwards.

3.3 Quantitative Analysis of Slider Deposition

A quantitative assessment was made for each test conducted to develop normalized wear rate relationships as a function of contact pressure, velocity and tribomaterial pairing in the severe plastic deformation and melt lubrication regions. The information obtained from assessing each guider specimen, using optical microscopy, was used to identify three wear regions and to relate those wear regions to the volumetric slider deposition measurements. Based on the analysis conducted using 3D non-contact profilometry there are three inflection points that were identified that correlate well to optical microscopy. These inflection points are shown in Figure 3.14 for the test case of a 6061-T6 aluminum slider on a titanium grade 2 commercial purity guider at a contact pressure of 145 MPa. The first inflection point occurs at the shift from plasticity dominated wear to severe plastic deformation, the second occurs at the peak of the severe plastic deformation wear, and the third occurs at the shift from severe plastic deformation to melt lubrication.

Prior to reaching the first inflection point the normalized wear rate is relatively low and consistent. For the most part the amount of deposited slider material is difficult to measure using the scanning white light interferometer as the volume of deposited material fell within the noise of the guider surface roughness. For this reason only an upper bound could be placed on the normalized wear rates in this region and it is on the order of 10^{-4}.

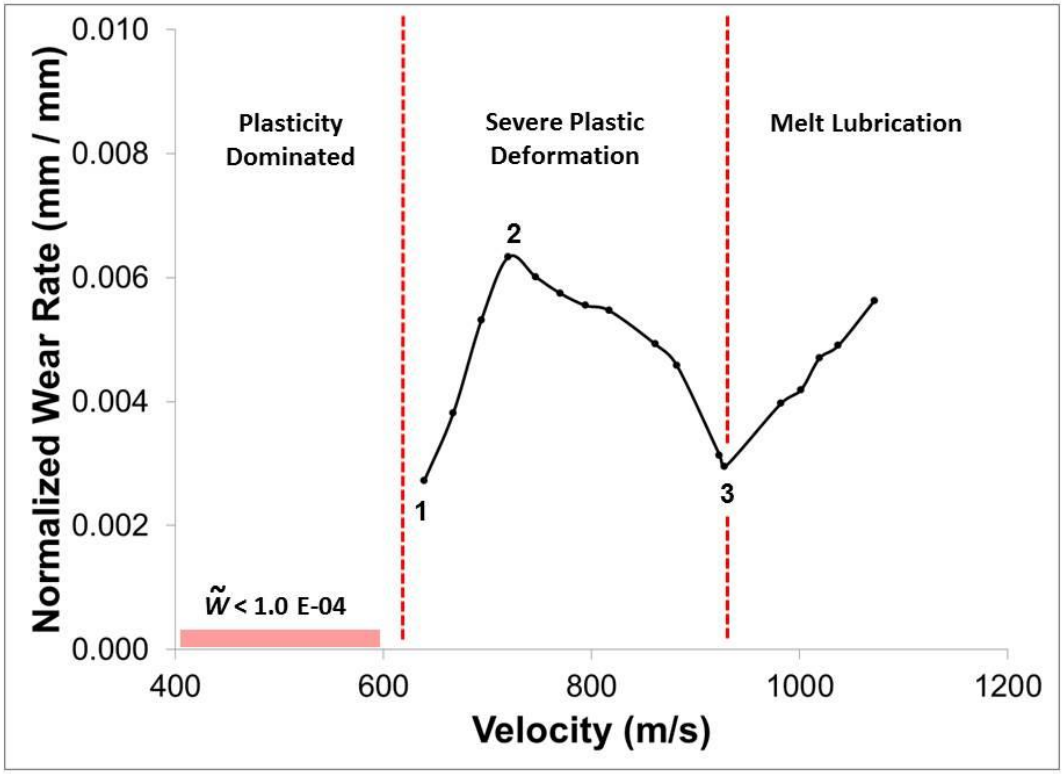

Figure 3.14 - Influence of velocity on normalized wear rate showing three inflection points representing the shift from plasticity dominated wear (1) to severe plastic deformation (2) to melt lubrication (3) for 6061-T6 aluminum on titanium grade 2 commercial purity at 145 MPa.

The low normalized wear rate prior to the first inflection point is representative of localized heating due to frictional effects at the asperity level. As the rate of heat generation increases the temperature gradients between asperities begin to interact, at which point the majority of the slider interface takes on a higher temperature. This causes thermal softening on a large scale and results in larger pieces of worn slider material deposited onto the guider. This is evident in the severe plastic deformation wear micrograph shown in Figure 3.6. The first inflection point signifies this change from localized slider wear to a larger bulk removal of material. From inflection point one to inflection point two, the shearing / plastic deformation that occurs is on a larger scale that eventually reaches a peak as indicated by the second inflection point. At which the normalized wear rate begins to decrease with increasing velocity. The heat dissipation due to the shearing / plastic deformation of these pieces of slider material is large enough to melt the bulk of the slider interface at a sufficient rate to form a melt film capable of supporting the slider normal contact load. This shift from large scale shearing / plastic deformation to a melt film is represented by the third inflection point. Once a melt film has been established the normalized wear rates are representative of melt lubrication and viscous dissipation is the primary heating mechanism.

The melt lubrication region is of particular interest because it had not been identified on the aluminum alloy wear mechanism map previously and its wear rate has a clear relationship with velocity. The melt lubrication region is demarcated by a critical velocity at which the type of wear transitions from severe plastic deformation to melt lubrication, as shown in Figure 3.15. This critical velocity represents the development of a melt film capable of supporting large normal contact loads. A design of experiments to explore the

effects of contact pressure, velocity, and guider material properties on melt lubrication normalized wear rates is discussed in Chapters 4 and 5. Individual normalized wear rate plots as a function of velocity with 95% confidence interval error bars for the wear regions of interest (severe plastic deformation and melt lubrication) are summarized in Appendix A.

Some similarities may be drawn between the normalized wear rate plots as shown in Figures 3.14 and 3.15 to that of a Stribeck curve as shown in Figure 3.16 [14, 57]. The Stribeck curve, named after the German engineer who studied the frictional properties between two sliding lubricated surfaces was developed from a broad set of experiments conducted on journal bearings. The results are typically presented in the form of

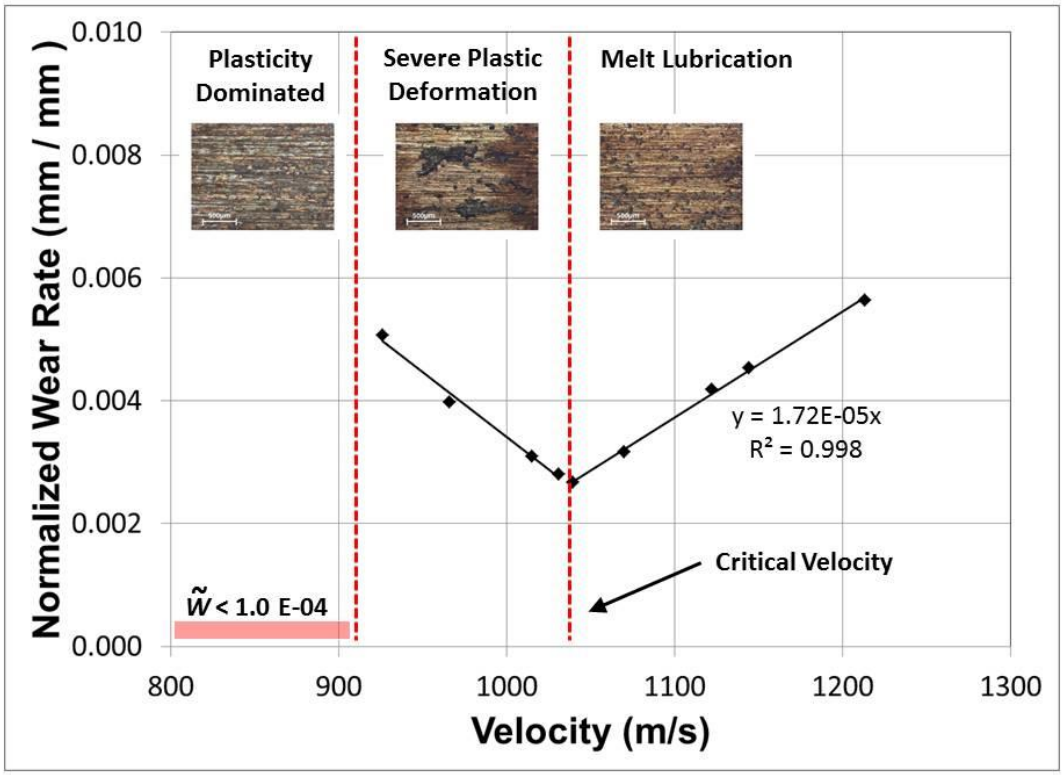

Figure 3.15 - Wear regions and normalized wear rates for 6061-T6 aluminum on C110-H2 copper at 101 MPa.

coefficient of friction, *f*, on the y-axis as a function of dynamic viscosity, μ, rotational speed, *N*, and contact pressure, σ, on the x-axis. The curve itself provides a visualization of the different lubrication regimes encountered and can be used to gain a basic understanding of hydrodynamic lubrication in journal bearings. The actual physical analysis of hydrodynamic lubrication was presented by Petroff and later altered by Sommerfeld and are commonly used in mechanical design of journal bearings [58, 59].

Several different lubrication regimes exist. The hydrodynamic lubrication region is representative of a thick film that separates the two sliding surfaces. This region is

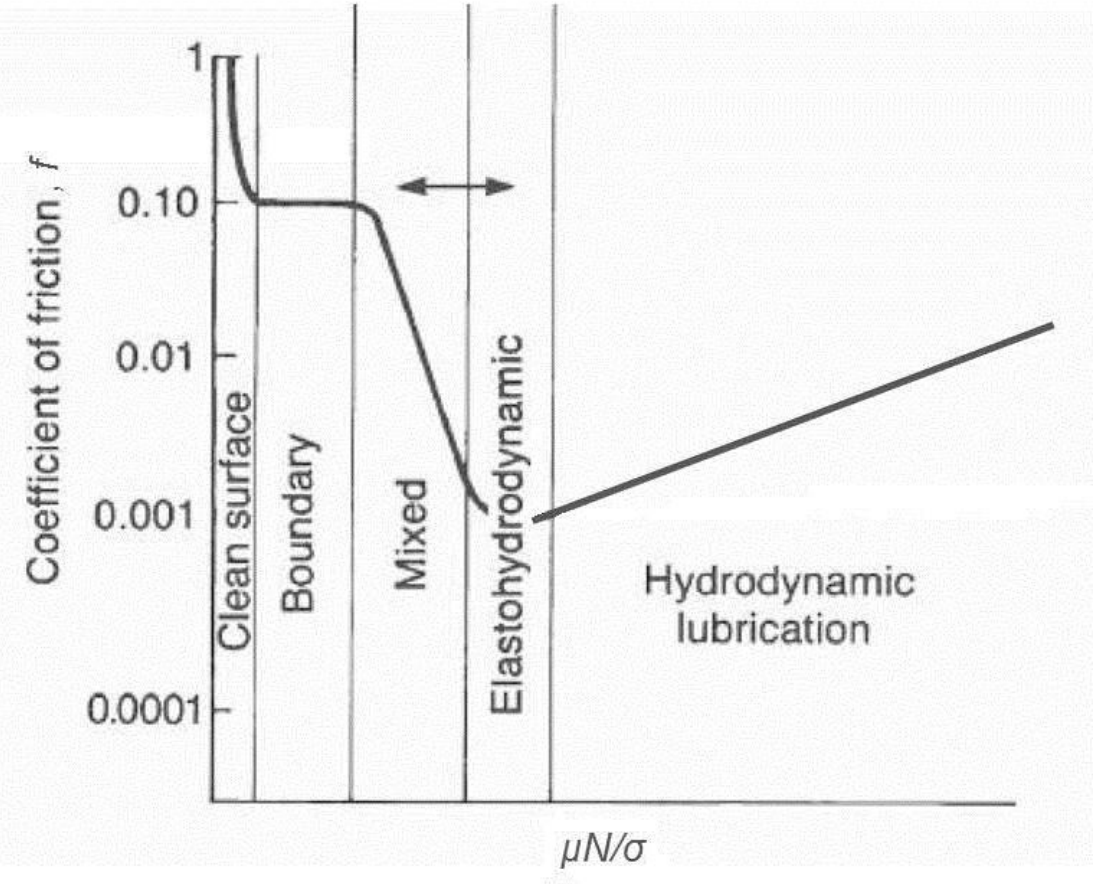

Figure 3.16 - A Stribeck curve representative of the coefficient of friction for the different lubrication regions [14].

demarcated by the inflection point in the elastohydrodynamic region. In typical applications the hydrodynamic lubrication region is the ideal region of operation as it ensures the sliding surfaces are fully separated. This often requires that the lubricant film thickness is much larger than the roughness or irregularities of the sliding surfaces. The friction coefficient in the hydrodynamic region typically increases with increasing sliding speeds due to viscous drag. However, this is not the case in journal bearings where operating in the hydrodynamic region is often self-correcting due to the use of oil as a lubricant. This self-correction has to do with the physical properties of oil as they are sensitive to changes in temperature [60]. For example, an increase in rotational or sliding speed results in an increase in the coefficient of friction and a shift to the right or up the line per the Stribeck curve. This shift to the right results in a higher coefficient of friction due to the viscous / shear drag of the oil. An increase in shear drag results in an increase in the viscous heat dissipation and accordingly a rise in the lubricant temperature. The physical properties of oil are such that an increase in temperature results in a decrease in the dynamic viscosity, as shown in Figure 3.17 [1, 2]. A decrease in dynamic viscosity results in a decrease in the coefficient of friction and causes a shift to the left or down the line. For this reason hydrodynamic lubrication, as it applies to journal bearings, is often considered self-correcting.

In the case of hydrodynamic lubrication or melt lubrication as it pertains to a melting slider, the physical properties of the melt film for molten metals do not possess the same self-correcting properties as oils. As the sliding velocity increases, the shear drag increases and the viscous heat dissipation rate increases, consequently melting more slider material and increasing the thickness of the melt film. Unlike in the self-correcting

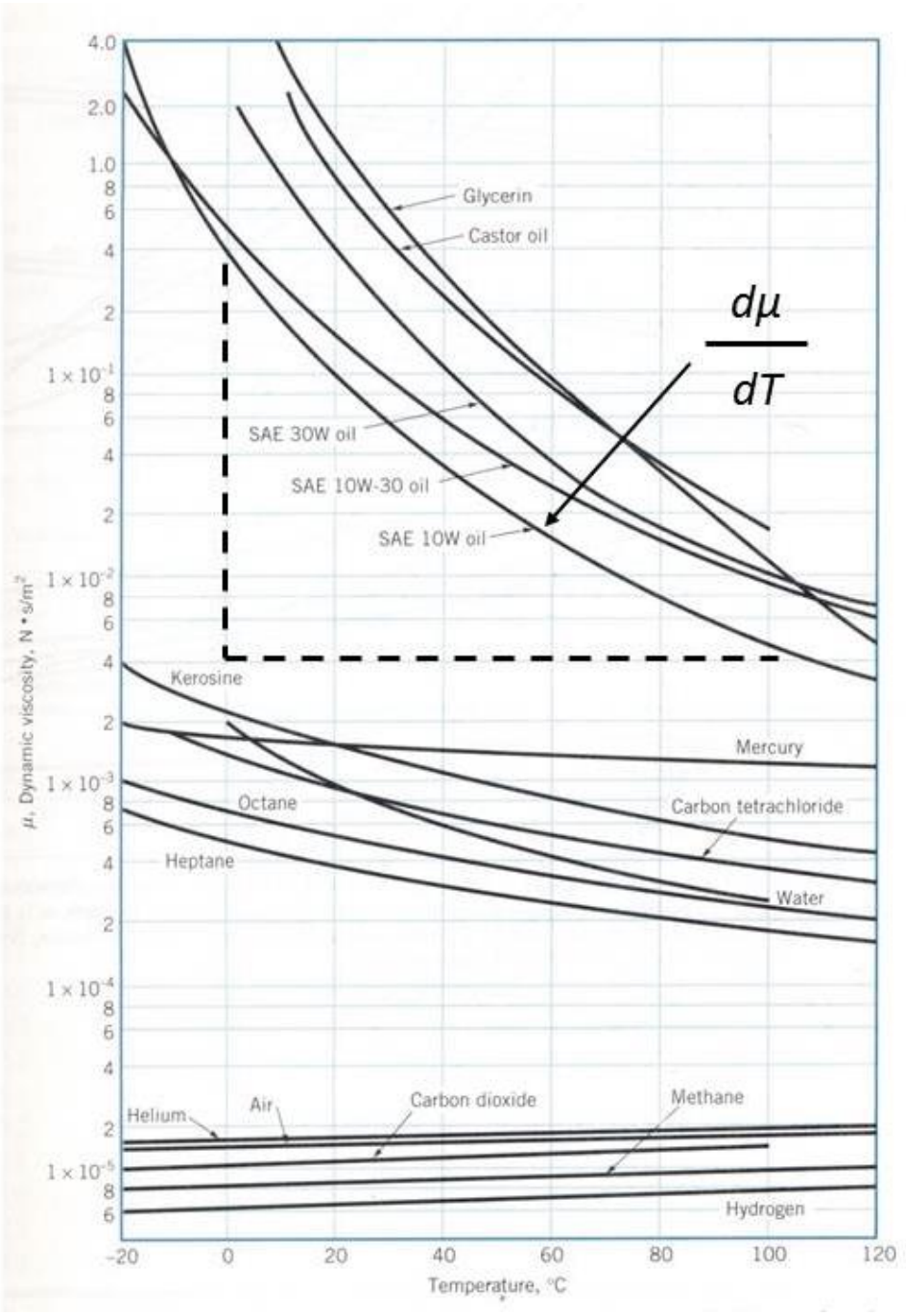

Figure 3.17 - Dynamic viscosity of several different oils and other common fluids as a function of temperature [1, 2].

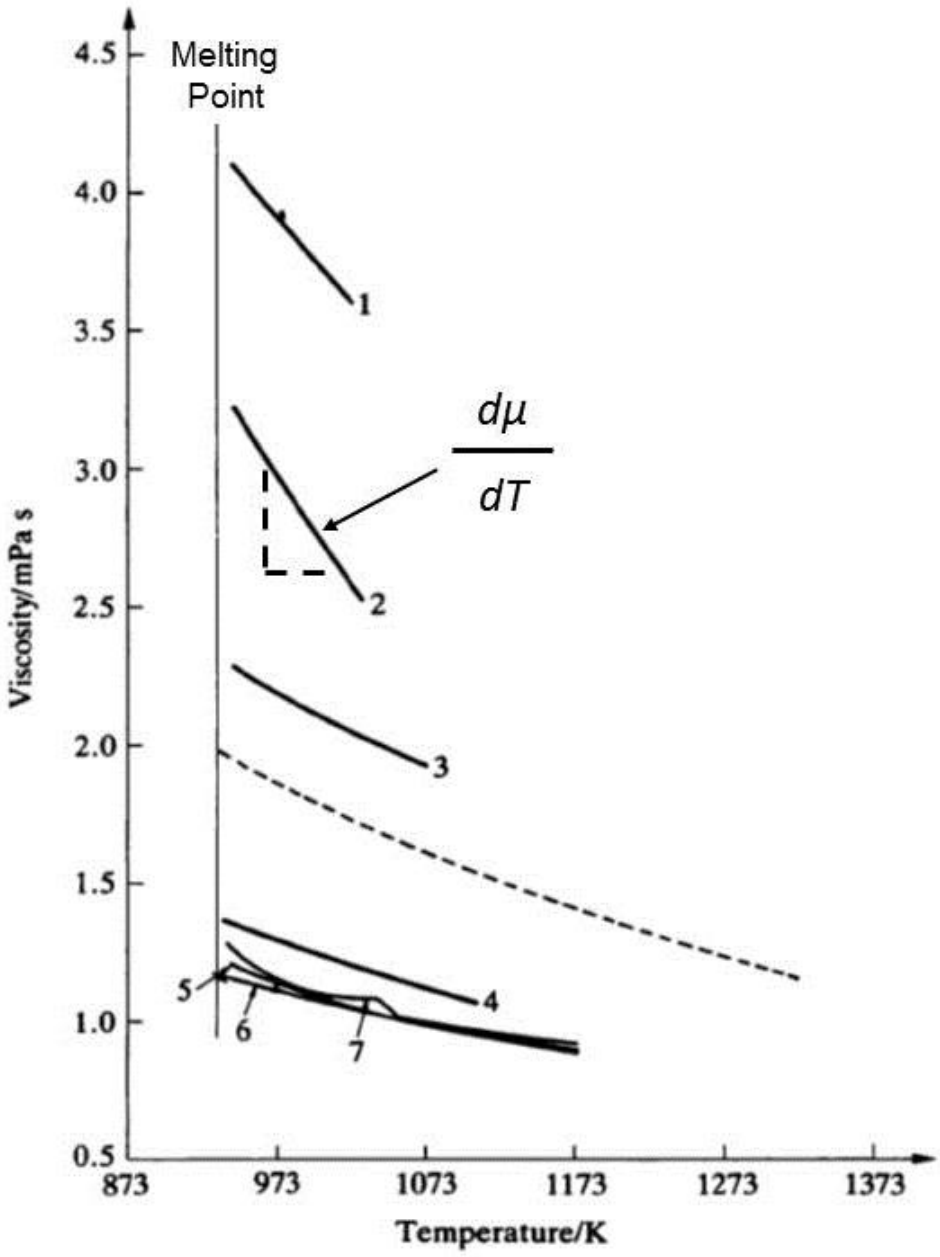

Figure 3.18 - Dynamic viscosity measurements of molten aluminum compiled from seven different sources, labeled 1-7, plotted as a function of temperature [6, 7].

case, the dynamic viscosity of molten aluminum is relatively insensitive to temperature, as shown in Figure 3.18, when compared to typical engine oils [6, 7]. For typical engine oils an increase in temperature of 100ºC results in a decrease in in dynamic viscosity by a factor of 100, whereas as an increase in temperature of 100ºC for molten aluminum results in a decrease in dynamic viscosity by a factor of 1.4. So, as the sliding velocity increases, the viscous heat dissipation rate increases and consequently the slider melt rate increases. This is evident in both the qualitative and quantitative data presented in Figure 3.15 where the normalized wear rate or the amount of slider material deposited on the guider increases linearly with velocity.

A comparison in the trends among the five different lubrication regions of a Stribeck curve and the wear regions identified for a 6061-T6 aluminum slider on a titanium grade 2 commercial purity guider at 145 MPa is made in Figure 3.19. Several assumptions are required and they are as follows:

1) The molten aluminum acts as a Newtonian fluid.
2) The molten aluminum is incompressible.
3) The viscosity of molten aluminum is constant throughout the film.
4) The viscosity of molten aluminum is insensitive to changes in temperature.
5) The normalized wear rate is proportional to the coefficient of friction.
6) The contact pressure at the slider-guider interface is uniform and constant.
7) The normalized wear rate is proportional to the coefficient of friction at the slider-guider interface.
8) No-slip boundary conditions.

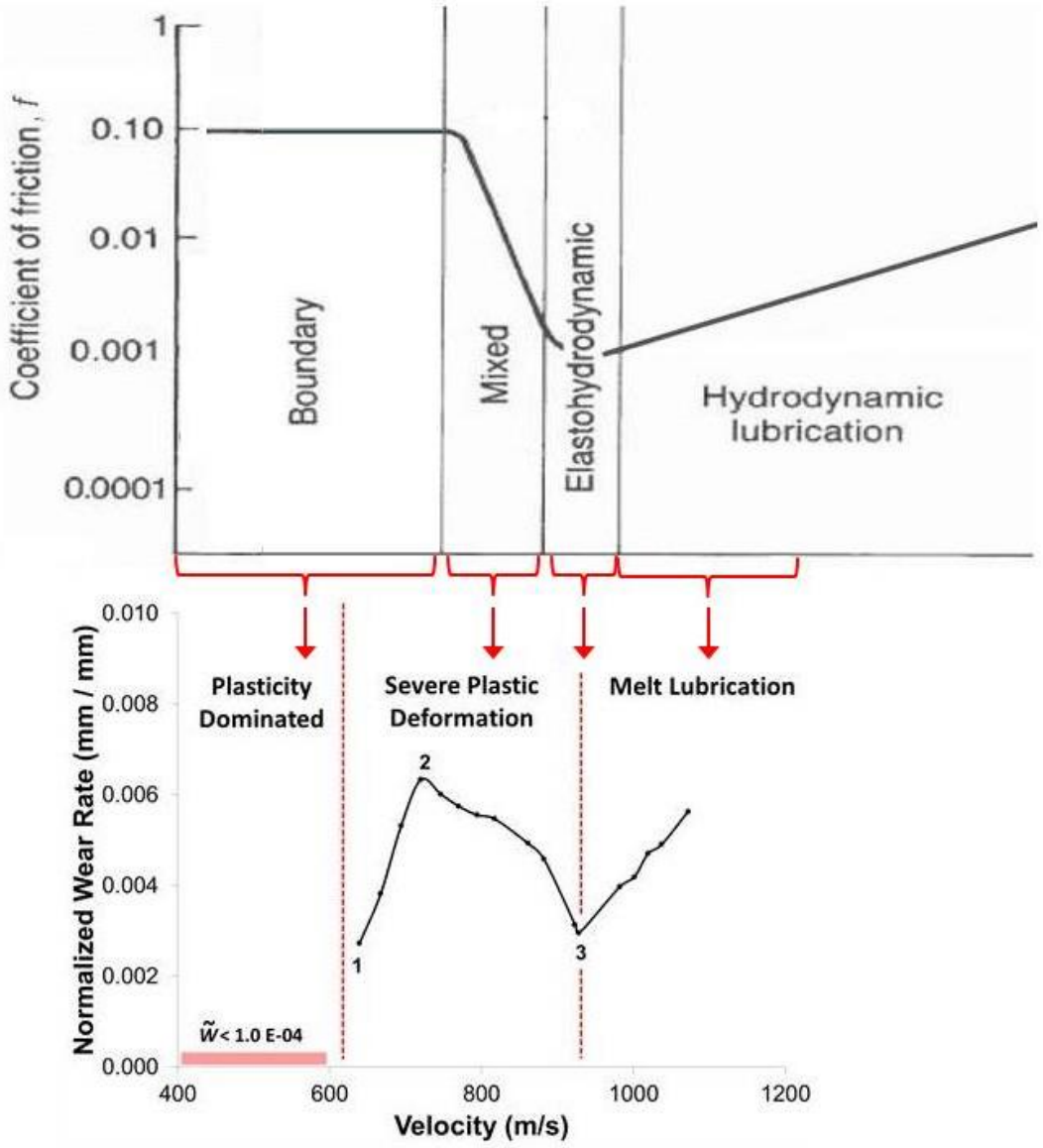

Figure 3.19 - Comparison of a Stribeck curve to a normalized wear rate plot of 6061-T6 aluminum on titanium grade 2 commerical purity at 145 MPa.

The first region of the Stribeck curve is the cleaned surface region. This region is characteristic of high coefficient of friction values that approach unity and can be best correlated to seizure wear. Seizure wear was not identified as one of the three types of wear observed during testing. The second region is the boundary contact region. This region is representative of solid on solid contact at the asperity level, as adhesion is the primary wear mechanism and this region correlates well to the plasticity dominated wear region. The third region, termed mixed lubrication, is representative of partial hydrodynamic lubrication. In this region there is some solid on solid contact between the two sliding surfaces and a portion of the normal contact load is carried by a partially formed lubricant film. The mixed lubrication region correlates well to the severe plastic deformation wear region between the second and third inflection points. As this region is representative of a mixture of solid contact and partial surface separation. Both regions display a similar trend in that the coefficient of friction and normalized wear rates are decreasing with increasing sliding speed. The severe plastic deformation region between the first and second inflection points does not correlate well to the Stribeck curve, because in the Stribeck curve a lubricant is being pumped into the sliding interface. This differs from the high velocity wear experiments where the lubrication is being provided via the melting slider. This transition from localized to large scale melting of the slider occurs between inflection points one and two and consequently does not correlate well to a particular region of the Stribeck curve.

The fourth region, elastohydrodynamic lubrication (EHL), is a subset of hydrodynamic lubrication. In the EHL region the film is thinner than that of the hydrodynamic lubrication region. The EHL region correlates well with the third

inflection point as it has been shown that the melting rate of the slider is sufficient enough to maintain a thin film. Lastly, the fifth region, the hydrodynamic lubrication region, is representative of thick film lubrication and is located beyond the third inflection point in the melt lubrication region. These two regions correlate well as slider deposition in the melt lubrication region is indicative of a thicker melt lubrication film, which is representative of full slider-guider separation.

It is concluded that portions of the severe plastic deformation and melt lubrication regions followed similar trends to that of the mixed, EHL and hydrodynamic lubrication regions of a Stribeck curve. Several wear models have attempted to predict the melting rate of the slider in the melt lubrication region. The basis for these models is Stiffler's melt lubrication model which is constructed on the concept of laminar flow [36]. Stefani and Kothmann tried to apply Stiffler's melt lubrication model to high velocity wear data and found that the assumption of laminar flow under predicted the slider wear rate and that a larger molten aluminum viscosity value provided better results [41]. It was concluded that a higher effective viscosity is necessary to better predict the melting rates under these conditions. This conclusion indicates that the film could be better represented by a slurry or that turbulence needs to be accounted for when modeling the melt film. Stefani and Merrill investigated the effects of turbulence in thin films [42]. They utilized the Reynold's Number to provide further insight into whether or not the melt film is operating in the laminar or turbulent regime. The Reynold's Number for a thin film is defined as follows

$$Re = \frac{inertial\ forces}{viscous\ forces} = \frac{\rho v h}{\mu} \tag{3.3}$$

where v is the slider velocity, h is the film thickness, μ is the dynamic viscosity and ρ is the liquid density of aluminum at the melting point. Using the sliding conditions and molten aluminum material properties, as shown in Table 3.3, a Reynold's Number of approximately 12,000 is calculated [6, 7]. Stefani and Merrill found the transition from laminar to turbulent flow in journal bearings to be as low as 2,000 [61]. So, for the sliding conditions in the melt lubrication region the fluid film may be considered turbulent, which provides added complexity when analyzing the slider-guider contact interface.

Table 3.3 - Typical sliding conditions and material properties of molten aluminum in the melt lubrication region

v (m/s)	h (m)	μ (Pa·s)	ρ (kg/m^3)
1,000	10^{-5}	0.002	2375

CHAPTER 4: Experimental Results – Velocity and Pressure

4.1 Overview

A set of experiments was designed to explore the effects of velocity and contact pressure on slider wear. Additional considerations such as the effects of the tribomaterial pairing are discussed in Chapter 5. For the modified EML experimental setup the peak sliding velocity is typically between 1,150 – 1,250 m/s and the critical velocity at which the type of wear shifts from severe plastic deformation to melt lubrication is in the range of 800 – 1,000 m/s. This leaves approximately 10 – 25 centimeters of slider deposition to analyze. Pressures in the range of 120 – 180 MPa were targeted as this pressure range provides an extension of previous work conducted by Stefani and Parker [4]. The material pairing is held constant, utilizing a 6061-T6 aluminum slider on a C110-H2 guider as these materials are relevant to small caliber EML systems [62-66]. Additionally, the effect of nominal contact area is explored. The results presented in this chapter are in standard format with the normalized wear rate on the y-axis and the operating parameters or test conditions such as velocity on the x-axis. Data analysis combined with high velocity wear theory is utilized to plot the data in an insightful form. A design of experiments to study the effects of pressure and velocity on slider normalized wear rates is discussed.

4.2 Design of Experiments

A design of experiments to study the effects of high sliding speeds and high contact pressures on slider wear is explored. The test conditions achieved are limited by the EML system power supply and bore geometric constraints. The design space for the tribometer

is shown in Figure 4.1. Several different contact pressures were targeted within this design envelope. A comparison of the five targeted and measured pressures and test parameters is made in Table 4.1. Differences occurred for two primary reasons. The first has to do with the repeatability of the Georgia Tech minor caliber EML system. Several different electrical connections are made between the power supply and the EML bore. Assembly and disassembly of these connections is required for maintenance and can lead to different electrical contact resulting in variability in the electrical current passing through the system. This variability directly impacts the electromagnetic propulsive force on the launch package, consequently causing the acceleration, in some instances, to dip below the targeted value.

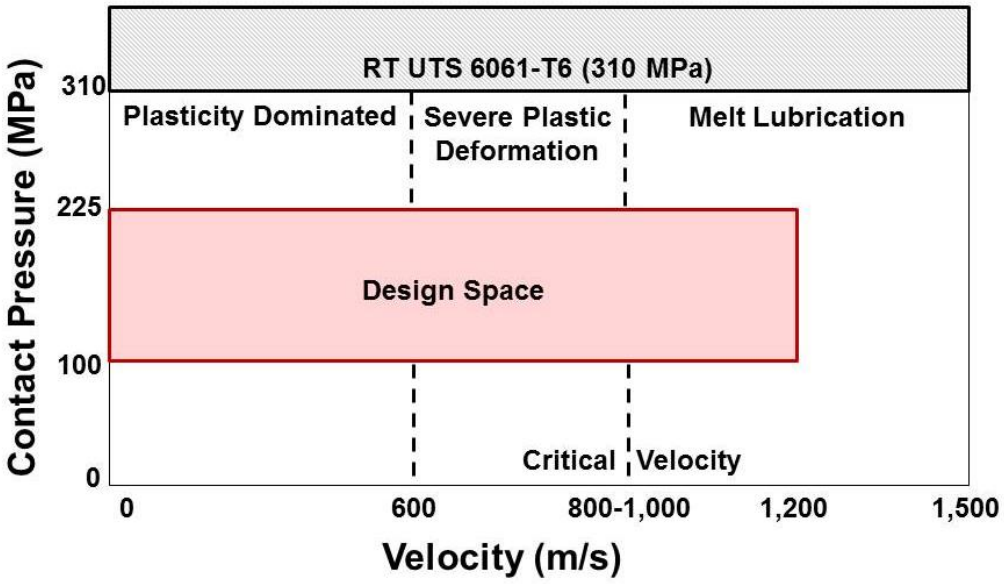

Figure 4.1 - Design space for the Georgia Tech minor caliber EML and tribometer design for a 6061-T6 aluminum slider on C110-H2 guider.

Table 4.1 - Summary of the targeted and measured wedge mass, acceleration and contact pressures.

Test No.	Targeted Conditions			Measured Conditions		
	Wedge Mass (g)	Accel. (m/s^2)	Pressure (MPa)	Wedge Mass (g)	Accel. (m/s^2)	Pressure (MPa)
1	0.347	1.60E6	120	0.286	1.64E6	101
2	0.240	1.60E6	140	0.240	1.40E6	122
3	0.405	1.60E6	140	0.362	1.60E6	124
4	0.463	1.60E6	160	0.396	1.52E6	130
5	0.520	1.60E6	180	0.640	1.63E6	225

The second difficulty in replicating the target contact pressures has to do with the fabrication process. Additional mass in the form of a tungsten pin was added to each wedge to vary the mass and accordingly the contact pressure. The tungsten pin was added by drilling a blind hole into each wedge, cutting a pin to size and press fitting it into the hole. The relative size of each individual wedge coupled with tolerancing and the addition of a tungsten pin made a noticeable impact on the final wedge mass, which subsequently has an effect on the calculated pressure.

This combination of EML system performance and wedge fabrication generated a variability that made it difficult to precisely meet the targeted contact pressures during actual testing as indicated by the differences in Table 4.1 For all tests the contact area was square (aspect ratio of one). It is important to note that test number 2 maintained a square shape, but had a 41% reduction in the contact area from tests 1 and 3-5 and the wedge mass was adjusted accordingly to achieve the targeted contact pressure.

Additionally test number 5 had a much larger mass than expected due to a deeper blind hole and a larger tungsten pin.

A summary of the material pairing, contact pressure, peak velocity and nominal contact area for each of the five tests is displayed in Table 4.2. An even distribution of contact pressures was difficult to achieve due to the aforementioned issues, however the distribution is sufficient as the lower and upper bounds, 101 MPa and 225 MPa, of the design space were achieved and additional intermediary pressures were attained providing enough data to adequately capture the sensitivity of contact pressure on normalized wear rates. Additionally the peak velocity for the five tests are within 10-20 m/s of the targeted 1,200 m/s and the velocity range of 600 – 1,200 m/s was properly captured such that the severe plastic deformation and melt lubrication regions can be explored.

Table 4.2 - Summary of test conditions to study the effects of pressure and velocity on slider wear.

Test No.	Slider Material	Guider Material	Contact Pressure (MPa)	Peak Velocity (m/s)	Nominal Contact Area (mm^2)
1	6061-T6	C110-H2	101	1210	10.1
2	6061-T6	C110-H2	122	1180	5.8
3	6061-T6	C110-H2	124	1210	10.1
4	6061-T6	C110-H2	130	1190	10.1
5	6061-T6	C110-H2	225	1180	10.1

4.3 Experimental Results

4.3.1 Overview

The test results presented and discussed in this section focus on the melt lubrication region. A broad survey of slider deposition measurements is taken as to properly identify the critical velocity to adequately capture the melt lubrication region. A normalized wear rate plot for the melt lubrication region of a 6061-T6 aluminum slider on a C110-H2 copper guider at five different contact pressures is shown in Figure 4.2. The normalized wear rates exhibit a dependence on both pressure and velocity. The critical velocity, v_c, at which the wear transitions from severe plastic deformation to melt lubrication is sensitive

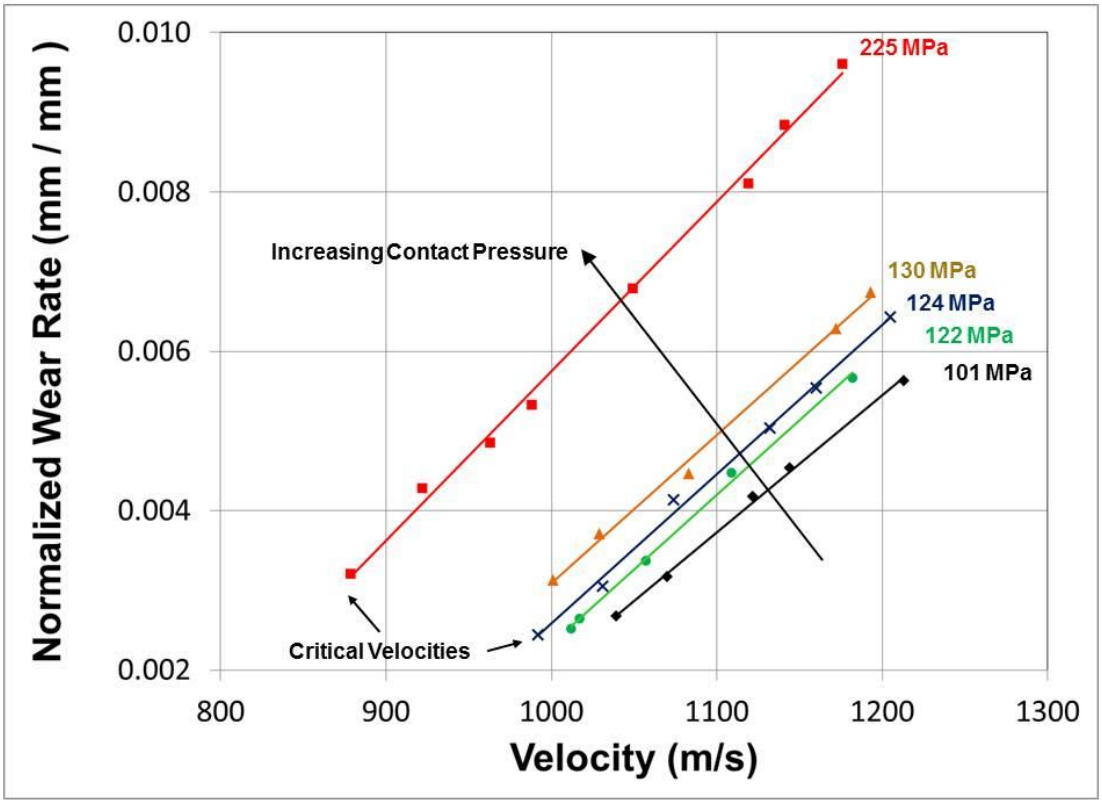

Figure 4.2 - Melt lubrication test data for a 6061-T6 aluminum slider on C110-H2 guider with varying contact pressure.

to pressure. The critical velocity decreases with increasing pressure. After the critical velocity is achieved the normalized wear rate increases linearly with velocity. This suggests that the rate of heat dissipation is directly related to the viscous drag and subsequently velocity. Additionally, while it is difficult to visually identify, secondary pressure effects are present in the slope of each line. These effects are summarized in Table 4.3. An increasing contact pressure results in an increase in the slope. In the next section the effects of pressure and velocity are understood utilizing melt lubrication theory, which provides a means to develop an empirical model for predicting slider wear.

Table 4.3 - Influence of pressure and velocity effects on the slope of normalized wear rates in the melt lubrication region for a 6061-T6 slider on a C110-H2 guider.

Test No.	σ (MPa)	v_c (m/s)	Slope, m x 10^{-5}
1	101	1039	1.72
2	122	1012	1.87
3	124	992	1.87
4	130	1001	1.86
5	225	879	2.13

4.3.2 Analysis: Melt Lubrication Theory

Melt lubrication theory is used to provide insight in analyzing the experimental data. A melt lubrication model for a fully melting slider and a laminar viscous heat source was developed by Stiffler [36]. Stiffler utilized the Reynold's equation (momentum and

continuity) in conjunction with the heat equation to evaluate and predict melting rates. Several assumptions are made and they are

1) Molten metal lubricant is laminar and incompressible
2) The pressure, density and viscosity are constant across the film thickness
3) Molten metal film thickness is small relative to the slider geometry
4) Only the slider is melting
5) Quasi-steady state conditions are reached in the molten film

The normalized wear rate for a laminar melt lubrication film according to Stiffler is defined

$$\widetilde{W} = \frac{\sigma^{\frac{1}{4}} \cdot (\mu v)^{\frac{1}{2}}}{l^{\frac{1}{2}} \cdot \delta^{\frac{1}{4}} \cdot \rho^{\frac{3}{4}} \cdot [L + c(T_m - T_o)]^{\frac{3}{4}}} \tag{4.1}$$

where σ is the nominal contact pressure, μ is the dynamic viscosity, v is the slider velocity, l is the slider length, δ is a geometric factor, ρ is the room temperature mass density, L is the latent heat of fusion, c is the specific heat, T_m is the melting point, and T_o is the initial temperature. The thermal properties are those of the melting slider. The geometric factor [36] is defined

$$\delta = 1 - \frac{192}{\pi^5 \cdot \zeta} \sum_{n=1,3,5}^{\infty} n^{-5} \tanh\left(\frac{n \cdot \pi \cdot \zeta}{2}\right) \tag{4.2}$$

where ζ is the aspect ratio of the slider contact area (length divided by the width).

Equation 4.1 suggests that the normalized wear rate is proportional to the nominal contact pressure and sliding velocity raised to the ¼ and ½ powers, respectively. The data presented in Figure 4.2 is re-plotted as a function of $\sigma^{1/4}v^{1/2}$ in Figure 4.3. The results do not appear to correlate well as a good correlation would "collapse" the data onto a single line. As discussed in Chapter 3 an inherent uncertainty lies in the assumption of laminar flow and it has been shown that the melt lubrication film may operate in the turbulent

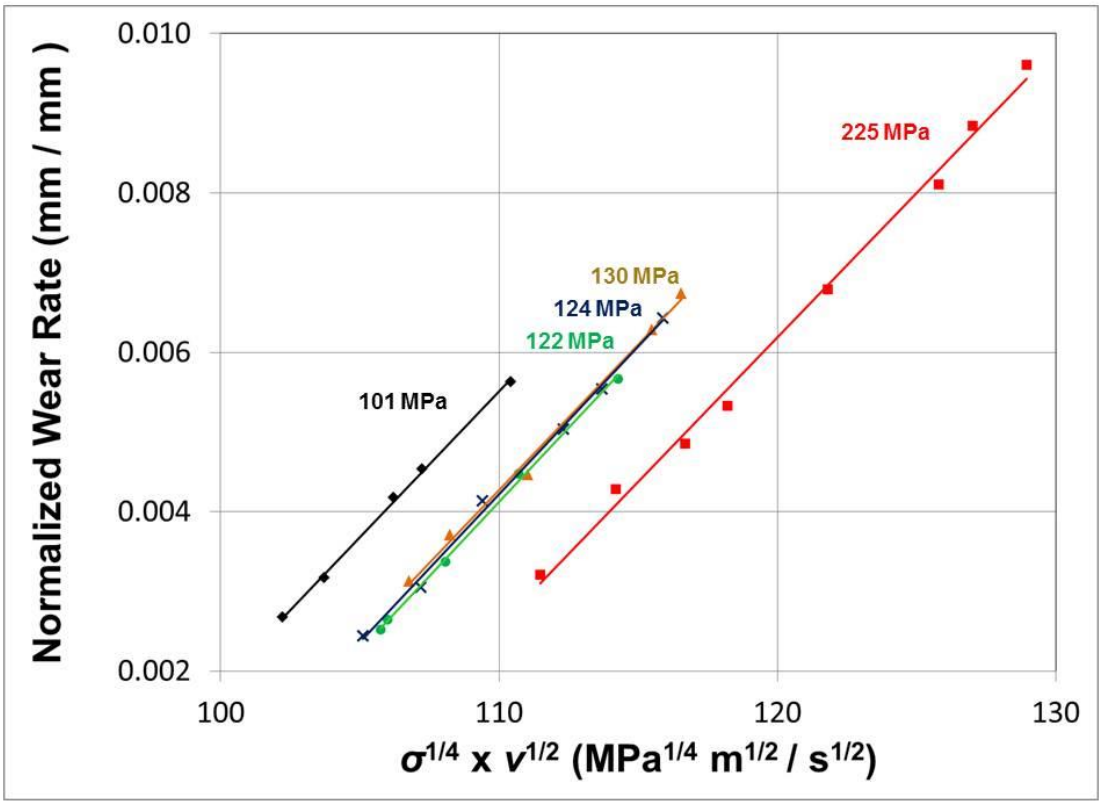

Figure 4.3 - Melt lubrication test data for a 6061-T6 aluminum slider on C110-H2 guider as a function of $\sigma^{1/4}v^{1/2}$.

regime. A turbulent melt lubrication film can have a strong dependence on velocity and therefore these effects need to be considered [42, 67].

Based on these results it is assumed that the molten metal film is turbulent and that the viscosity exhibits a linear dependence on velocity [2, 42]. The turbulent viscosity is defined

$$\mu_{turbulent} = \lambda \cdot v + \mu_{laminar} \tag{4.3}$$

where λ is the turbulent viscosity constant, v is velocity and $\mu_{laminar}$ is the laminar viscosity. For high velocities, the first term dominates and the turbulent viscosity is reduced

$$\mu_{turbulent} = \lambda \cdot v \tag{4.4}$$

Substituting Equation 4.3 into 4.1 the normalized wear rate for a turbulent melt film is defined

$$\widetilde{W} = \frac{\lambda^{\frac{1}{2}} \cdot \sigma^{\frac{1}{4}} \cdot v}{l^{\frac{1}{2}} \delta^{\frac{1}{4}} \rho^{\frac{3}{4}} [L + c(T_m - T_o)]^{\frac{3}{4}}} \tag{4.5}$$

It is important to note that the geometry terms, l and δ are constant for a fixed slider geometry. These terms can be represented by a single geometry constant,

$$G = \frac{1}{l^{\frac{1}{2}}\delta^{\frac{1}{4}}} \tag{4.6}$$

As the slider thermal terms, ρ, L, c, T_m, and T_o, are representative of the energy required to melt the slider material, these terms can be represented by a single thermal constant,

$$\Gamma = \frac{1}{\rho^{\frac{3}{4}}[L + c(T_m - T_o)]^{\frac{3}{4}}} \tag{4.7}$$

Combining Equations 4.5, 4.6, and 4.7 a simplified form for the normalized wear rate for a turbulent melt film is

$$\widetilde{W} = \lambda^{\frac{1}{2}} \cdot G \cdot \Gamma \cdot \sigma^{\frac{1}{4}} \cdot v \tag{4.8}$$

When the data in Figure 4.2 is re-plotted as a function of $\sigma^{1/4}v$, as shown in Figure 4.4, the lines of constant pressure "collapsed" onto a single line and the slope of each line is now representative of the viscosity, geometry and thermal constants λ, G, and Γ, collectively referred to as the melt lubrication proportionality constant Ψ defined by

$$\Psi = \lambda^{\frac{1}{2}} \cdot G \cdot \Gamma \tag{4.9}$$

Substituting Equation 4.9 into 4.8

$$\widetilde{W} = \Psi \cdot \sigma^{\frac{1}{4}} \cdot v \tag{4.10}$$

This simplified form is useful when analyzing the experimental data as the slope of each line is representative of the melt lubrication proportionality constant. A comparison of the melt lubrication proportionality constants for each set of data and the associated percent difference from the data set average is summarized in Table 4.4.

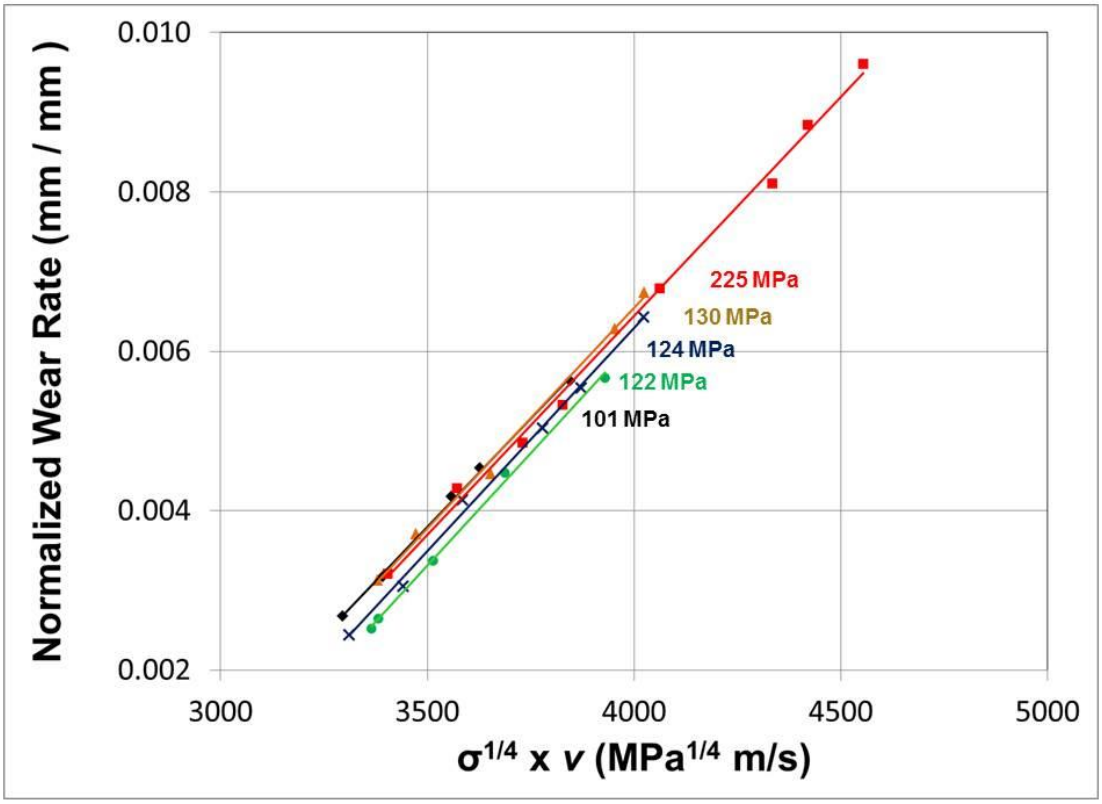

Figure 4.4 - Melt lubrication test data for a 6061-T6 aluminum slider on C110-H2 guider as a function of $\sigma^{1/4}v$.

Table 4.4 - A comparison of the melt lubrication proportionality constants for the 6061-T6 slider on a C110-H2 guider data set.

Test No.	σ (MPa)	Ψ $(\lambda^{1/2} \cdot G \cdot \Gamma) \times 10^{-6}$	% Diff.
1	101	5.44	1.7
2	122	5.62	1.5
3	124	5.60	1.2
4	130	5.53	0.1
5	225	5.49	0.8
Average	---	5.54	---

A linear fit is made using the complete set of data in Figure 4.5. These results support the use of melt lubrication with turbulence as the normalized wear rates are sensitive to $\sigma^{1/4}v$. The effective turbulent viscosity of the melt lubrication film is calculated using the melt lubrication proportionality constant of the fit data in Figure 4.5 and calculating the geometric and thermal constants using Equations 4.6 and 4.7 and the material property data in Table 4.5 [5-7, 9, 36]. Solving for the turbulent viscosity constant, λ, using Equations 4.9, a value of 8.6 $Pa \cdot s^2$ / m is calculated. For a viscosity constant of 8.6 $Pa \cdot s^2$ / m and a velocity range from 1,000 – 1,200 m/s an effective turbulent viscosity of 8.6 – 10.3 x 10^3 Pa·s is calculated using Equation 4.4. The effective turbulent viscosity is six orders of magnitude larger than that of molten aluminum 2.0 x 10^{-3} Pa·s without turbulent effects included. This demonstrations the effect that turbulence has on normalized wear rates in the melt lubrication film. Modeling of this film using the assumption of laminar

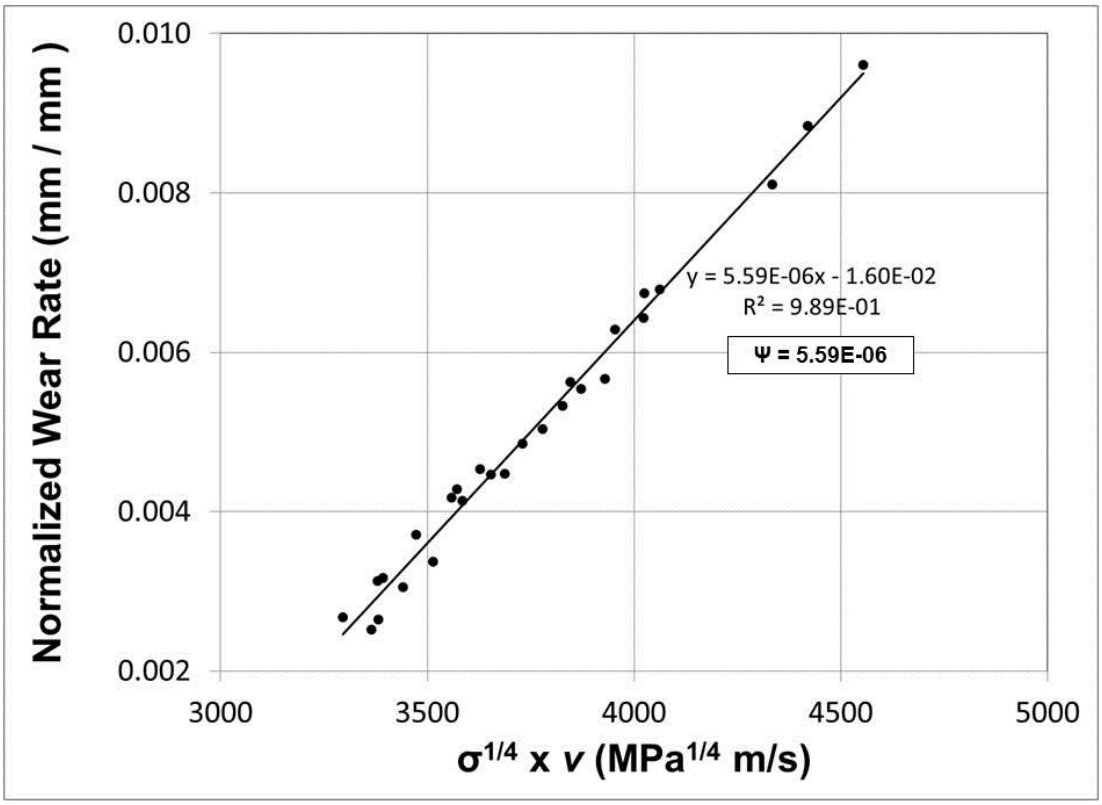

Figure 4.5 - A linear fit of complete data set for a 6061-T6 aluminum slider on C110-H2 guider as a function of $\sigma^{1/4}v$.

Table 4.5 - Material properties and slider geometry used to calculate G·Γ.

Material Property	6061-T6
ρ, density at RT (kg/m^3)	2,700
L, heat of fusion (kJ/kg)	398
c, specific heat (J/kg K)	897
T_m, melting point (°C)	660
T_o, ambient temperature (°C)	25
l, slider length (mm)	3.18
w, slider width (mm)	3.18
δ, geometric correction factor	0.42

Table 4.6 - Melt lubrication constants.

Constant	6061-T6
Ψ, melt lubrication proportionality (s / m $MPa^{1/4}$)	5.59×10^{-6}
G, geometric constant (1 / $m^{1/2}$)	22.0
Γ, thermal constant (1 / $Pa^{3/4}$)	8.65×10^{-8}
λ, viscosity constant (Pa s^2 / m)	8.6

flow (no turbulence) will significantly under predict the normalized wear rates in the melt lubrication region.

Additionally, the melt lubrication model of Equation 4.5 assumes that all of the heat generated in the melt film is partitioned into the slider. This may not be appropriate as the guider acts as a heat sink, removing heat from the melt lubrication film. These effects are captured through the turbulent viscosity constant, which is adjusted to calibrate the melt lubrication model to the experimental data.

4.3.3 Analysis: Empirical Modeling

Experimental data from the tests of varying pressure show that the critical velocity or the velocity at which the type of wear transitions from severe plastic deformation to melt lubrication is sensitive to contact pressure. The larger the contact pressure, the lower the critical velocity. As discussed in section 4.3.2 the effects of pressure can be removed by plotting the normalized wear rates as a function of pressure and velocity ($\sigma^{1/4}v$). A critical value of $\sigma^{1/4}v$, referred to as the critical heat dissipation, A, exists and represents the shift from severe plastic deformation to melt lubrication. A comparison of the critical heat

dissipation for each set of data and the associated percent difference from the data set average is summarized in Table 4.7.

Table 4.7 - Comparison of the critical heat dissipation values.

Test No.	σ (MPa)	v_c (m/s)	A (MPa$^{1/4}$·m/s) x 10^3	% Diff.
1	101	1039	3.30	1.7%
2	122	1012	3.36	0.4%
3	124	992	3.31	1.2%
4	130	1001	3.38	0.9%
5	225	879	3.40	1.6%
Average	---	---	3.35	---

The average *A* value shown in Table 4.7 is empirically derived and represents the conditions at which the heat dissipation is significant enough to develop a melt film. The critical velocity for a given contact pressure can be calculated as follows

$$v_c = \frac{A}{\sigma^{\frac{1}{4}}} \tag{4.11}$$

where *A*, is the critical heat dissipation and σ, is the contact pressure. For a tribomaterial pairing of a 6061-T6 aluminum slider on a C110-H2 guider and a contact pressure in the range of 100 – 225 MPa the critical velocity at which the wear shifts from severe plastic deformation to melt lubrication can be predicted.

Table 4.8 - Comparison of the normalized wear rates at the critical velocity.

Test No.	σ (MPa)	v_c (m/s)	$\widetilde{W}_c$ x 10^{-3}
1	101	1039	2.67
2	122	1012	2.52
3	124	992	2.44
4	130	1001	3.13
5	225	879	3.20

In addition to the sensitivity of the critical velocity on contact pressure, the normalized wear rate at the critical velocity displays a dependence on pressure, as shown previously in Figure 4.2. A large pressure results in a higher normalized wear rate at the critical velocity. The normalized wear rate at the critical velocity, $\widetilde{W}_c$ for each data set is summarized in Table 4.8. A similar methodology used to define the critical heat dissipation is employed here to define the critical normalized wear rate, *B*. The significance of *B* is that it captures the pressure effects on the normalized wear rate at the critical velocity. In order to properly define *B* a dimensionless pressure ratio, σ_r, is defined

$$\sigma_r = \frac{\sigma}{\sigma_o} \tag{4.12}$$

where σ, is the nominal contact pressure, and σ_o is the reference contact pressure, which for this case is 101 MPa and represents the lower bound of the pressures tested. The critical normalized wear rate, *B*, is defined

$$B = \frac{\widetilde{W}_c}{\sigma_r{}^{\frac{1}{4}}} \tag{4.13}$$

Similar to the critical heat dissipation parameter, the dimensionless pressure ratio is raised to the ¼ power as this parameter is of significance in melt lubrication theory. A comparison of the critical normalized wear rates, *B*, for each set of data and the associated percent difference from the data set average is summarized in Table 4.9.

Table 4.9 - Comparison of the critical normalized wear rates, *B*.

Test No.	σ (MPa)	σ_r	$\sigma_r^{1/4}$	$\widetilde{W}_c$ x 10^{-3}	*B* x 10^{-3}	% Diff.
1	101	1.00	1.00	2.67	2.67	3.1
2	122	1.21	1.05	2.52	2.40	7.2
3	124	1.23	1.05	2.44	2.32	10.5
4	130	1.29	1.07	3.13	2.94	13.5
5	225	2.23	1.22	3.20	2.62	1.1
Average	---	---	---	---	2.59	---

The transition from severe plastic deformation to melt lubrication was difficult to capture quantitatively. This required that the normalized wear rate at the critical velocity was estimated using the intersection of the linear fit of the experimental data in the severe

plastic deformation and melt lubrication regions. The differences between the critical normalized wear rates, *B*, and the data set average in Table 4.9 can be attributed to variability in the linear fit of each wear region as they are sensitive to the number of data points used to create the fit and the uncertainty in each normalized wear rate measurement.

An empirical normalized wear rate equation, derived from Equation 4.10, in a general form as a function of the sliding speed and contact pressure is derived using the following linear expression

$$\widetilde{W} = \Psi \cdot \sigma^{\frac{1}{4}} \cdot v + b \tag{4.14}$$

Using the boundary conditions at the critical velocity,

$$b = \widetilde{W}_c - \Psi \cdot \sigma^{\frac{1}{4}} \cdot v_c \tag{4.15}$$

Substituting Equation 4.11 - 4.13 into Equation 4.15

$$b = B \cdot \left(\frac{\sigma}{\sigma_o}\right)^{\frac{1}{4}} - \Psi \cdot \sigma^{\frac{1}{4}} \cdot \frac{A}{\sigma^{\frac{1}{4}}} \tag{4.16}$$

Substituting Equation 4.16 into Equation 4.14 and rearranging terms gives way to an empirical normalized wear rate equation

$$\widetilde{W} = \Psi \cdot \left(\sigma^{\frac{1}{4}} \cdot v - A\right) + B \cdot \left(\frac{\sigma}{\sigma_o}\right)^{\frac{1}{4}} \tag{4.17}$$

This equation is capable of replicating lines of constant pressure using the constants Ψ, A, B and σ_o. A summary of the constants and their mean values is given in Table 4.10. The equation is applicable for velocities in the melt lubrication region ($v_c \leq v \leq 1{,}200$ m/s) and pressures in the range of 100 – 225 MPa for a 6061-T6 aluminum slider on C110-H2 guider.

Table 4.10 - Normalized wear rate equation constant and mean values.

Constant	Average Value	95% Confidence Interval
Ψ, melt lubrication proportionality constant (s / m $MPa^{1/4}$)	5.54E-06	0.15 x 10^{-6}
A, heat dissipation rate ($MPa^{1/4}$ m / s)	3,350	94
B, critical normalized wear rate	2.59E-03	0.49x 10^{-3}
σ_o, reference contact pressure (MPa)	101	---

A plot of the predicted lines of constant pressure using the normalized wear rate model and mean constant values for contact pressures of 101, 122, 124, 130, and 225

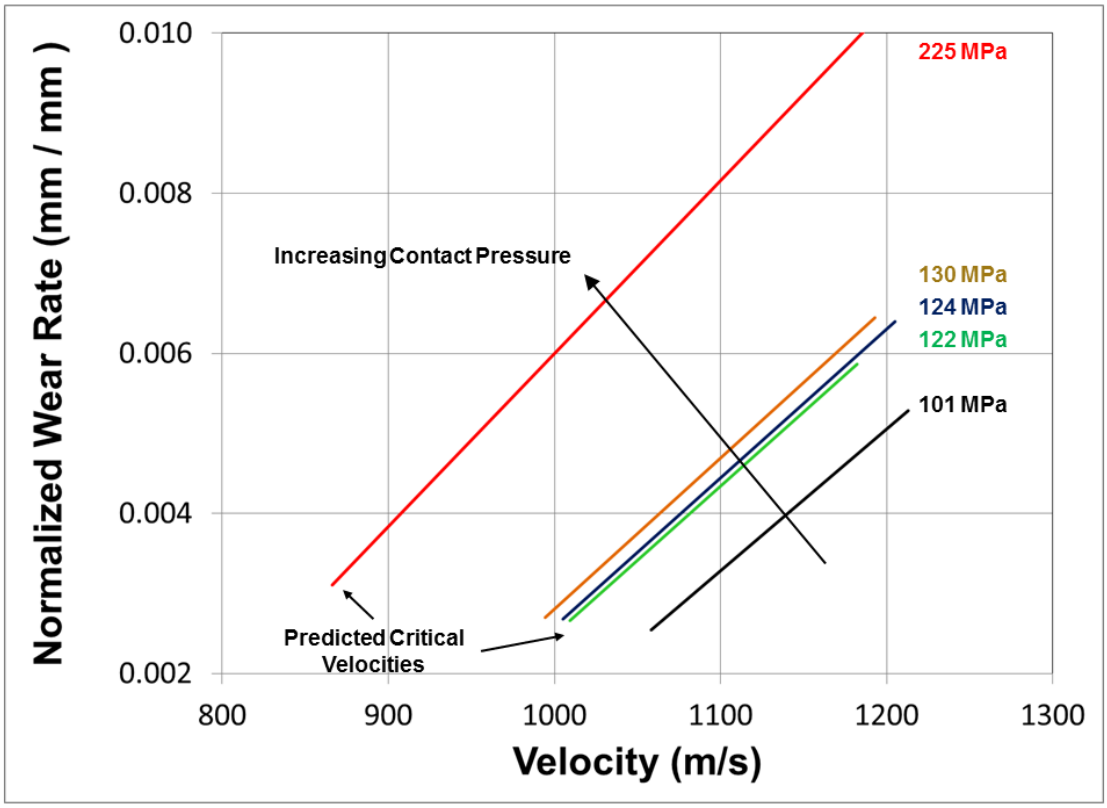

Figure 4.6 – Response of the normalized wear rate model.

MPa is shown in Figure 4.6. An error analysis is conducted to establish upper and lower bounds for a 95% confidence interval to evaluate the model results to experimental data. The associated error for each of the constants is presented in Table 4.10. The error in each of these individual constant values results in a propagated error that is used to define a 95% confidence interval in the form of an upper and lower bound. The propagated error is calculated using the following equation

$$\Delta\widetilde{W} = \sqrt{\Sigma_{i=1}^{n}\left(\frac{\delta\widetilde{W}}{\delta x_i}\Delta x_i\right)^2} \tag{4.13}$$

where $\Delta\widetilde{W}$ is the uncertainty in the normalized wear rate, Δx_i is the error or uncertainty in the constant value, and $\frac{\delta\widetilde{W}}{\delta x_i}$ is the partial derivative of the normalized wear rate model with respect to the constant δx_i. Applying the error propagation equation to the normalized wear rate model results in the following form

$$\Delta\widetilde{W} = \sqrt{\left[\sigma^{\frac{1}{4}} \cdot \left(v - \frac{A}{\sigma^{\frac{1}{4}}}\right) \cdot \Delta m\right]^2 + [-m \cdot \Delta A]^2 + \left[\left(\frac{\sigma}{\sigma_o}\right)^{\frac{1}{4}} \cdot \Delta\widetilde{W}_{c,o}\right]^2} \tag{4.14}$$

A plot comparing the experimental data to the normalized wear rate model using mean constant values with a 95% confidence interval for a contact pressure of 130 MPa is shown in Figure 4.7. The plots for each test are presented in Appendix B. All of the experimental data sets fall within the 95% confidence bands. The two experimental data sets that show the largest difference to the model predictions are the 101 MPa and 225 MPa tests. In general the uncertainty of the normalized wear rate measurements due to the variability in the slider deposition is the primary contributor to these differences.

The empirically derived normalized wear rate model provides a design tool for predicting volumetric wear in the melt lubrication region for a tribomaterial pairing of 6061-T6 aluminum on C110-H2 copper for sliding speeds ≤ 1,200 m/s and contact pressure between 100 – 225 MPa. Additional considerations, such as guider material properties are investigated in Chapter 5. The results from Chapter 5 can be used to further extend the normalized wear rate model for different guider materials**.** While the

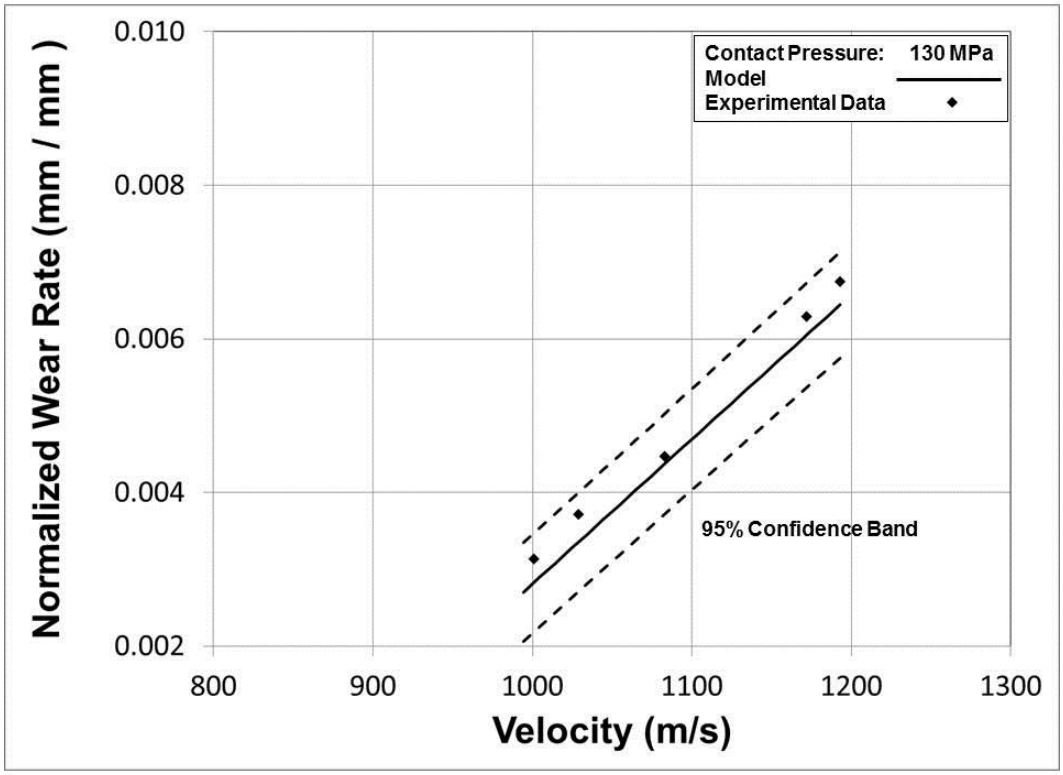

Figure 4.7 - A comparison plot for a 130 MPa set of experimental data to the model prediction including a 95% confidence interval band.

normalized wear rate model is only applicable to a 6061-T6 aluminum slider, it is important to note that the model can be used to gain insight into the behavior of different slider materials through the thermal constant, Γ. Future testing of slider materials with different thermal constants would be of interest to understand the effects on the melt lubrication proportionality constant, the heat dissipation rate, and the critical normalized wear rate constant.

4.3.4 Analysis: Geometry Effects

In the preceding two sections the effects of pressure and velocity on normalized wear rates for a 6061-T6 slider on a C110-H2 guider are discussed. Two tests were conducted

under similar contact pressures, 122 MPa and 124 MPa, but differing nominal contact areas, 5.8 mm^2 and 10.1 mm^2, respectively, as to better understand the effects of nominal contact area on normalized wear rates. The test conditions for these two tests are summarized in Table 4.11.

Table 4.11 - Summary of test conditions to study the effects of slider nominal contact area on wear.

Test No.	Slider Material	Guider Material	Contact Pressure (MPa)	Peak Velocity (m/s)	Nominal Contact Area (mm^2)
2	6061-T6	C110-H2	122	1180	5.8
3	6061-T6	C110-H2	124	1210	10.1

A comparison of the two tests is shown in Figure 4.8. Similar to the previous test results the critical velocity at which the wear shifts from severe plastic deformation to melt lubrication is sensitive to the contact pressure and follows the trend that the higher the contact pressure, the lower the critical velocity. This trend is consistent with previous test results and the data is ordered appropriately as the higher contact pressure test, 124 MPa, has a lower critical velocity than the 122 MPa test. Additionally, the critical velocities, slopes, and initial normalized wear rate of the two tests are relatively similar as the pressure differences are small (<2%).

A comparison of the two tests in terms of $\sigma^{1/4}v$ is made in Figure 4.9. Both the lines "collapse" on top of each other, indicating a good correlation. The effect of nominal contact area appears to be negligible as the two lines fall within the normalized wear rate error of ± 5 – 10%. These results indicate that the volumetric wear is proportional to the

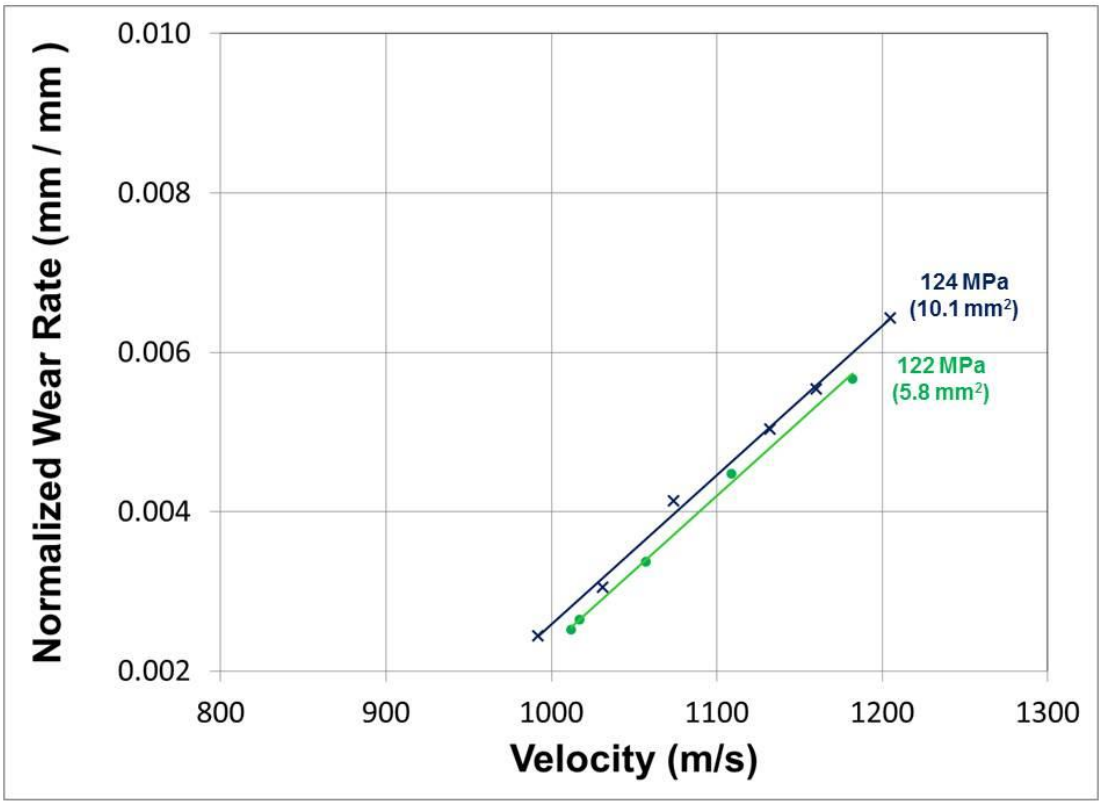

Figure 4.8 - Normalized wear rates comparing tests with similar contact pressures and different nominal contact areas.

nominal area of contact which is appropriate as the melt lubrication region is representative of large scale melting. This differs from traditional normalized wear rates or wear coefficients, which at low speeds are proportional to the real area of contact as determined by the normal contact load and strength / hardness of the softer material [14, 52, 53]. It can be concluded from Figures 4.8 and 4.9 that the effects of nominal contact area are negligible for the geometries tested. However, a better test to investigate the effects of nominal contact area on normalized wear rates in the melt lubrication region would be to modify the length of the slider and aspect ratio as this directly influences the geometry constant G, as defined in Equation 4.6. The geometry factor is sensitive to the

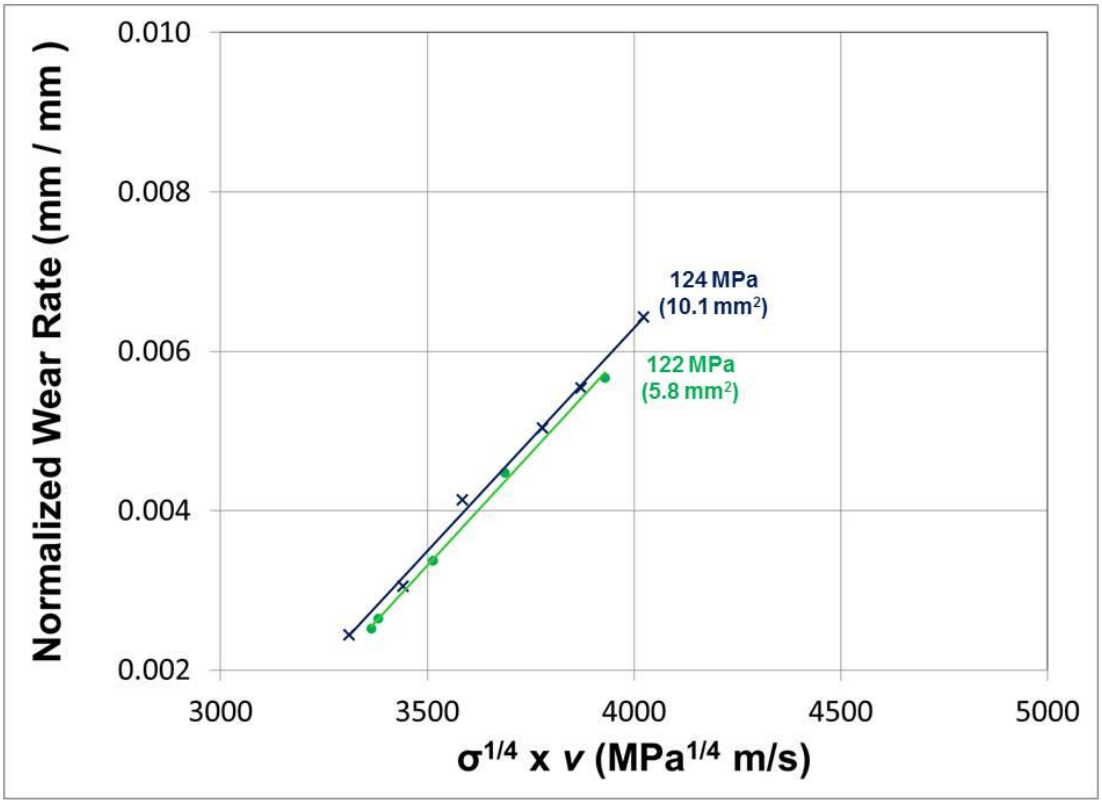

Figure 4.9 - Normalized wear rate dependence on $\sigma^{1/4}v$ for different nominal contact areas.

slider length and the aspect ratio such that a larger slider length and a larger aspect ratio results in a smaller geometry constant. The geometry constant is directly related to the melt lubrication proportionality constant, Ψ, and a larger slider length and aspect ratio would result in a smaller value of Ψ. It would be valuable in future testing to modify the slider length and aspect ratio to be vastly different as to exacerbate the differences. Currently for the 10.1 mm^2 and 5.8 mm^2 test cases with contact pressures of 124 MPa and 122 MPa the G values are 22.0 and 25.1 which relates to Ψ values of 5.62×10^{-6} and 5.60×10^{-6}. A better choice would have been to design the contact area to produce a G value of 10 as this would have lowered the Ψ value for the 124 MPa case from 5.62×10^{-6} to 2.55×10^{-6}.

CHAPTER 5: Experimental Results – Influence of Guider Material

5.1 Overview

A set of experiments was designed to investigate the effects of guider material properties on slider wear in the melt lubrication region. The concepts developed in the preceding chapters will be expanded on to include the effects of guider material properties. Three different guider materials were chosen. Peak sliding velocities between 1,050 and 1,250 were achieved. A contact pressure of 130 MPa was targeted for each test so that direct comparisons could be made among the three different guider materials. As a result of the variability in the EML system and the wedge fabrication process, the measured contact pressure varied from the targeted contact pressure up to 15 MPa between tests. However, these differences were removed by plotting the normalized wear rates as a function of $\sigma^{1/4}v$ so that a direct comparison among the three different tests could be made to draw conclusions on the effects of guider material properties on normalized wear rates

The objective of this study is to isolate the individual influence of mechanical properties (strength, hardness) and thermal properties (thermal conductivity, specific heat, and thermal diffusivity). To study the effects of guider mechanical properties on normalized wear rates, two materials with different mechanical properties, but similar thermal properties were first investigated. Then the effect of the guider thermal properties on normalized wear rates is studied. Using these results, the normalized wear rate model developed in Chapter 4 is further generalized with the addition of a guider material property term.

5.2 Experimental Results: Effect of Guider Mechanical Properties

5.2.1 Design of Experiments

A nominal contact pressure of 135 MPa was targeted with sliding velocities ranging from 0 – 1,200 m/s for a 6061-T6 aluminum slider to properly explore the effects of guider mechanical properties on slider wear. The mechanical property of interest in this study is hardness as it can be easily acquired through a bench top / hand held hardness tester in a laboratory environment.

For this set of experiments the softer material is the slider and it is assumed that the slider deforms plastically to establish a real area of contact at lower velocities. At higher velocities the slider undergoes large scale plastic deformation due to thermal softening until the heat dissipation rate is significant enough to incur large scale melting. Large scale melting is representative of melt lubrication as the melting of the slider is capable of supporting the normal contact load and fully separating the slider – guider surfaces. For these reasons it is expected that two guider materials with differing hardness values and similar thermal properties will have minimal impact on the normalized wear rates in both the severe plastic deformation and melt lubrication regions.

A broad survey of metals with a large hardness range, but similar thermal properties was conducted. Using CES EduPack, [5] two plots were generated comparing hardness to thermal conductivity and volumetric thermal mass ($\rho \cdot c$), as these are the thermal material properties of interest and will be discussed in more detail in the Section 5.3.1. From this survey a group of low – medium plain carbon steels were identified as the ideal candidate materials to investigate the effects of hardness on normalized wear rates in the melt lubrication region. Plain carbon steels are ideal as the primary constituent is iron

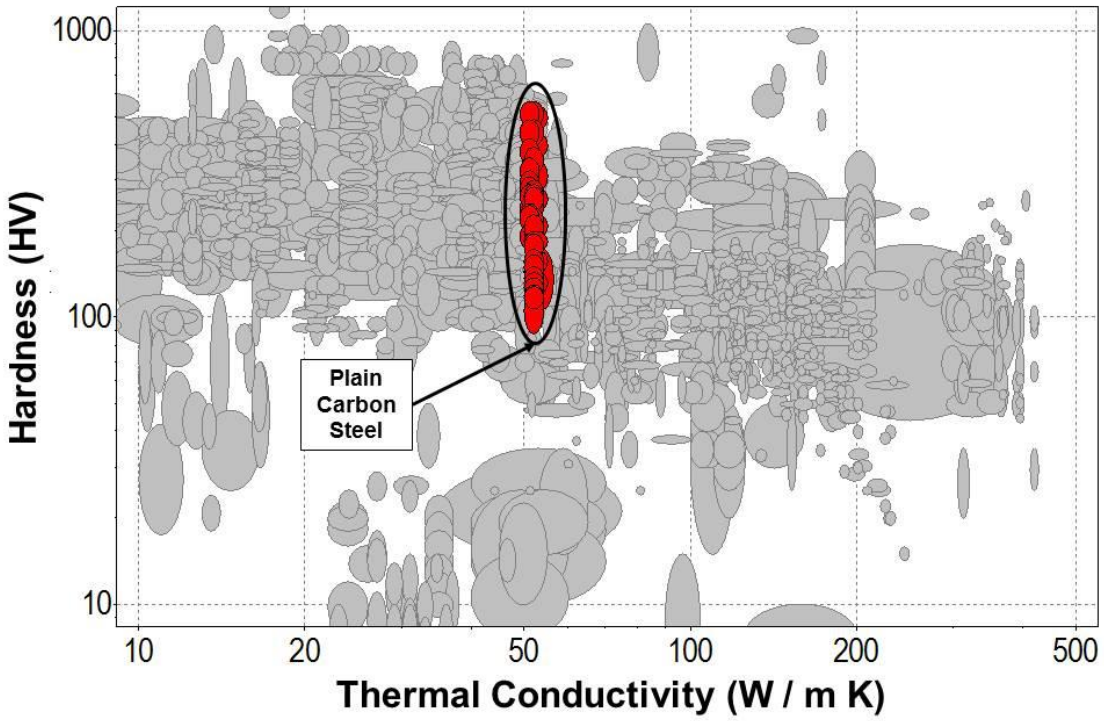

Figure 5.1 - Hardness versus thermal conductivity of low – medium plain carbon steels highlighted in red, generated by CES EduPack 2014 [5].

and small changes in carbon content can produce vastly different mechanical properties [68]. The carbon content in low – medium plain carbon steels is ≤ 0.50%, which means that the effects of varying carbon content will have minimal impact on the bulk thermal properties. An additional alloying element of manganese is also present, but in low amounts (0.6 – 0.9%), making iron the primary constituent and maintaining that the bulk thermal properties are driven by that of iron. Two plots of hardness versus thermal conductivity and hardness versus volumetric thermal mass are made in Figure 5.1 and 5.2, respectively. These plots show the large range of mechanical properties that low –

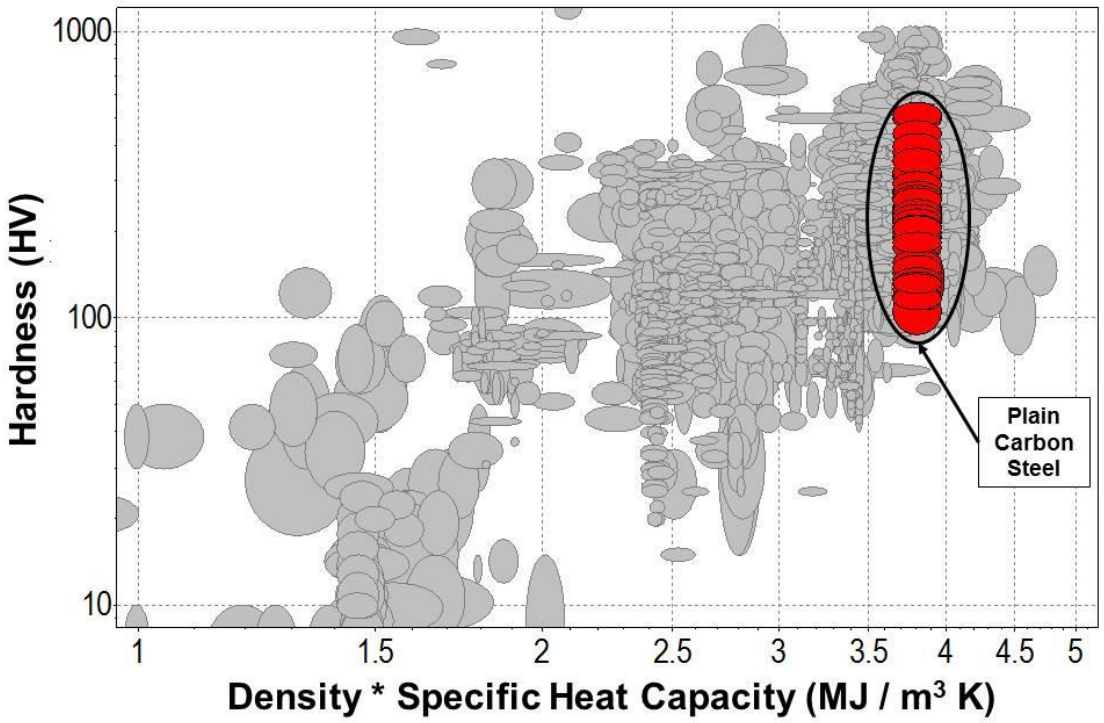

Figure 5.2 - Hardness versus volumetric thermal mass of low – medium plain carbon steels highlighted in red, generated by CES EduPack 2014 [5].

medium plain carbon steels provide, while maintaining similar thermal properties, making them an ideal group of materials to evaluate the effects of guider mechanical properties on normalized wear rates in the melt lubrication region.

Two different plain carbon steels were selected. One of the major challenges during the final selection of materials is related to the guider form. For testing purposes as outlined in Chapter 2, the guiders need to be 6.35 mm x 6.35 mm x 1560 mm or 1.56 m in length. For this reason a 1018 low plain carbon steel and a 1045 medium plain carbon steel were selected as they are readily available in the correct form. Hardness values, surface roughness measurements, and material compositions are provided in Table 5.1 [5,

9, 68]. Hardness measurements were taken using a portable Riehle hardness tester. The resultant hardness of the 1018 and 1045 plain carbon steels is 238 HV and 281 HV, respectively, which differs by approximately 15%.

Table 5.1 - Comparison of steel guider materials tested.

Test No.	Guider Material	Alloying Element Composition (%wt)				Ra (μm)	Hardness (HV)
		C	Mn	P (max)	S (max)		
6	1018 Steel	0.15 – 0.2	0.6 – 0.9	0.04	0.05	4.7	238
7	1045 Steel	0.43 – 0.5	0.6 – 0.9	0.04	0.05	4.3	281

5.2.2 Experimental Results

A comparison of the test results from the guider mechanical property study is shown in Figure 5.3. A nominal contact pressure of 134 MPa and 135 MPa were achieved for the 1018 and 1045 steel guider tests. A comparison of the two tests in terms of $\sigma^{1/4}v$ is made in Figure 5.4.The test results of both plots indicate that the guider mechanical properties in the melt lubrication region have a negligible effect, as both lines have similar slopes and lie on top of each other. One difference among the two tests is the critical velocity, v_c, and the heat dissipation constant, A ($\sigma^{1/4}v_c$) as a small but noticeable difference occurred. The critical velocity and the heat dissipation constant for the 1045 steel is 1.7% higher than the 1018 steel guider test. The transition from the severe plastic deformation to melt lubrication was difficult to capture experimentally. This required that the critical velocity was estimated using the intersection of the linear fit of the

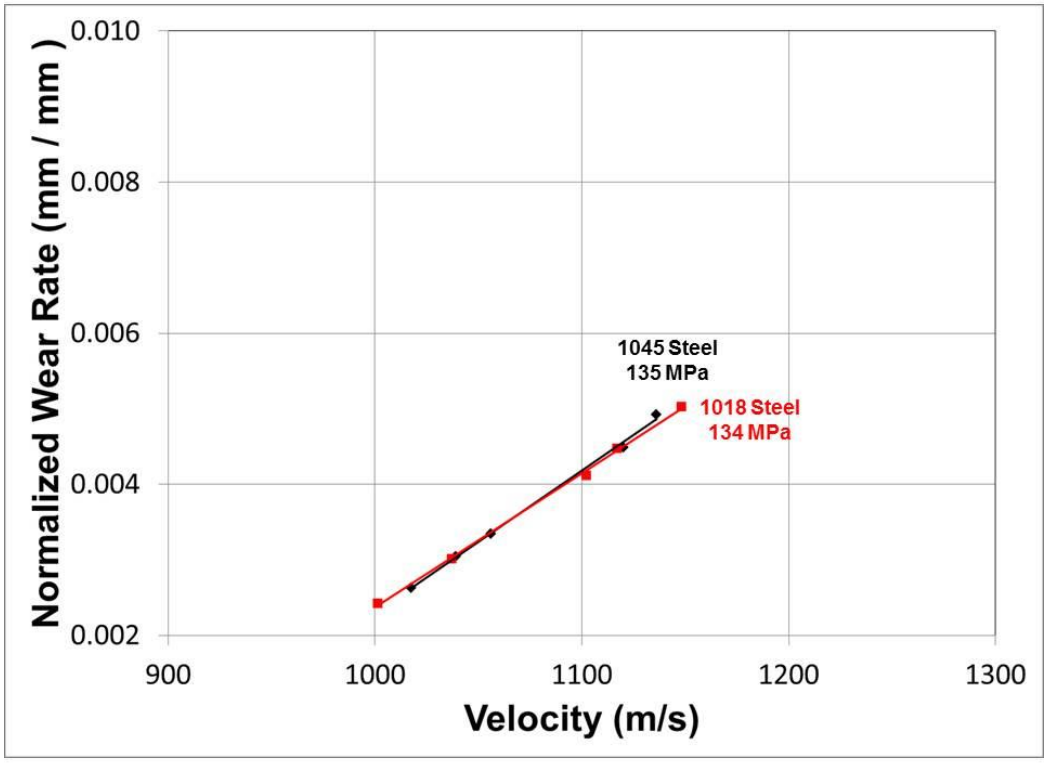

Figure 5.3 - Normalized wear rates for a 6061-T6 slider on a 1018 steel and 1045 steel guider in the melt lubrication region.

experimental data in the severe plastic deformation and melt lubrication regions. The differences between the critical velocities can be attributed to variability in the linear fit of each wear region as they are sensitive to the number of data points used to create the fit and the uncertainty in each normalized wear rate measurement.

Based on the results in Figures 5.3 and 5.4 it is concluded that the effects of guider mechanical properties on slider normalized wear rates in the melt lubrication region are negligible. Surface roughness measurements pre-test and post-test were taken for both the 1018 and 1045 steel guiders, as shown in Table 5.2. These measurements were taken at several different locations. Post-test measurements required removal of the slider deposition by the methods described in Chapter 2, so as to properly characterize the

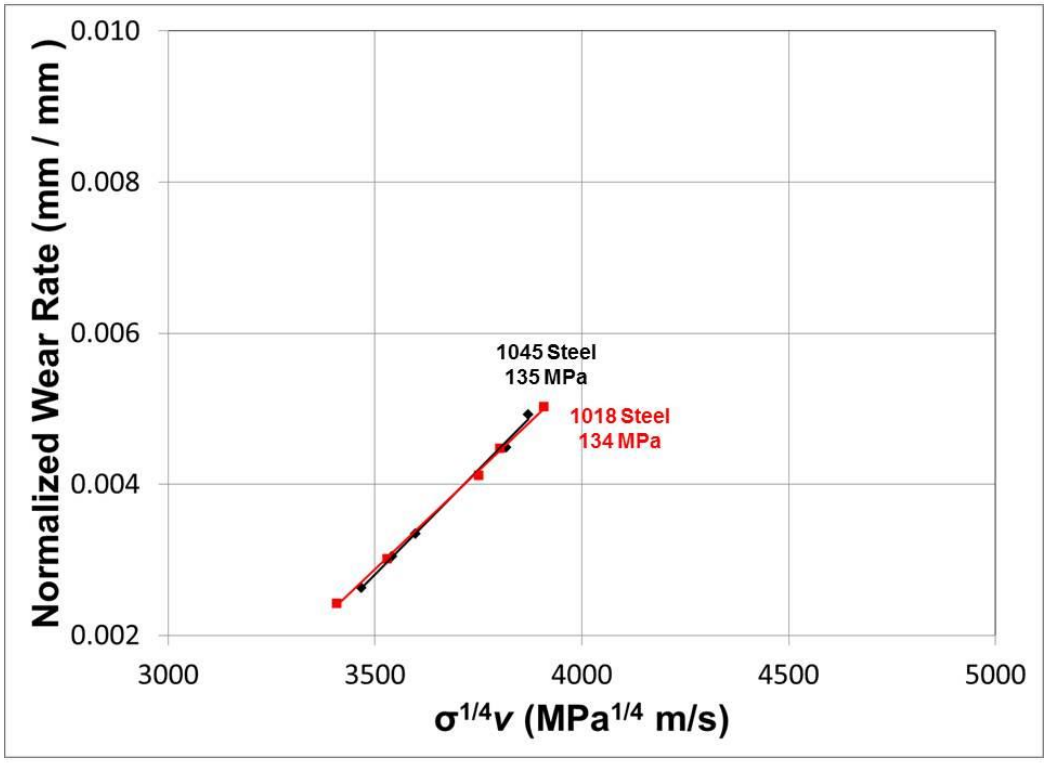

Figure 5.4 - Normalized wear rate dependence on $\sigma^{1/4}v$ for a 6061-T6 slider on a 1018 steel and 1045 steel guider in the melt lubrication region.

surface roughness in the slider-guider contact region. Test results showed good agreement with small differences in surface roughness indicating that no significant bulk deformation at the slider-guider interface occurred. These small differences in surface roughness are most likely representative of the variability in the guider material processing method.

A test with a much lower hardness or ultimate tensile strength may provide more information regarding the effects of mechanical properties on normalized wear rates as the ultimate tensile strength of cold drawn 1018 and 1045 steel at room temperature is approximately 420 MPa and 590 MPa, respectively [9]. These values are significantly larger than the 310 MPa ultimate tensile strength of the 6061-T6 aluminum slider at room

Table 5.2 - Comparison of pre-test and post-test surface roughness of the 1018 and 1045 steel guiders tests.

Test No.	Guider Material	Hardness (HV)	Ra (μm)	
			Pre-Test	Post-Test
6	1018 Steel	238	4.7	4.9
7	1045 Steel	281	4.3	4.0

temperature. In traditional wear theory the wear rate is proportional to the normal contact load and material hardness of the softer material or the material being worn, assuming the softer material is undergoing localized plastic deformation. For this reason a significantly harder guider material would be ideal at lower velocities. However, at higher velocities such as in the severe plastic deformation wear region, the slider has undergone thermal softening due to a rise in bulk temperature and accordingly the ultimate tensile strength is reduced as the interface temperature approaches the melting point of the 6061-T6 aluminum. Once the type of wear has shifted to the melt lubrication region the slider and guider surfaces are fully separated due to a melt lubrication film. For this reason guider hardness or ultimate tensile strength is less important at these higher velocities due to the nature of the sliding conditions.

5.3 Experimental Results: Effects of Guider Thermal Properties

5.3.1 Design of Experiments

A design of experiments to study the effects of guider thermal properties on normalized wear rates of a 6061-T6 aluminum slider is explored. A nominal contact

pressure was targeted to make relative comparisons among the different tribomaterial pairings. As discussed previously the variability in the EML system and the wedge fabrication process provides difficulties in replicating nominal contact pressures from test to test. However, utilizing the melt lubrication concepts developed in Chapter 4, the pressure effects are removed by plotting normalized wear rate as a function of $\sigma^{1/4}v$. Additionally it was shown in Section 5.2.2 that guider mechanical properties in the severe plastic deformation and melt lubrication regions have a negligible effect on normalized wear rates and no further correction is required. For these reasons a direct comparison can be made to better understand the effects of guider thermal properties on normalized wear rates in the melt lubrication region.

For this study the objective is to understand the influence of guider thermal properties on slider normalized wear rates. In order to properly capture this design space an upper and lower bound of relevant guider thermal properties must be defined. This is accomplished through the use of well-established heat transfer theory for sliding contacts. Additionally, an intermediate guider material that falls within the upper and lower bounds is desired to better understand the sensitivity of normalized wear rates to guider thermal properties.

For sliding contacts where the primary heat source is frictional dissipation and the mode of heat transfer is thermal conduction, two well-established theories (Jaeger and Blok) are used [69, 70]. These conditions differ from those of melt lubrication, as the heat source in melt lubrication region is viscous dissipation and the formation of a molten aluminum film would suggest the primary mode of heat transfer to be convection. However, limited published literature is available under the high sliding speeds and high

contact pressures examined in this dissertation. For this reason the traditional heat transfer theory is utilized as to provide insight for selecting guider materials with thermal properties of significance.

Heat transfer between two sliding solid bodies is presented in the form of a heat flux, q, and a heat partition coefficient, α, as shown in Figure 5.5. The heat flux represents the heat generated from the interaction of the sliding surfaces and the heat partition coefficient represents the portion of the heat flux that is partitioned into the guider. A maximum value of one indicates that all of the heat flux is partitioned into the guider and a minimum value of zero represents the opposite, where all of the heat flux is partitioned

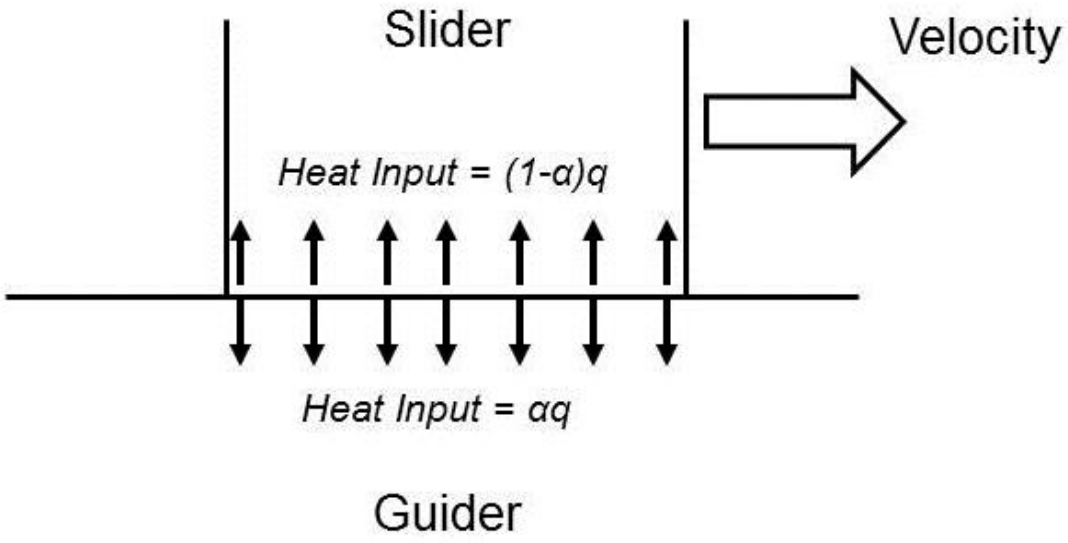

Figure 5.5 - Diagram of the heat partition theory concept.

into the slider. The fundamentals of heat partition theory lie in the assumption of temperature continuity or matching of the slider-guider surfaces. Jaeger's heat partition theory uses an average temperature matching, while Blok uses a maximum temperature matching approach. More recently, Bansal [71] matched localized temperatures at the slider-guider interface to form localized heat partition coefficients and showed a good correlation to that of Jaeger and Blok under the conditions investigated. For this materials selection exercise the two simple cases presented by Jaeger and Blok are analyzed as they are in a rather simplistic form for design purposes.

Heat partition theory for average temperature matching, referred to as Jaeger's theory, is presented in the following analytical form

$$\alpha = \frac{K_1 (v \cdot l)^{\frac{1}{2}}}{1.125 K_2 \chi_1^{\frac{1}{2}} + K_1 (v \cdot l)^{\frac{1}{2}}} \tag{5.1}$$

Heat partition theory for maximum temperature matching, referred to as Blok's theory, is defined as

$$\alpha = \frac{0.5 \cdot \left(1 - \frac{1}{\sqrt{2}}\right) + \frac{K_1}{K_2} \cdot \sqrt{\frac{\pi}{2} \cdot \frac{v \cdot l}{4 \cdot \chi_1}}}{1 + \frac{K_1}{K_2} \cdot \sqrt{\frac{\pi}{2} \cdot \frac{v \cdot l}{4 \cdot \chi_1}}} \tag{5.2}$$

where α is the heat partition coefficient for the guider, K_1 is the thermal conductivity of the guider, K_2 is the thermal conductivity of the slider, χ_1 is the thermal diffusivity of the guider, $2l$ is the length of the slider in the direction of travel, and v is the velocity.

Table 5.3 - Heat partition coefficient properties and values for a 6061-T6 aluminum slider on a C110-H2 guider.

Property	Value
$2l$, slider length (mm)	3.18
K_1, guider thermal conductivity (W / m – K)	388
c, guider specific heat (J/kg K)	385
ρ, guider density (kg / m^3)	8900
χ_1, guider thermal diffusivity (m^2 / s)	1.13E-04
K_2, slider thermal conductivity (W / m – K)	160

The two analytical forms in Equations 5.1 and 5.2 make simplifying assumptions based on the magnitude of the Peclet number and are applicable for large Peclet numbers. The Peclet number is a dimensionless heat transfer parameter that represents the ratio of advective to diffusive heat transport, meaning for small Peclet numbers, <0.1, thermal conduction dominates and for larger Peclet numbers, >10, convection dominates [72]. The Peclet number is defined as follows

$$Pe = \frac{v \cdot 2l}{\chi_1} \tag{5.3}$$

For a 6061-T6 aluminum slider on a C110-H2 guider, with a sliding speed of 1,000 m/s, a slider length ($2l$) of 0.00318 meters, and a guider thermal diffusivity of 1.13E-04 m^2/s, a Peclet number of 28,000 is calculated. This value is three orders of magnitude larger than the value of 10 used to define large Peclet numbers, in traditional heat partition theory. For large sliding velocities and thus large Peclet numbers the limits of the heat partition coefficients, defined in Equations 5.1 and 5.2, approach a value of one, meaning that approximately all of the heat generated at the slider-guider interface is partitioned into the guider. A comparison of the two heat partition theories as a function of slider velocity is made in Figure 5.6 for a 6061-T6 aluminum slider on a C110-H2 guider using the conditions as summarized in Table 5.3 [5, 9].

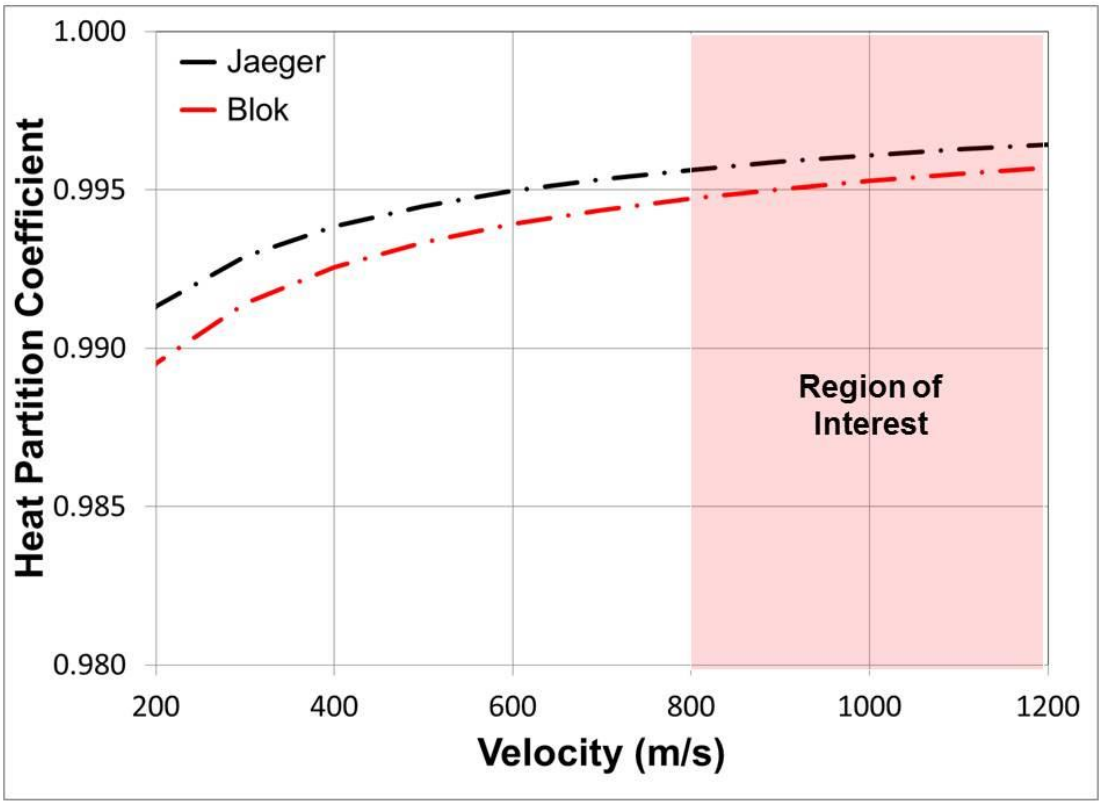

Figure 5.6 - Heat partition coefficient for sliding contacts with large Peclet numbers computed using two different theories.

The results shown in Figure 5.6 suggest that for the melt lubrication velocity range (800 – 1,200 m/s) that the majority of the heat flux generated at the slider-guider interface is partitioned into the guider and only a small fraction is partitioned into the slider. Additionally, the difference between Jaeger and Blok's heat partition theory is small <0.1%. For this reason Jaeger's heat partition theory is used for the identification and selection of guider materials as the analytical form is more simplistic than Blok's theory.

Several simplifications are made to Equation 5.1 in order to put it into a form that can be used for screening potential guider materials. The first simplification requires fixing the slider length and velocity. For this study the slider geometry is fixed and the effects of velocity in the severe plastic deformation and melt lubrication regions have minimal impact on the heat partition coefficient, in which case Equation 5.1 can be simplified to the following form

$$\alpha = \frac{K_1 C_1}{1.125 K_2 \chi_1^{\frac{1}{2}} + K_1 C_1} \tag{5.4}$$

where C_1 represents $(v \cdot l)^{1/2}$. The second simplification requires fixing the slider thermal conductivity K_2. A slider material of 6061-T6 aluminum is used for all experiments. This allows for Equation 5.4 to be simplified further to the form

$$\alpha = \frac{K_1 C_1}{C_2 \chi_1^{\frac{1}{2}} + K_1 C_1} \tag{5.5}$$

where C_2 represents ($1.125 \cdot K_2$). Dividing the numerator and denominator by K_1 gives the following form

$$\alpha = \frac{C_1}{C_2 \frac{\chi_1^{\frac{1}{2}}}{K_1} + C_1} \tag{5.6}$$

Simplifying the thermal diffusivity χ_1 term provides

$$\alpha = \frac{C_1}{C_2 \left(\frac{1}{\rho_1 \cdot c_1 \cdot K_1}\right)^{\frac{1}{2}} + C_1} \tag{5.6}$$

This provides a material index in the form

$$M_1 = \rho_1 \cdot c_1 \cdot K_1 \tag{5.6}$$

where ρ, is the density, c, is the specific heat, and K is the thermal conductivity of the guider material.

Maximization of the material index M_1 results in a larger heat partition coefficient and minimization of the material index M_1 results in a smaller heat partition coefficient. Additionally, it is of interest to find an intermediary heat partition value for the guider thermal property study. A group of common materials available for purchase utilizing the material index M_1 is evaluated with results shown in Table 5.4. A maximum material

index value of 13.3 x 10^8 is identified for copper. This means using a copper guider results in a larger heat partition coefficient and provides the upper bound for the guider thermal study. A minimum material index value of 0.4 x 10^8 is identified for titanium. The use of titanium results in a lower heat partition coefficient and provides the lower bound. A good intermediate material index of approximately 4.0 x 10^8 is identified for molybdenum and tungsten. However, acquisition of molybdenum and tungsten proved costly. Several other potential material candidates were unavailable in the proper form and for this reason an intermediate material of plain carbon steel was selected. The selection of a plain carbon steel serves a dual purpose as it was used in the guider mechanical property study as well.

Table 5.4 - Potential materials for the guider thermal property study.

Material	ρ (kg/m^3)	c (J/kg-K)	K (W /m-K)	M_1 (J^2 / m^4-K-s) x 10^8
Iron	7600	465	43	1.5
Low - Plain Carbon Steel	7850	485	52	2.0
Medium - Plain Carbon Steel	7870	486	52	2.0
High - Plain Carbon Steel	7850	490	50	1.9
Stainless Steel	7970	510	16	0.7
Copper	8890	385	388	13.3
Brass	8270	377	122	3.8
Bronze	8710	384	75	2.5
Aluminum	2700	896	160	3.9
Nickel	8900	456	70	2.8
Titanium	4510	540	17	0.4
Molybdenum	10220	276	142	4.0
Tungsten	19300	138	155	4.1
Zinc	7140	392	105	2.9

The three materials selected were C110-H2 copper, 1018 / 1045 steel, and titanium grade 2 commercial purity. All three of these materials are in a high purity form. A plot of the heat partition coefficients as a function of sliding velocity for the three materials copper, plain carbon steel, and titanium is shown in Figure 5.7. It is important to note that copper and titanium provide the upper and lower bounds, while steel falls in between as the intermediate material as predicted by the material index M_1.

A summary of the tribomaterial pairings, contact pressures, peak velocities and nominal contact areas used to investigate the effects of guider thermal properties on normalized wear rates is summarized in Table 5.5. Overlap between the pressure-velocity

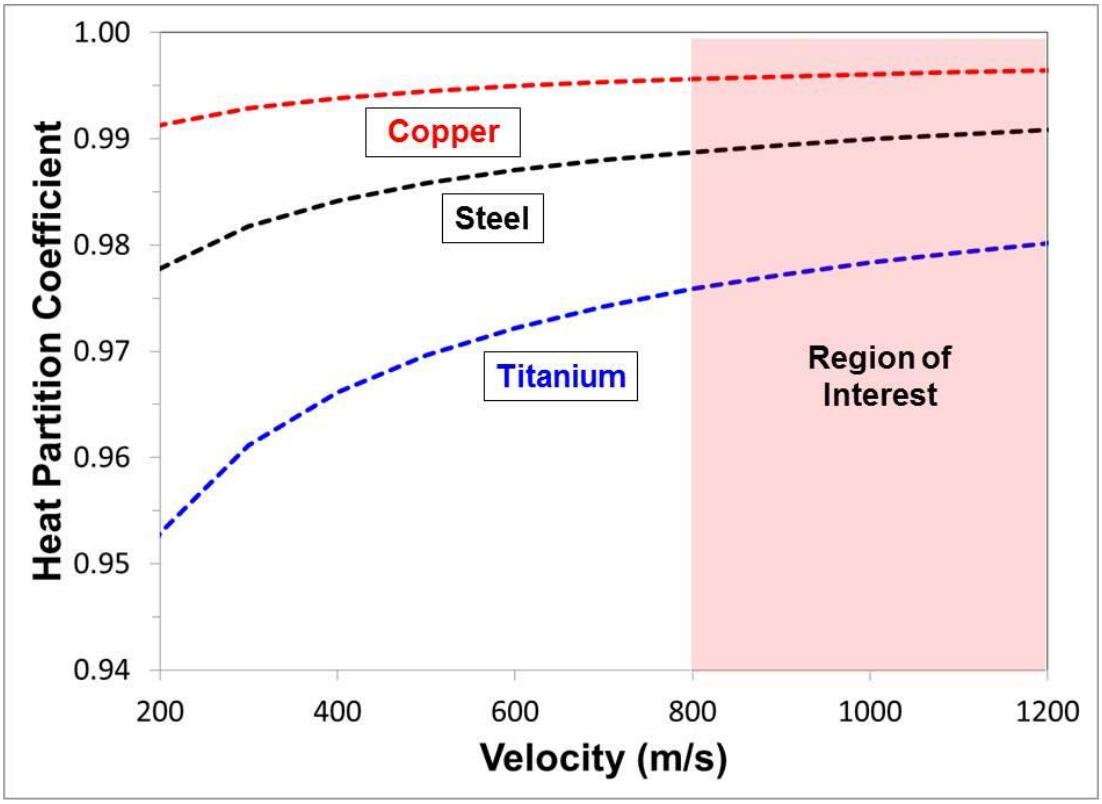

Figure 5.7 - A comparison plot of the heat partition coefficients for the three selected materials for the guider thermal properties study.

experiments discussed in Chapter 4, and the guider mechanical study in Section 5.2 require that only a single test of 6061-T6 aluminum slider on a titanium grade 2 commercial purity guider is required. These results are summarized and discussed in Section 5.3.2.

Table 5.5 - Tribomaterial pairings and test conditions used in the guider thermal study.

Test No.	Slider Material	Guider Material	Contact Pressure (MPa)	Peak Velocity (m/s)	Nominal Contact Area (mm^2)
1	6061-T6	C110-H2	101	1210	10.1
2	6061-T6	C110-H2	122	1180	5.8
3	6061-T6	C110-H2	124	1210	10.1
4	6061-T6	C110-H2	130	1190	10.1
5	6061-T6	C110-H2	225	1180	10.1
6	6061-T6	1045 Steel	135	1140	10.1
7	6061-T6	1018 Steel	134	1150	10.1
8	6061-T6	Titanium G2 CP	144	1170	10.1

5.3.2 Experimental Results

A comparison of the test results from the guider thermal property study is shown in Figure 5.8. The data from the five tests of copper at different contact pressures is represented by the red triangles. The two steel tests are represented by the black diamonds and the single titanium test is represented by the blue squares. Each data set is fit to a linear function. A comparison of the eight experiments in terms of $\sigma^{1/4}v$ is made in Figure 5.9. As discussed previously the mechanical effects are negligible in the severe plastic deformation and melt lubrication regions, consequently isolating the guider thermal properties. A distinct reordering of the guider materials is apparent. The

predicted ordering of the three guider materials, using material index, $M_1 = \rho \cdot c \cdot K$, from Section 5.3.1, is titanium, steel, and copper. As titanium has the least favorable thermal properties of the three materials tested, meaning that of the heat generated at the contact interface a lesser portion of the heat is partitioned into the guider and a greater portion is partitioned into the slider, creating the conditions necessary to develop a melt lubrication film at a lower critical velocity. Accordingly, the same reasoning is applied to the steel and copper guider tests. However, an ordering of titanium, copper, and steel in Figure 5.9 indicates the material index M_1 is not applicable under the sliding conditions in the severe plastic deformation and melt lubrication regions.

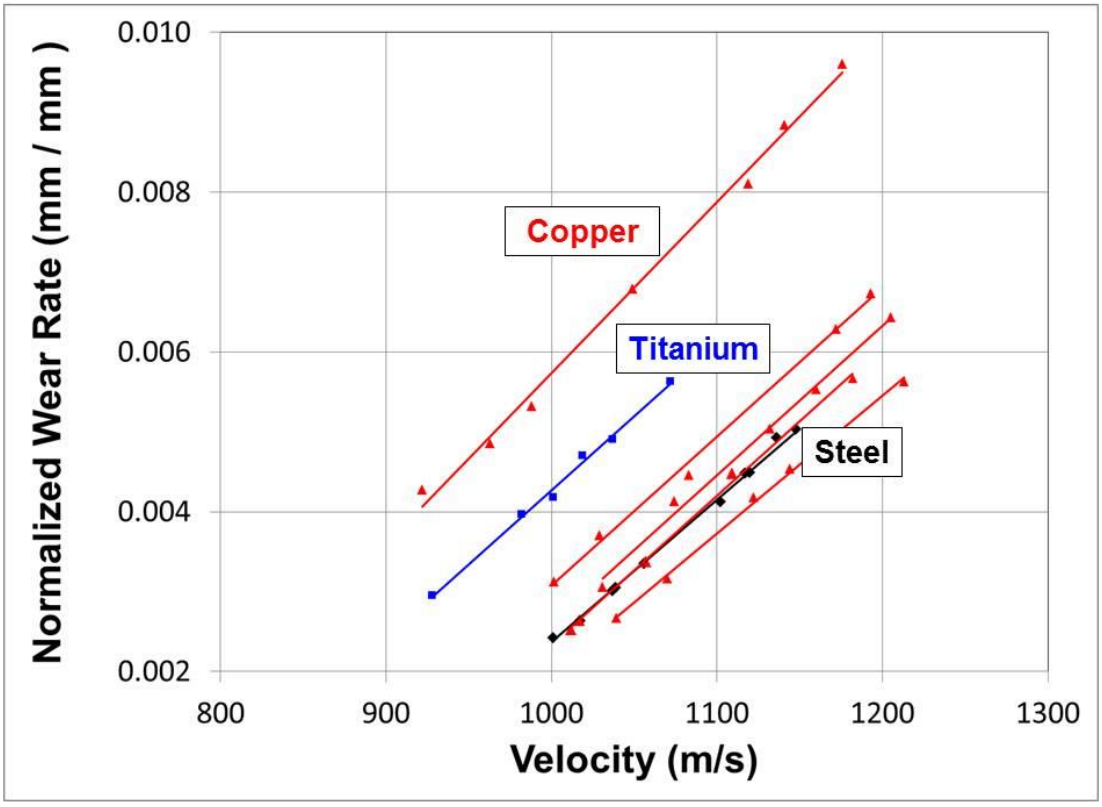

Figure 5.8 - Normalized wear rates as a function of velocity for three different guider materials in the melt lubrication region.

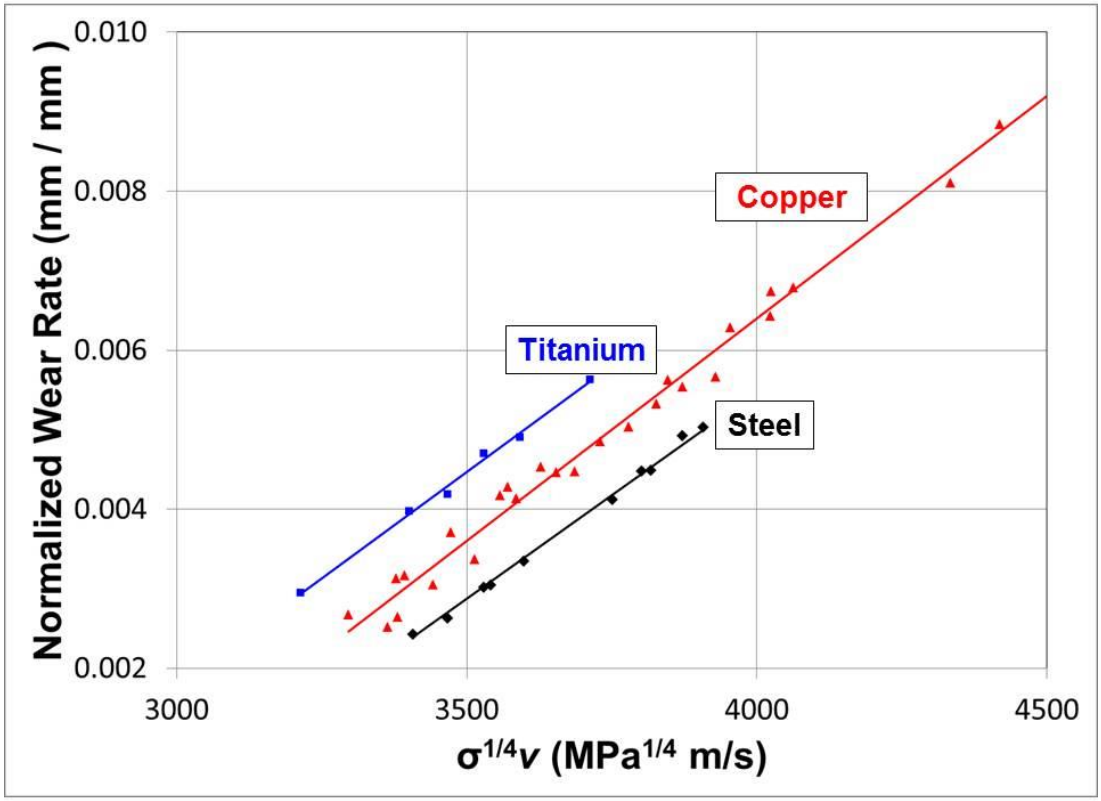

Figure 5.9 - Normalized wear rate dependence on $\sigma^{1/4}v$ for three different guider materials in the melt lubrication region.

Further insight can be gained by comparing the dwell time, which is the time that a point on the guider stays in contact with the sliding heat source, to the diffusion time, which is the time it takes for the heat to penetrate into the bulk material [73]. The dwell time is defined as

$$\tau_d = \frac{2l}{v} \tag{5.7}$$

where *2l*, is the slider length, and *v*, is the slider velocity. Furthermore, the diffusion time is defined as

$$\tau_h = \frac{z^2}{\chi} \tag{5.7}$$

where *z* is the diffusion depth, and χ, is the thermal diffusivity. The ratio of the diffusion time to the dwell time is as follows

$$\Phi = \frac{\tau_h}{\tau_d} = \frac{v \cdot z^2}{2l \cdot \chi} \tag{5.8}$$

Equation 5.8 is representative of the ratio of time required for heat to diffuse into the bulk material to the available dwell time of the heat source. A Φ value less than one indicates that a sufficient amount of time is available for bulk diffusion to occur resulting in steady state heat transfer conditions, whereas a ratio greater than one results in transient heat transfer conditions. For the values of $2l$ = 0.00318 meters, v = 1,000 m/s, χ = 1.13e-04 (thermal diffusivity of copper), and $z = l$ = 0.00159, a Φ value of 7,000 is calculated, indicating that the conditions are representative of transient heat transfer. For this reason a simple transient conduction problem in which a small volume of guider material at the surface experiences a sudden change in surface temperature is considered. This approach is similar to that of quenching a hot metal forging. The concept is depicted in Figure 5.10. Based on the large calculated Φ value, it's assumed that there is inadequate time for heat to diffuse into the bulk material, such that a small volume of material near the surface

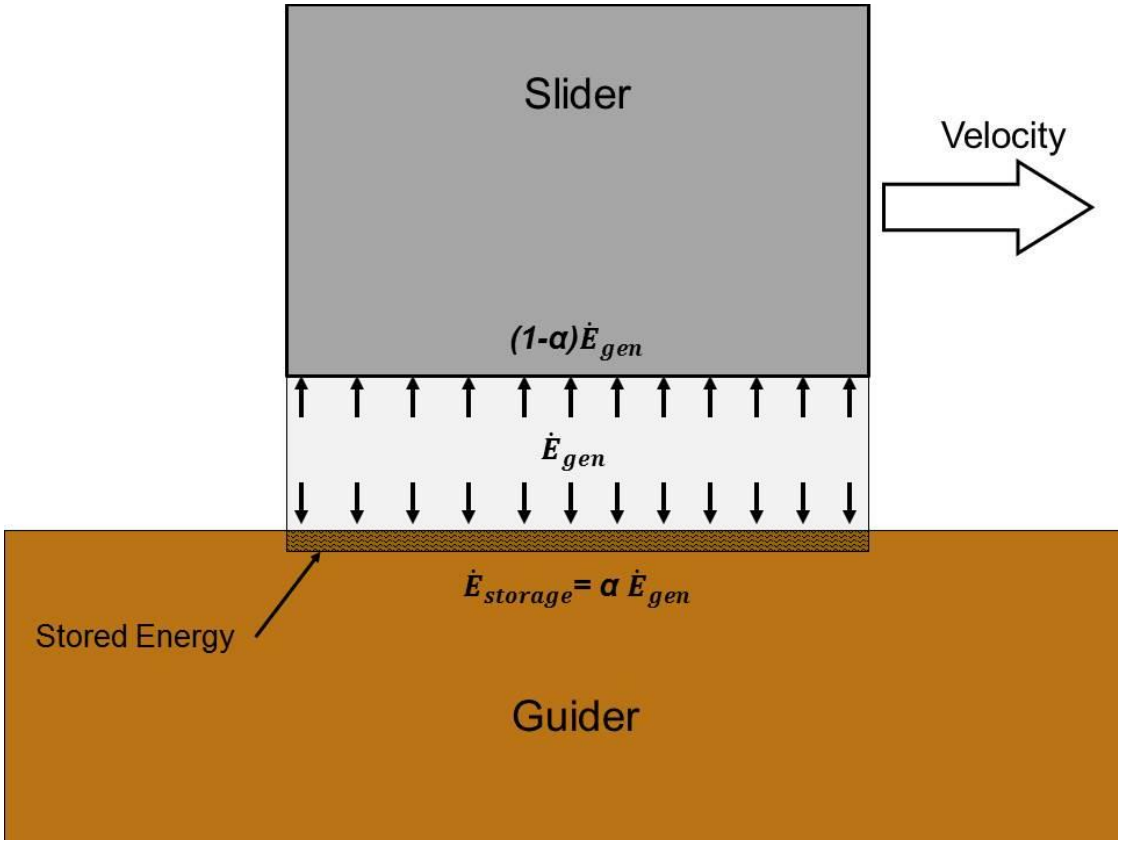

Figure 5.10 - Diagram of the lumped capacitance approach to analyzing the guider thermal properties.

acts as a heat sink. The temperature of this volume is spatially uniform and the temperature gradients within the volume are negligible. Utilizing this assumption a lumped capacitance approach is taken and an energy balance is performed [72].

$$\dot{E}_{storage} = \alpha \cdot \dot{E}_{gen} \tag{5.9}$$

where $\dot{E}_{gen}$, is rate of heat generated at the contact interface, α the portion of that heat partitioned into the guider, and $\dot{E}_{storage}$ is the energy storage rate of the volume of guider material near the surface. The rate of energy storage can be rewritten as

$$\dot{E}_{storage} = \rho \cdot c \cdot \bar{V} \cdot \frac{\Delta T}{\tau_d} \tag{5.10}$$

where ρ is the density, c is the specific heat, $\bar{V}$ is the volume of guider material, ΔT is the rise in temperature and τ_d is the guider dwell time. It is assumed that the volume is fixed in size and relatively thin.

The ratio of the energy storage rate to the total rate of energy dissipation $\dot{E}_{gen}$ is the definition for the heat partition coefficient and is represented in the following form

$$\alpha = \frac{\dot{E}_{storage}}{\dot{E}_{gen}} \tag{5.11}$$

Substituting in Equation 5.10 into 5.11 and rearranging the terms

$$\alpha = \rho \cdot c \cdot \frac{\bar{V} \cdot \Delta T}{\tau_d \cdot \dot{E}_{gen}} \tag{5.12}$$

Equation 5.12 can be used to better understand the effects of guider material properties on heat partitioning at the slider-guider interface. This provides a material index in the form

$$M_2 = \rho \cdot c \tag{5.13}$$

A material with a large value of M_2 or volumetric thermal mass ($\rho \cdot c$) will partition more heat into the guider than a lower one. Increasing the heat partitioned into the guider and consequently decreasing the heat partitioned into the slider, results in an increase in the critical velocity. Additionally, for the case with pressure effects removed this would mean that the heat dissipation rate constant ($\sigma^{1/4} \cdot v$) would also increase with increasing M_2.

The volumetric thermal mass values for the guider materials tested, C110-H2 copper, plain carbon steel (1018/1045), and titanium grade 2 commercial purity are provided in Table 5.6. The material properties for titanium grade 2 commercial purity are replaced by those of titanium dioxide as the bar was formed by a hot extrusion process and was cooled in open air [5]. This resulted in a thick slag or scale on the exterior of the bar that is representative of titanium dioxide. The experimental data was fit using the material properties for high purity titanium and titanium dioxide. The titanium dioxide provided a better fit and was used in this analysis. For the copper and steel guiders the natural oxide scale was relatively thin as the bars were cold drawn and for this reason the bulk properties of these materials are used.

Table 5.6 - Guider thermal properties.

Material	ρ (kg/m^3)	c (J/kg-K)	M_2 (MJ/kg-m^3)	β
Titanium Dioxide	4010	690	2.8	1.24
Copper	8890	385	3.4	1.00
Plain Carbon Steel	7850	485	3.8	0.90

A normalized volumetric thermal mass term β is introduced as

$$\beta = \frac{(\rho \cdot c)_{copper}}{(\rho \cdot c)_x} \tag{5.14}$$

The normalized volumetric mass term is incorporated into the pressure term of the normalized wear rate equation, Equation 4.10, as follows

$$\widetilde{W} = \Psi \cdot (\beta \cdot \sigma)^{\frac{1}{4}} \cdot v + b \tag{5.15}$$

Re-plotting of the normalized wear rate data for the eight experiments as a function of $(\beta \cdot \sigma)^{1/4} \cdot v$ collapses the data onto a single line as shown in Figure 5.11. The experimental data supports the use of volumetric thermal mass as the guider material metric when operating in the severe plastic deformation and melt lubrication regions. This suggests that the effects of thermal conductivity on the heat partition coefficient are secondary in

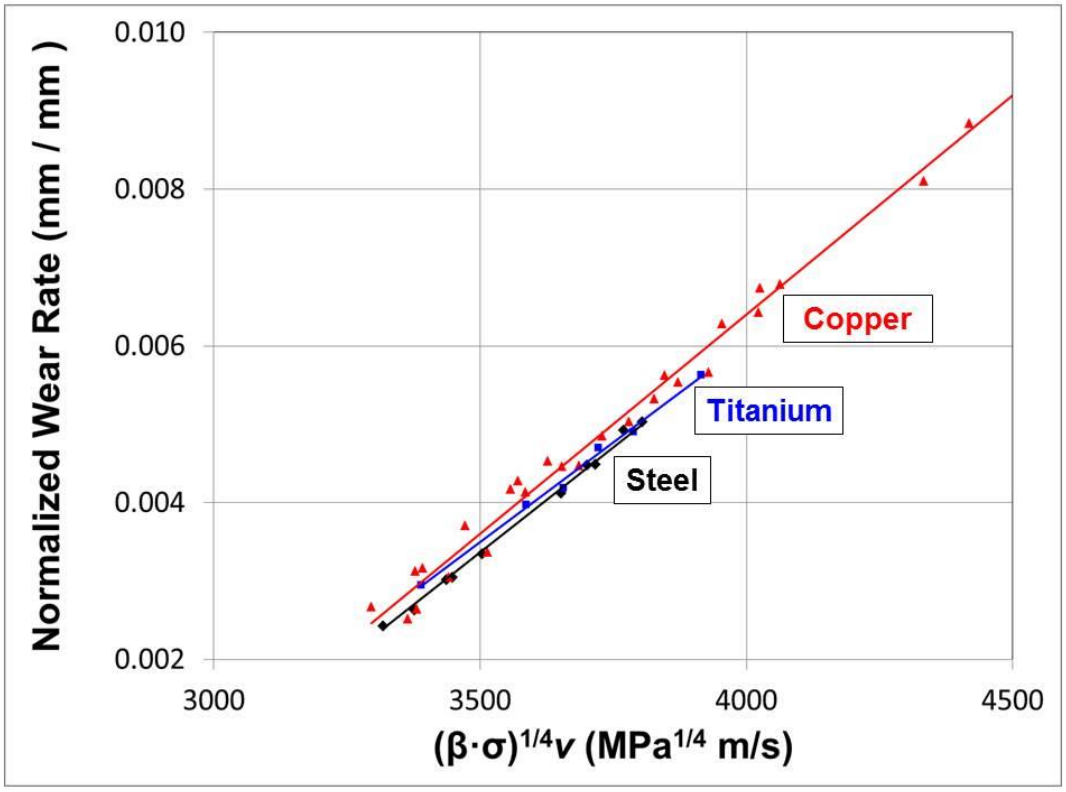

Figure 5.11 - Normalized wear rate dependence on $(\beta\cdot\sigma)^{1/4}v$ for three different guider materials in the melt lubrication region.

nature, as the exposure time is on the order of a microsecond, making heat diffusion negligible.

Utilizing the entire set of eight experiments the empirical model, Equation 4.17, developed in Chapter 4 is now updated to include guider thermal property effects as follows

$$\widetilde{W} = \Psi \cdot \left[(\beta \cdot \sigma)^{\frac{1}{4}} \cdot v - A\right] + B \cdot \left(\frac{\beta \cdot \sigma}{\sigma_o}\right)^{\frac{1}{4}} \tag{5.16}$$

The normalized wear rate equation, as presented in Equation 5.16, is in a general form and is capable of replicating normalized wear rates using the constants Ψ, A, B and σ_o and their values summarized in Table 5.7. The equation is applicable for velocities in the melt lubrication region ($v_c \leq v \leq 1{,}200$ m/s) and pressures in the range of 100 – 225 MPa for a 6061-T6 aluminum slider on different guider materials. The guider material correction factor, β, is calculated per Equation 5.14. The model is correlated to the experimental data as shown in Figure 5.12. Individual comparisons between the model and each set of data for the experiments with a 95% confidence band are available in Appendix B.

Table 5.7 - Normalized wear rate equation constants for all eight experiments.

Constant	Average Value	95% Confidence Interval
Ψ, melt lubrication proportionality constant (s / m $MPa^{1/4}$)	5.48E-06	0.38E-06
A, heat dissipation rate ($MPa^{1/4}$ m / s)	3,355	84
B, critical normalized wear rate	2.54E-03	0.42E-03
σ_o, reference contact pressure (MPa)	101	---

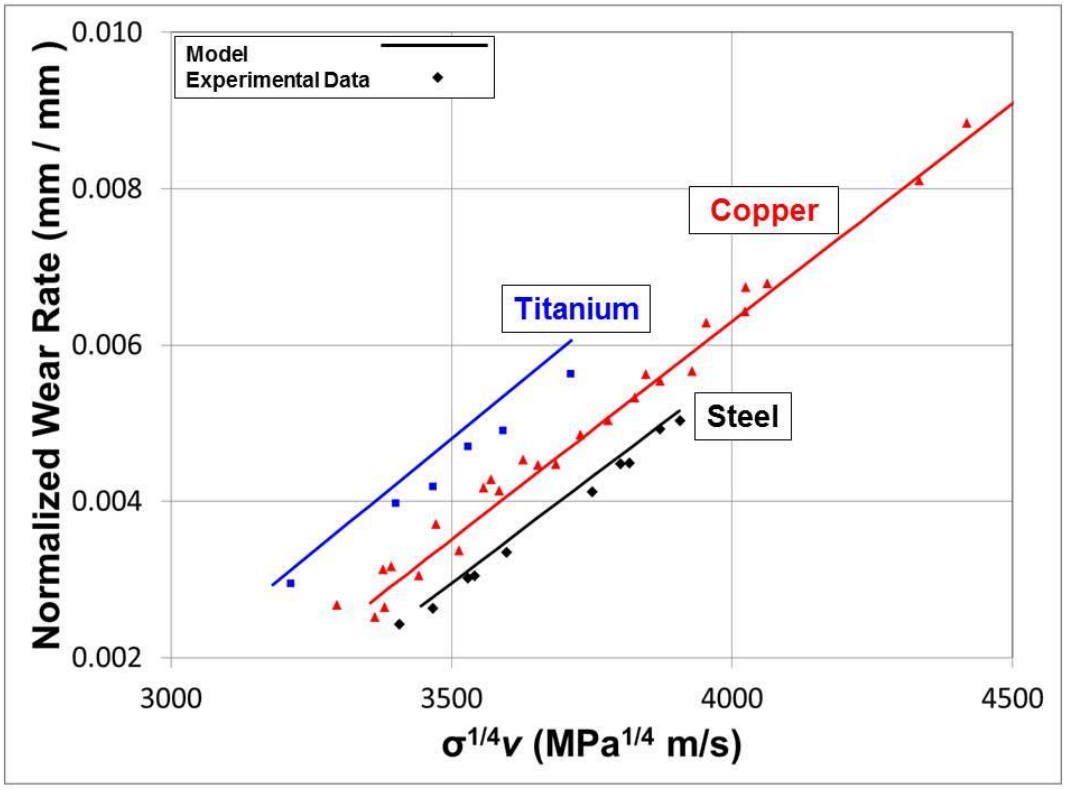

Figure 5.12 - Comparison of the normalized wear rate model (solid line) and experimental data in the melt lubrication region as a function of $\sigma^{1/4}v$.

CHAPTER 6: GUIDER MATERIAL SELECTION

6.1 Guider Material Properties Overview

The primary focus of the preceding chapters has been on the characterization of the material response of the slider in the form of wear at high sliding speeds and high contact pressures. It is important to recognize that slider wear is a system response, which is dependent on both the tribomaterial pairing and operating conditions. It has been shown that slider wear is predominately a function of the slider thermal properties, while guider thermal properties have a secondary effect [13].

For practical engineering applications the guider is often subjected to repetitive use, while the slider more often than not is designed for single use. An example is that of a projectile rotating band on a rifled barrel in large caliber cannons [74]. In these instances it is essential that the guider is durable for performance and economic viability. Under high sliding speeds and high contact pressures there are three primary guider degradation mechanisms to consider when selecting a suitable material. They include, but are not limited to gouging, wear and fracture. The remainder of the chapter will summarize the key material properties to consider when selecting a guider material, as they relate to slider wear and guider durability.

6.2 Guider Material Selection in the Melt Lubrication Region

There are several different wear regions that may be encountered by an accelerating slider. Normalized wear rates or wear coefficients are influenced by the sliding conditions and tribomaterial pairings. In most applications a low coefficient of friction and low normalized wear rate is ideal. For high sliding speeds at low contact pressures

the ideal operating regions are the plasticity dominated and melt wear regions as shown in Figure 6.1 [15]. It is important to note that the boundary lines for the seizure and severe plastic deformation regions are theoretical as empirical data for aluminum alloys was not available at the time of wear mechanism map publication. If the seizure boundary line was shifted to a normalized pressure of 10^0 and the adjacent wear regions were extrapolated, then three different types of wear: plasticity dominated, severe plastic deformation and melt wear would be expected at high sliding speeds and high contact pressures. Additionally as discussed in Chapter 3 a fourth wear region, melt lubrication, exists. For high sliding speeds and high contact pressures the slider may operate in the plasticity dominated, severe plastic deformation, and melt lubrication regions as identified in the present work. The ideal region under the present work is the plasticity dominated region ($\widetilde{W} = 0.1 - 1.0 \cdot 10^{-4}$), characterized by lower wear rates than the severe plastic deformation ($\widetilde{W} = 1.0 \cdot 10^{-3}$) and melt lubrication ($\widetilde{W} = 0.1 - 1.0 \cdot 10^{-2}$) regions. For this reason it is important to identify the conditions at which severe plastic deformation and melt lubrication occurs as to avoid operating in these two regions if possible.

The onset of the severe plastic deformation region is difficult to predict. However, a heat dissipation rate constant, as defined in Equation 4.11, can be used to predict the critical velocity at which the slider wear transitions from severe plastic deformation to melt lubrication. Based on the wear mechanism map in Figure 6.1, the severe plastic deformation region precedes the melt lubrication region and is bounded by a relatively small range of normalized velocities. For this reason the critical velocity is used to demarcate the low wear rate region (plasticity dominated wear) from the high wear rate

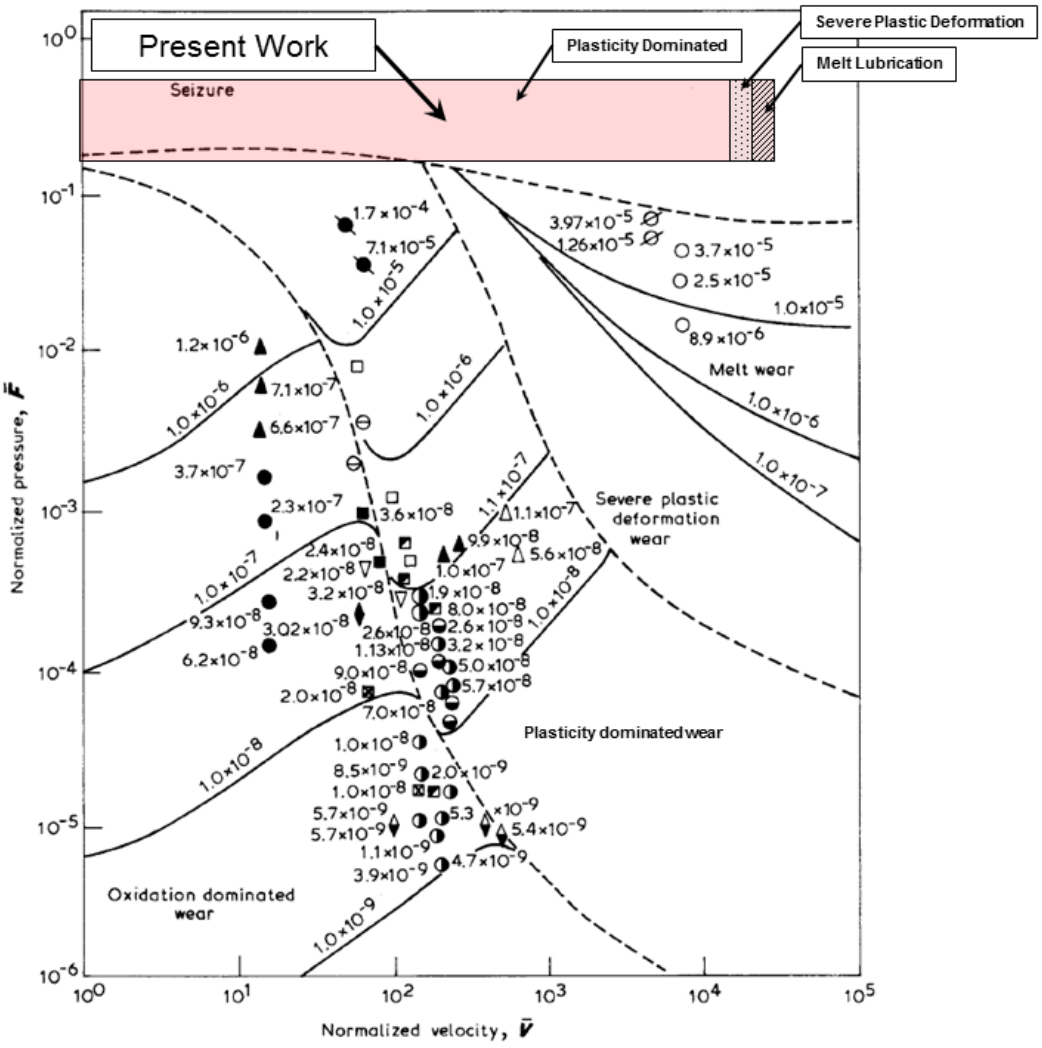

Figure 6.1 - An aluminum alloy wear mechanism map indicating the low and high wear rate regions under high sliding speeds [15].

regions (severe plastic deformation and melt lubrication) as it can be predicted using the heat dissipation rate constant.

Additionally, the critical velocity can be increased by selecting a guider material with a large volumetric thermal mass. In doing so the velocity range of the plasticity dominated wear region is extended. When operating in the plasticity dominated wear

region it is important to select a guider with a higher strength or hardness than the slider to ensure that deformation and wear is incurred in the slider at low sliding speeds. However, when operating in the severe plastic deformation and melt lubrication regions the guider strength is less important as the slider undergoes thermal softening and large scale melting.

A survey of available materials was conducted to identify potential candidates with both a high volumetric thermal mass and high hardness as shown in Figure 6.2. For visual purposes the inverse of both the volumetric thermal mass and hardness are plotted on a log-log scale. Ideal material candidates reside in the lower left corner of the plot. Several material groupings, metals and alloys (red), technical ceramics (yellow) and glasses

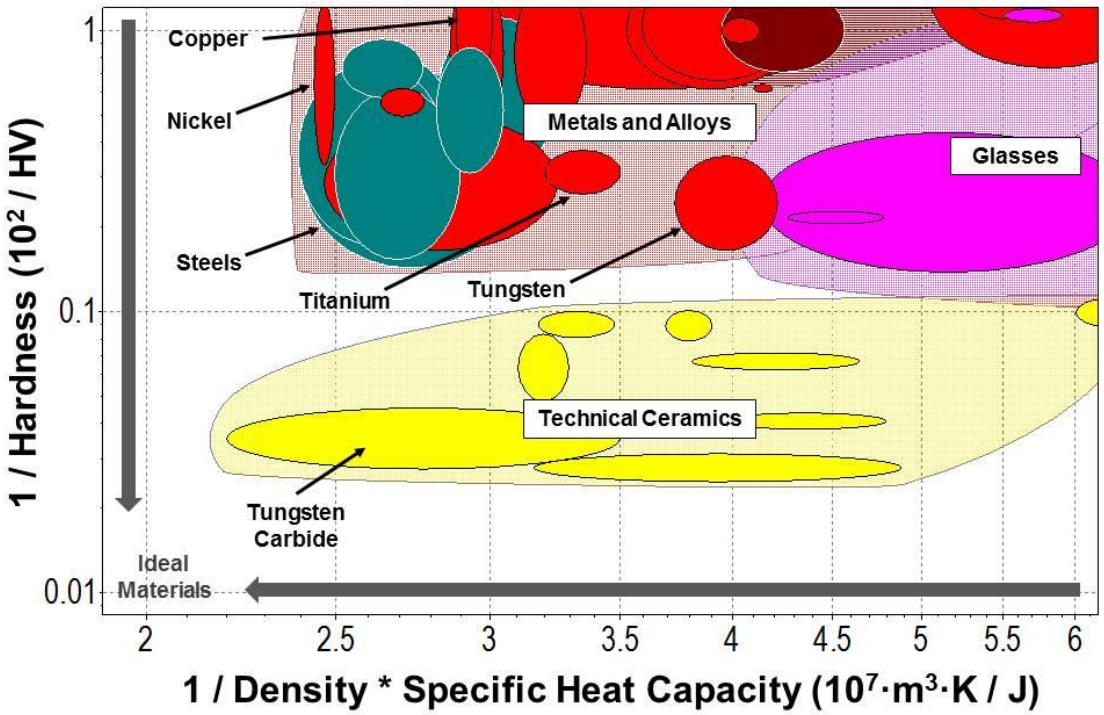

Figure 6.2 - Guider material selection targeting melt lubrication guider wear [5].

(magenta) appeared. Of these groupings the metals appear to have a large subset of materials with a high volumetric thermal mass and reasonable hardness. In particular steel, which is one of the guider materials tested, is a top performer of the metals. From the ceramics grouping, tungsten carbide is the top performer and the glass grouping is bounded by the metals and ceramics, making them less relevant. The results in Figure 6.2 do not take into account operating conditions, such as contact pressure and ductility limitations, which may further reduce the material groupings to a single subset of materials.

6.3 Guider Durability

6.3.1 Overview

During operation under extreme sliding contact a guider may experience severe plastic deformation, wear or fracture, all of which limit the useful service life of the guider. In order to make a slider-guider tribomaterial system more economically feasible a guider may need to be durable enough to withstand hundreds to thousands of cycles. There are three primary forms of guider damage that need to be considered and they are gouges, wear/erosion and fracture/fatigue. Each of the three primary forms of guider damage is discussed in detail and the associated material properties to maximize guider durability are identified.

6.3.1 Guider Damage: Gouges

Gouges are an inherent form of severe plastic deformation that occurs at the guider surface. They are typically teardrop shaped craters with the blunt end facing the direction of slider travel as shown in Figure 6.3. Guider gouging has been studied extensively over

the past forty plus years and was first reported by Graff and Dettloff [22] in rocket sled testing conducted in the 1960s. At the time sled velocity was attributed to the formation of the gouges. In 1982, Barber and Bauer [75] investigated sliding contact at low, high, and hypervelocities. Their gouge hypothesis was based on the principle of asperity contact at low velocities and asperity impact at high velocities. In 1997, Tarcza and Weldon [76] were able to show that gouges could be created at low velocities and that the gouging onset velocity could be predicted using the material properties of the slider. In 1999, Stefani and Parker [3] developed a model for predicting the gouge onset velocity using the hardness, mass densities, and Hugoniot values for a given slider-guider tribomaterial pairing. The model is capable of predicting gouge onset velocities for a given slider-guider tribomaterial pair, but does not account for surface coatings or lubrication, which can further delay the velocity at which gouging occurs [77].

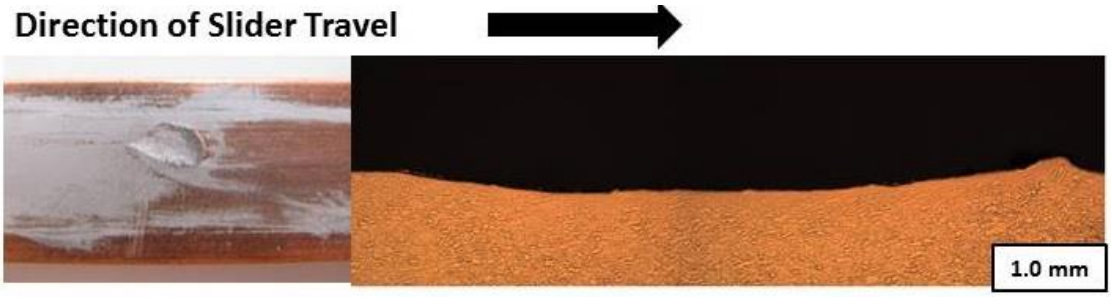

Figure 6.3 - An overhead view (left) and a side profile micrograph (right) of a gouge produced in Georgia Tech's minor caliber electromagnetic launcher.

Understanding the operating conditions (i.e. pressure and velocity) at which a gouge occurs is important when selecting a guider material. A gouge in the guider, if significant, could condemn the guider and require repair or replacement. For this reason it is

important to identify tribomaterial pairings with gouge velocities outside of the operating conditions. An established gouge model developed by Stefani and Parker [3] and published in more detail by Watt and Bourell [78] currently exists.

The principles behind the model are based on high-pressure shock compression theory, which is the result of an intense impulse loading in a solid medium that results in a shock wave [79]. A shock wave can be viewed as a discontinuity consisting of a particle velocity and a shock velocity. The particle velocity lags behind the shock velocity and it is the velocity that a segment of the solid acquires, whereas the shock velocity is the velocity that the disturbance moves through the solid body. Experimentally the response of a solid under these extreme conditions is studied using a flyer plate and a stationary target plate. The flyer plate is accelerated via a detonation of explosives such that it impacts the target plate at a high enough velocity to generate a shock wave. The state of a shocked solid can be found using the equation of state along with the three jump conditions (conservation of mass, momentum, and energy) to define a material specific Hugoniot curve. A Hugoniot curve represents all of the possible final physical states that can be achieved by a single shock wave for a given material and initial state. A Hugoniot curve may be expressed by any two of the following five variables: particle velocity, shock velocity, density, normal pressure, and specific internal energy.

A comparison can be made between the slider-guider surface to surface interaction to that of a flyer and target plate, where the slider is representative of the flyer plate and the guider is representative of the target plate. The Hugoniot P-u curves, where P is pressure and u is particle velocity, for a given slider-guider material combination can be plotted together, as shown in Figure 6.4. For a given normal planar shock pressure the two curves

intersect at a common point. The slider velocity necessary to create a gouge in the guider is equivalent to the sum of the slider and guider particle velocities. For a guider material to fail in the form of a gouge, the shock pressure must be greater than or equal to the strength of the guider material. Given a slider-guider tribomaterial pairing the shock pressure can be estimated as the material strength of the guider and using the Hugoniot P-u curves the gouge velocity can be calculated.

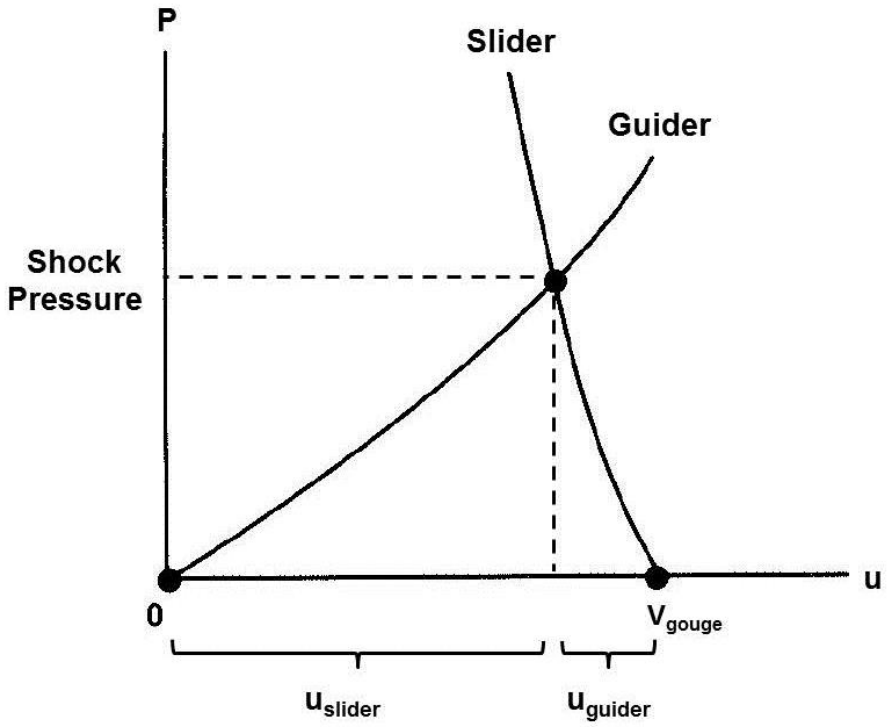

Figure 6.4 - Hugoniot P-u diagram for a guider and slider surface-to-surface interaction [79].

Gouges are inherently a form of extreme plastic deformation, so hardness can be used as an indicator of a metal's resistance to plastic deformation and in general it is proportional to ultimate tensile strength. For a materials screening / selection, ultimate

tensile strength is used. The upper bound of the normal planar shock pressure P_N is proportional to the ultimate tensile strength σ_{UTS} of the guider material.

$$P_N \propto \sigma_{UTS} \tag{6.1}$$

The normal planar shock pressure for a shock wave can be obtained through the conservation of momentum and is defined as

$$P_N = \rho \cdot U \cdot u \tag{6.2}$$

where ρ is density, U is shock velocity, and u is particle velocity. The shock velocity for a given material can be represented as a function of the particle velocity using Hugoniot U-u data as

$$U = C + s \cdot u \tag{6.3}$$

where C and s are experimentally fit parameters. Combining Equations 6.1 – 6.3 and solving for particle velocity using the quadratic equation gives way to the following form

$$u = \frac{-C}{2 \cdot s} + \frac{1}{2} \cdot \sqrt{\frac{C^2}{s^2} + \frac{4 \cdot \sigma_{UTS}}{\rho \cdot s}} \tag{6.4}$$

Referring back to Figure 6.4 the gouge threshold velocity v_{gouge} is the sum of the slider and guider particle velocities.

$$v_{gouge} = u_{guider} + u_{slider} \tag{6.5}$$

The gouge velocity, for the portion pertaining to the guider, can be maximized through Equation 6.4 and because Hugoniot data is not readily available for a wide range of materials, only ultimate tensile strength and density will be considered. Maximization of the gouge velocity v_{gouge} is proportional to ultimate tensile strength σ_{UTS} divided by density ρ. A guider material with a high ultimate tensile strength and a low density is desired

$$v_{gouge} \propto \left(\frac{\sigma_{UTS}}{\rho}\right)^{1/2} \tag{6.6}$$

Using published gouge experimental data and material properties, a plot of gouge velocity versus ultimate tensile strength and density is shown in Figure 6.5 [3, 5]. A general relationship between the experimental gouge velocity data and material properties of interest is apparent, confirming that for material screening purposes this relationship is reasonable.

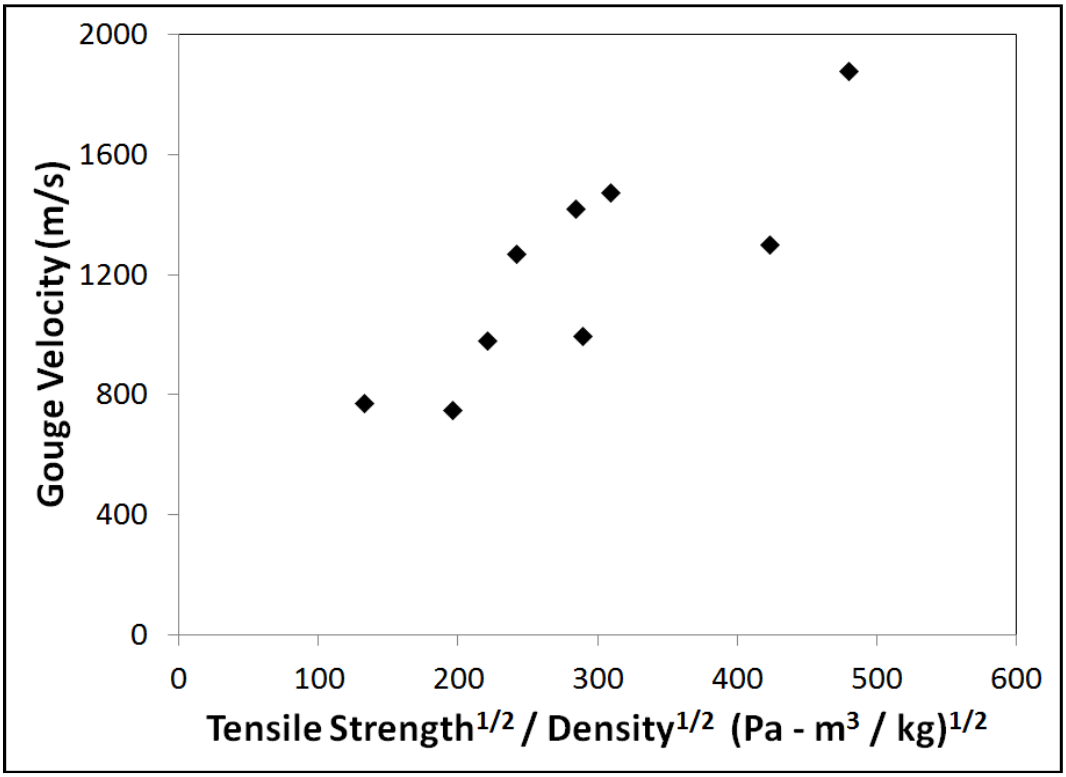

Figure 6.5 - A plot of experimental gouge velocity data versus ultimate tensile strength and density material properties [3, 5].

6.3.2 Guider Damage: Wear / Erosion

Erosion in large caliber cannon has been extensively researched over the past 60 years. Barrel erosion or multishot wear due to the interaction of the projectile and barrel rifling is complex and often times involves thermal, chemical, and mechanical erosion

mechanisms [74, 80, 81]. However, the primary driver for barrel erosion is temperature related as high temperatures reduce barrel mechanical properties and leave the barrel susceptible to corrosion. Significant research has been conducted on mitigating these temperature effects through the use of coatings and lubrication [82, 83].

In addition to conventional gun barrels, multishot wear has more recently become an issue in electromagnetic launchers as the barrel is exposed to extreme electrical sliding contact [84]. Multishot wear in EML barrels has been attributed to excessive Joule heating that is intensified by high sliding speeds that produce high localized barrel temperatures [62, 84]. These high localized temperatures result in thermal softening of the barrel material. This thermal softening combined with the high velocity flow of molten metal from the melting projectile, facilitates chemical dissolution of the barrel material into the molten material, which results in barrel erosion [63, 85].

In both applications research has shown that high localized temperatures are the driver for barrel or guider erosion. High temperatures are prevalent in all three wear regions of interest: plasticity dominated, severe plastic deformation and melt lubrication. At low sliding speeds and high contact pressures the high temperatures can be attributed to Coulomb heating, while at high sliding speeds and high contact pressures they can be attributed to viscous heating. A material screening index for guider wear can be derived through an energy balance

$$E_{in} - E_{out} = E_{storage} \tag{6.7}$$

where E_{in} is the heat energy input into a portion of the guider material near the surface, E_{out} is the heat energy removed via diffusion, and $E_{storage}$ is the heat energy absorbed. E_{in} is composed of two components. If the energy input into the guider E_{in} is due to Coulomb heating it is defined [45]

$$E_{in} = fWl \tag{6.8}$$

where f is the coefficient of friction, W is the normal load, l is the slider length. For viscous dissipation, representative of the melt lubrication region, the energy input into the guider is defined [45]

$$E_{in} = \mu \frac{v}{h} A_n 2l \tag{6.9}$$

where μ is the dynamic viscosity, v is the slider velocity, h is the thickness of the slider melt film, A_n is the nominal contact area and $2l$ is the slider length. Both of the heat sources presented in Equations 6.8 and 6.9 are rather simplistic views of the slider guider interface physics. Particularly the viscous dissipation heat source, which has been shown to be turbulent making the melt lubrication film physics complex.

For the sliding speeds and geometries used in the aforementioned experiments, the dwell times for a section of the guider, due to the high sliding speeds, is on the order of a microsecond. For a given set of guider material properties the diffusion time or the time it takes to diffuse the heat at the guider surface into the bulk material is much larger relative to the dwell time. Based on this reasoning a simplifying assumption is made that there is insufficient time for diffusion to occur and the E_{out} term of the energy balance in Equation 6.7 is negligible. A transient conduction problem using a lumped capacitance approach is taken and assumes the volume of material near the guider surface has a spatially uniform temperature distribution. The heat energy absorbed by the guider material near the surface is represented as follows

$$E_{storage} = \bar{V} \cdot \rho \cdot c \cdot (\Delta T) \tag{6.10}$$

where ΔT is the rise in temperature, $\bar{V}$ is the volume of material that absorbs the heat energy, c is the specific heat capacity of the guider material, and ρ is the density. Combining Equations 6.7 and 6.10, the increase in guider temperature is defined

$$\Delta T = \frac{E_{in}}{\bar{V} \cdot \rho \cdot c} \tag{6.11}$$

However, a material with a high melting temperature exposed to the same rise in temperature may not experience the same material damage as a material with a lower melting temperature. This is accounted for by dividing Equation 6.11 by the melting temperature T_m, giving it the dimensionless form,

$$\frac{\Delta T}{T_m} = \frac{E_{in}}{\bar{V} \cdot \rho \cdot c \cdot T_m} \tag{6.12}$$

Wear resistance is maximized through the guider material properties: mass density, specific heat capacity, and melting temperature. Additional considerations should be made related to the chemical interactions between the slider melt lubrication film and the guider material. Dissolution of the guider material into the slider melt is possible if the guider surface temperatures are high enough and the slider-guider tribomaterial pairing have an affinity towards each other [63, 86, 87].

6.3.3 Guider Damage: Fatigue / Fracture

The final form of guider damage that needs to be considered is fatigue / fracture. It has been shown in gun barrel coatings that repeated thermal cycling can cause thermo-mechanical cracking near the surface [88]. Extensive research has been conducted on modeling these conditions [89-91]. A simple thermal stress model can be used as a check

to ensure that tensile residual stresses are avoided upon cooling [82]. The applied thermal stress damage mechanism is defined as follows

$$S_T = \frac{E \cdot \alpha_T \cdot (T - T_o)}{(1 - \upsilon)} \tag{6.13}$$

where E is the modulus of elasticity, α_T is the coefficient of thermal expansion, T is temperature, T_o is the initial temperature, and υ is Poisson's ratio. For brittle materials, such as coatings, if the thermal stresses exceed the compressive yield strength at temperature, $S_{y,c}$ than residual tensile stresses will form on cooling. To avoid crack formation the following criteria needs to be met

$$\frac{S_{y,c}}{S_T} > 1 \tag{6.14}$$

The material selection criterion of Equation 6.14 is important for brittle materials where the strain-to-fracture is relatively low. Additionally, surface treatments such as coatings, can have residual stresses and microvoids / microcracks due to processing techniques [92]. These residual stresses can be accounted for by superimposing them onto the thermal stresses when evaluating the thermal stress damage mechanism [93]. Microvoids and microcracks coupled with relatively low fracture toughness and low

substrate stiffness can lead to fracture and need to be minimized during material processing. For these reasons ductility also needs to be considered when screening / selecting guider materials. Material properties such as fracture toughness or fatigue are avoided as material property data can be difficult to obtain or not readily available for a wide range of materials. A more simplistic and readily available material property is elongation or strain-to-fracture ε_f .

A survey of available materials was conducted to identify potential candidates with both a high compressive strength and high strain-to-fracture as shown in Figure 6.6. For visual purposes the inverse of both the material properties are plotted on a log-log scale. Ideal material candidates reside in the lower left corner of the plot. Several material groupings appeared; elastomers (aqua), polymers (blue), metals and alloys (red), and natural materials (green). Of these groupings the metals and alloys have a large subset of materials with a high compressive stress and reasonable strain-to-fracture. Steels, which were one of the guider materials tested, is a top performer of the metals. The ceramics material group screened out as they have relatively poor strain-to-fracture properties. The results in Figure 6.6 do not take into account operating conditions that result in high temperatures at the slider-guider interface, in which case the elastomers, polymers and natural materials would all screen out as they do not have the same relative temperature capability as the metals and alloys. This leaves the metals and alloys material group as the top performing materials group with steels being an attractive subgroup.

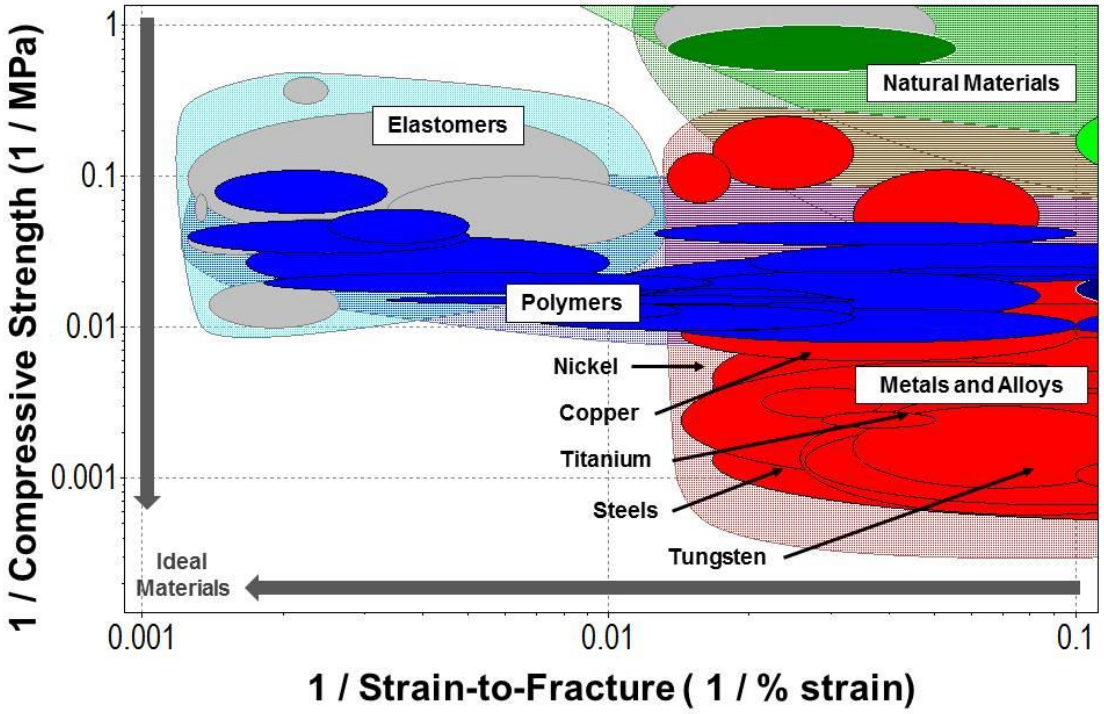

Figure 6.6 - Guider material selection for the fatigue / fracture damage mechanisms [5].

6.4 Materials Selection

The aforementioned forms of rail damage provide the background necessary for identifying the desired material attributes for rail durability. A systematic materials selection process, often referred to as the Ashby method, can be used in conjunction with the material properties presented in this chapter to screen and evaluate guider material solutions for further investigation [94]. The approach starts with a large electronic database of materials that covers the major engineering material families (metals, ceramics, glasses, polymers, elastomers, and hybrids) so that new or unforeseen

opportunities are not overlooked. The four steps include translating the design requirements, screening using constraints, ranking using objectives, and then exploring top ranked material solutions further with more in-depth analysis.

For engineering applications with multiple objectives it is often times advantageous to use a hybrid material configuration. Four potential hybrid material configurations that may be of interest include a fibrous composite, particulate composite, a monolayer structure, and a multilayer structure, as shown in Figure 6.7. For extreme sliding contacts the drawback to the first two hybrid configurations, fibrous and particulate composites, is that while the bulk properties are improved, locally at the guider surface durability is still a concern as the matrix material may still be susceptible to damage. However, this is not the case for the monolayer and multilayer structures which can be configured for durability at the guider surface. Furthermore each of these hybrid configurations adds different amounts of complexity in fabrication, which may incur additional cost over the use of a monolithic guider material.

The most relevant configuration for extreme sliding contact with multiple objectives is a monolayer structure with a guider surface material that maximizes durability. Wear rates and temperature gradients need to be considered when sizing the thickness of the guider surface material. Additionally, in repetitive use applications where the bulk material of the guider experiences a rise in temperature, the mismatch of the coefficients of thermal expansion between layers needs to be considered. This may result in the addition of an intermediate layer in which case a multilayered hybrid configuration is ideal.

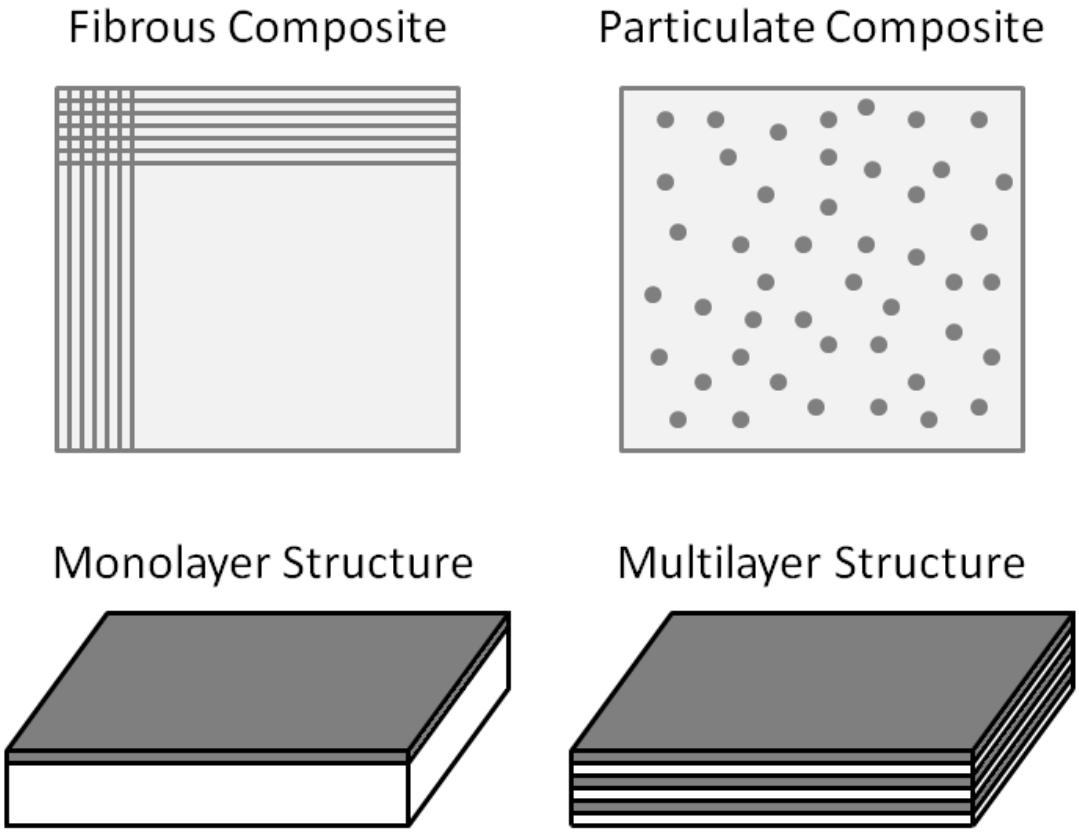

Figure 6.7 - Four potential hybrid material configurations for a durable guider material.

CHAPTER 7: Summary, Conclusions, Scientific Contributions and Recommendations

7.1 Summary

7.1.1 Chapter 1: Background

In Chapter 1 an extensive literature review was conducted on the subject of sliding contact under high sliding speeds and high contact pressures with a focus on metal on metal sliding at speeds greater than 200 m/s. Safety concerns and limitations in test equipment make it difficult to replicate these extreme sliding conditions using traditional tribological test apparatuses. For these reasons many one of a kind apparatuses have been developed and often times modifications to the existing engineering application equipment is necessary to isolate and study extreme sliding contact.

The study of sliding contacts can be viewed as the interaction of a moving solid, referred to as the slider with a stationary solid, referred to as the guider. The interaction of the slider and guider at the contact interface results in wear of one or both of the solids. For high sliding speeds and high contact pressures of metal on metal contact two distinct operating regions are identified. The first is melt wear, which is representative of localized melting at the asperity level with a primary heat mechanism of frictional dissipation. This region is characterized by a low coefficient of friction and low wear rates. The second region is melt lubrication, which is representative of large scale melting with a primary heating mechanism that is viscous in nature and is characterized by a high coefficient of friction and high wear rates.

7.1.2 Chapter 2: Experimental Methodology

A novel approach to studying mechanical wear of sliding metal contacts under high sliding speeds and contact pressures was developed using the Georgia Tech lab scale electromagnetic launcher (EML). Sliding speeds in excess of 1,000 m/s were achieved and an inertia loaded wedge technique was used to replicate contact pressures in the range of 100 – 225 MPa. Modifications to the EML core allowed for different tribomaterial pairings to be explored. A qualitative assessment of slider wear was performed using optical microscopy; while a quantitative assessment was conducted using a scanning white light interferometer. The resultant slider wear was correlated to the operating conditions of pressure and velocity.

7.1.3 Chapter 3: Experimental Results: Wear Regimes

In Chapter 3 the results of a tribomaterial pairing of 6061-T6 aluminum sliding on a C110-H2 copper guider at 101 MPa and a peak velocity of 1,210 m/s was analyzed. A qualitative and quantitative assessment of slider wear as a function of velocity showed three distinct wear regions: plasticity dominated, severe plastic deformation and melt lubrication. At lower velocities, 200 – 800 m/s, the slider wear is characteristic of plasticity dominated wear. The severe plastic deformation region occurred at a velocity, typically between 800 – 1,000 m/s, during which the slider wear transitioned from plasticity dominated wear to melt lubrication. At high velocities, >1,000 m/s the slider wear is characterized as melt lubrication. A correlation between normalized wear rates as a function of velocity between these three regions and that of hydrodynamic lubrication theory were made using a Stribeck curve. It was concluded that portions of the severe plastic deformation and melt lubrication regions followed similar trends to that of the

mixed and hydrodynamic lubrication regions of a Stribeck curve and the conditions of the melt lubrication film are representative of turbulent flow.

7.1.4 Chapter 4: Experimental Results: Velocity and Pressure

In Chapter 4 the results of a tribomaterial pairing of 6061-T6 aluminum slider on a C110-H2 guider to investigate the effects of pressure and velocity on normalized wear rates was conducted. Five different pressures in the range of 100 – 225 MPa and peak velocities of 1,200 m/s were investigated. Normalized wear rates for the melt lubrication region showed a strong dependence on velocity. The velocity at which the type of wear transitions from severe plastic deformation to melt lubrication also called the critical velocity was sensitive to pressure. Higher pressures resulted in lower critical velocities. Additionally, the normalized wear rate data showed a strong dependence on the parameter $\sigma^{1/4}v$, where σ is nominal contact pressure and v is velocity, which correlates well with melt lubrication theory for turbulent flow. Additionally it was found that effects of the slider nominal contact area on normalized wear rates were negligible for the slider geometries tested.

A constitutive model was developed capable of predicting normalized wear rates in the melt lubrication region. The normalized wear rates were found to be proportional to $\sigma^{1/4}v$ and the proportionality constant, Ψ, was found to be a function of the slider viscosity, geometry and thermal properties.

7.1.5 Chapter 5: Experimental Results: Guider Material Properties

In Chapter 5 the results of three different tribomaterial pairings were tested to investigate the effects of guider material properties on slider wear. For all three tests a

6061-T6 aluminum slider was tested. Heat partition theory for sliding contacts was used to select three different guider materials: C110-H2 copper, 1018 / 1045 steel, and titanium grade 2 commercial purity. Test results differed from predictions using traditional heat partition theory. For extreme sliding contacts in the severe plastic deformation and melt lubrication regions it was found that volumetric thermal mass of the guider ($\rho \cdot c$), not thermal diffusivity, was the material property of interest. A guider with a larger volumetric thermal mass resulted in a high critical velocity, meaning that more heat was partitioned into a guider than one with a lower volumetric mass.

Additionally the effects of guider mechanical properties were investigated. Two different steels, 1018 and 1045, with similar bulk thermal properties were tested. The effects of guider mechanical properties were found to be negligible in the severe plastic deformation and melt lubrication regions as the slider had undergone significant thermal softening. The constitutive model developed in Chapter 4 was updated into a more general form to include the effects of guider material properties on slider wear.

7.1.6 Chapter 6: Guider Durability Considerations

In Chapter 6 a list of relevant guider material properties as they relate to slider wear and guider durability were considered. For the case of slider wear the volumetric thermal mass of the guider material influenced the critical velocity at which melt lubrication occurs and needs to be considered when selecting tribomaterial pairings for engineering applications. For guider durability there are three primary forms of damage: gouges, wear / erosion, and fracture. To avoid gouging it is ideal to select materials with a high ultimate tensile strength and low density. Minimization of guider erosion can be achieved by selecting materials with high melt energies and avoiding tribomaterial pairings that

have an affinity towards each other. Lastly, fatigue and fracture can be mitigated by accounting for thermal stresses and identifying materials with moderate ductility.

7.2 Conclusions

The conclusions of the research conducted in this dissertation is as follows

1) The experimental data supports the use of melt lubrication theory for high sliding speeds and high contact pressures.
2) The heat dissipation mechanism in the melt lubrication region is viscous and turbulent in nature.
3) The slider normalized wear rates are insensitive to the guider hardness and sensitive to the volumetric thermal mass in the severe plastic deformation and melt lubrication regions.
4) A guider material with a high ultimate tensile strength, low density, high melting point, high compressive strength and moderate ductility is ideal for maximizing durability when the slider is operating in the severe plastic deformation and melt lubrication regions.

7.3 Scientific Contributions

The scientific contributions of the research conducted in this dissertation is as follows

1) *Development of a New Experimental Method*

   A one of a kind experimental methodology for studying high speed sliding contact was developed. This methodology provides the flexibility to study different tribomaterial pairings under sliding conditions beyond that of typical tribological test apparatuses. The experimental data obtained from the high velocity and high contact

pressure wear experiments provides new wear data beyond that of existing published literature.

2) *Clarification of Wear Mechanisms*

Three different wear regions were identified: plasticity dominated, severe plastic deformation and melt lubrication. Operating boundaries for each of these regions was established through the use of qualitative and quantitative analysis. An additional wear region, melt lubrication was defined on the aluminum wear mechanism map.

3) *Effects of Pressure and Velocity on Melt Lubrication*

Pressure effects on melt lubrication were characterized. It was found that the normalized wear rate data is sensitive to $\sigma^{1/4}v$, where σ is nominal contact pressure and v is velocity, which supports the use of melt lubrication theory.

4) *Influence of Guider Material Properties*

The heat partition coefficients or effects of guider material properties on slider wear in the melt lubrication region were studied. It was found that the volumetric thermal mass of the guider, not thermal diffusivity, influences the conditions at which melt lubrication occurs.

5) *Empirical Wear Model*

A normalized wear rate constitutive model that captures the operating conditions, slider geometry and material properties, and guider material properties was developed such that it can be used to predict wear and used to design more efficient and effective tribological systems under extreme sliding contact.

6) *Melt Film Physics*

The experimental methodology and data provides the foundation for future research in exploring the physics (i.e. heat transfer, fluid dynamics) of the melt lubrication film.

7.4 Recommendations

The recommendations for future research is as follows

1) *Extend Existing Wear Mechanism Maps*

   Include a new wear region identified as melt lubrication.

2) *Exploration of the Melt Lubrication Proportionality Constant*

   Understand the sensitivity of the slider geometry and thermal properties on normalized wear rates. This would include testing slider materials with vastly different aspect ratios and melt energies.

3) *Investigate the Heat Dissipation Rate Constant*

   Study how the mechanical and thermal properties of the slider influence the heat dissipation value at which the slider wear transitions from severe plastic deformation to melt lubrication.

APPENDIX A

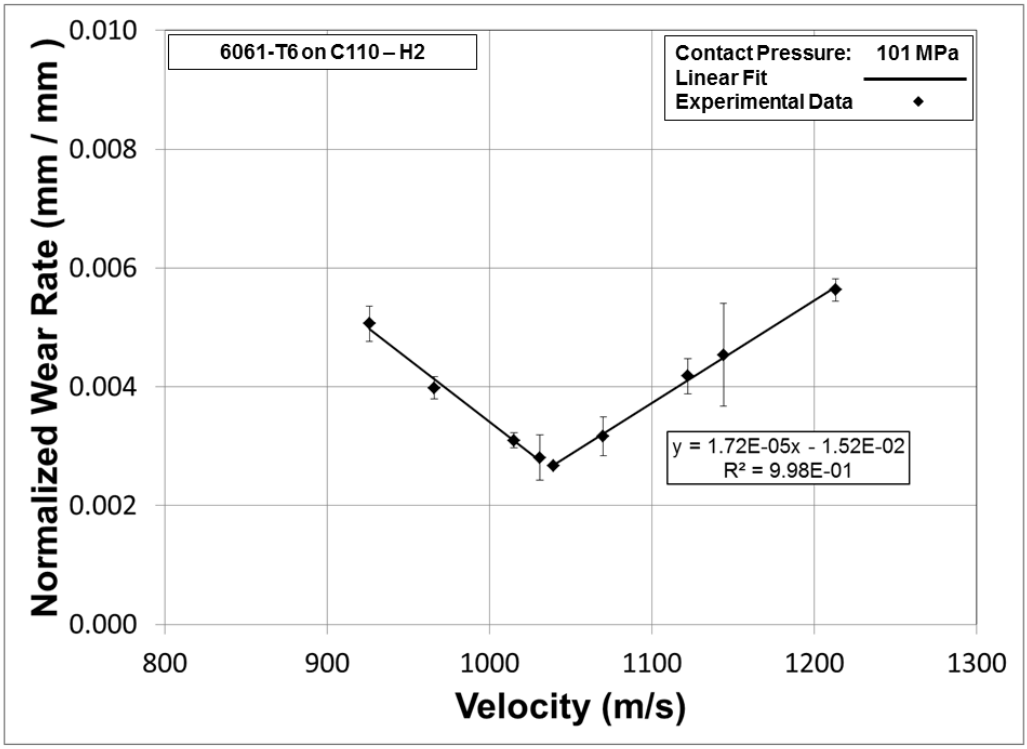
6061-T6 on C110 – H2
Contact Pressure: 101 MPa
Linear Fit
Experimental Data
y = 1.72E-05x - 1.52E-02
R² = 9.98E-01
Normalized Wear Rate (mm / mm)
0.010
0.008
0.006
0.004
0.002
0.000
800
900
1000
1100
1200
1300
Velocity (m/s)

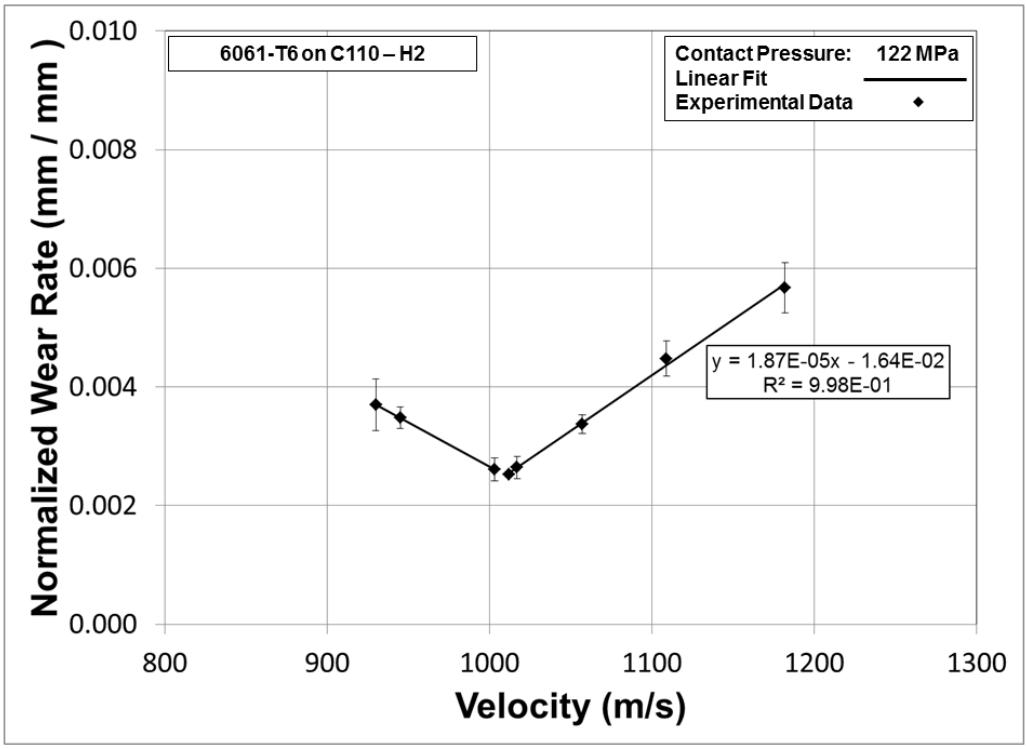
6061-T6 on C110 – H2
Contact Pressure: 122 MPa
Linear Fit
Experimental Data
y = 1.87E-05x - 1.64E-02
R² = 9.98E-01
Normalized Wear Rate (mm / mm)
0.010
0.008
0.006
0.004
0.002
0.000
800
900
1000
1100
1200
1300
Velocity (m/s)

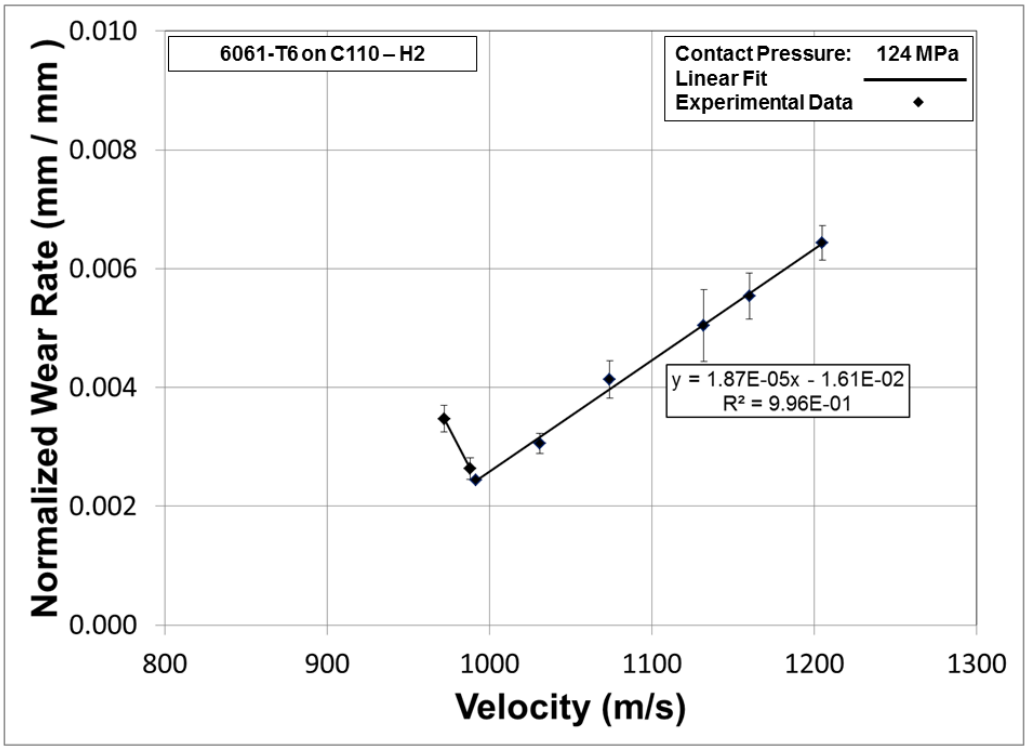
6061-T6 on C110 – H2
Contact Pressure: 124 MPa
Linear Fit
Experimental Data
y = 1.87E-05x - 1.61E-02
R² = 9.96E-01
Normalized Wear Rate (mm / mm)
0.010
0.008
0.006
0.004
0.002
0.000
800
900
1000
1100
1200
1300
Velocity (m/s)

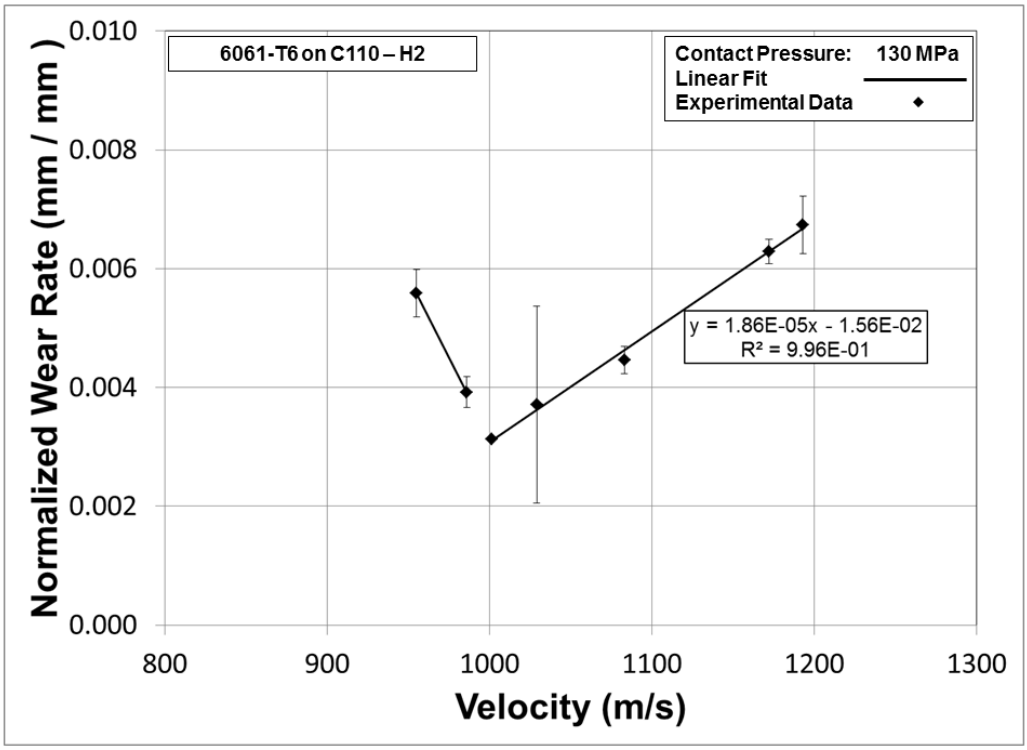
6061-T6 on C110 – H2
Contact Pressure: 130 MPa
Linear Fit
Experimental Data
y = 1.86E-05x - 1.56E-02
R² = 9.96E-01
Normalized Wear Rate (mm / mm)
0.010
0.008
0.006
0.004
0.002
0.000
800
900
1000
1100
1200
1300
Velocity (m/s)

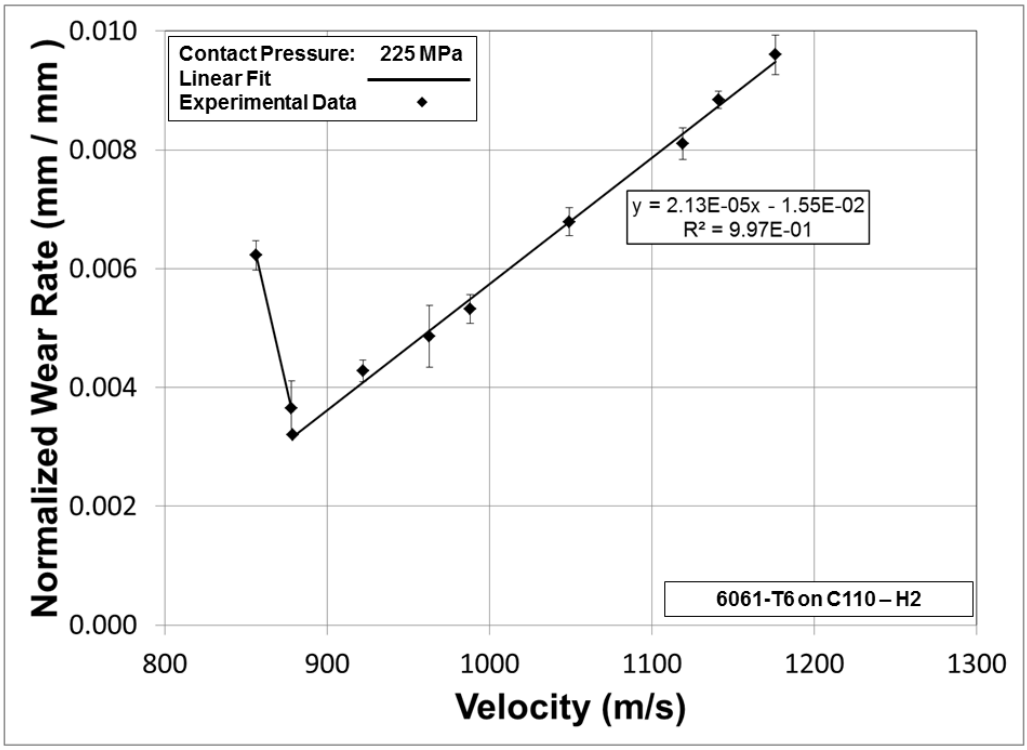
Contact Pressure: 225 MPa
Linear Fit
Experimental Data
y = 2.13E-05x - 1.55E-02
R² = 9.97E-01
6061-T6 on C110 – H2
Normalized Wear Rate (mm / mm)
Velocity (m/s)
0.010
0.008
0.006
0.004
0.002
0.000
800
900
1000
1100
1200
1300

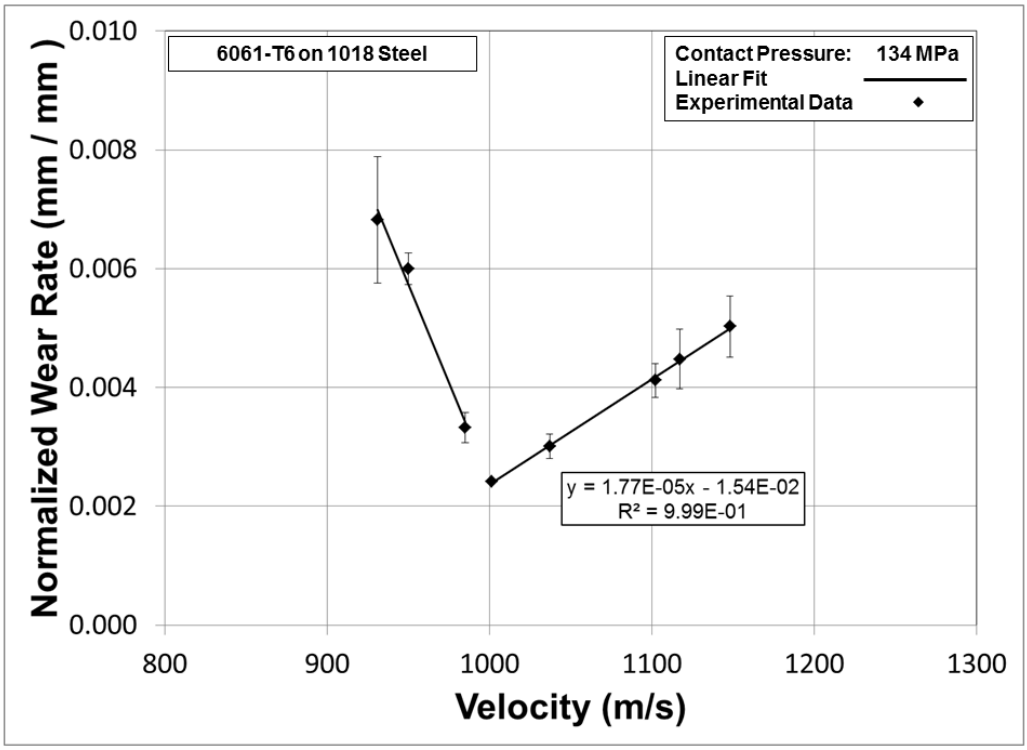
6061-T6 on 1018 Steel
Contact Pressure: 134 MPa
Linear Fit
Experimental Data
y = 1.77E-05x - 1.54E-02
R² = 9.99E-01
Normalized Wear Rate (mm / mm)
Velocity (m/s)
0.010
0.008
0.006
0.004
0.002
0.000
800
900
1000
1100
1200
1300

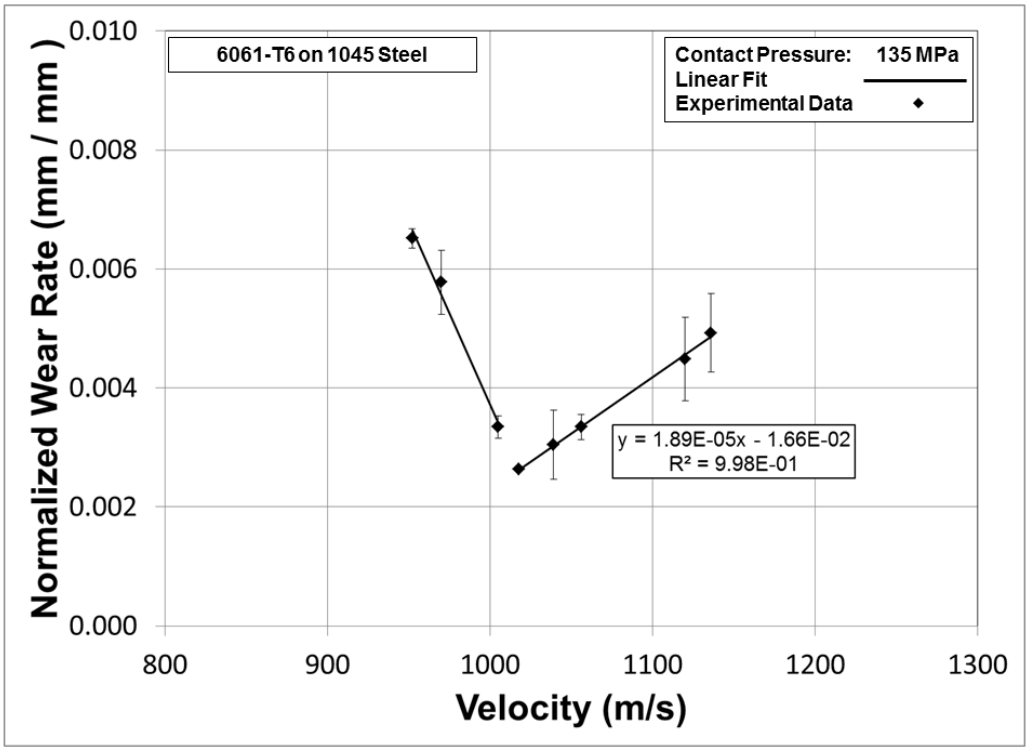
6061-T6 on 1045 Steel
Contact Pressure: 135 MPa
Linear Fit
Experimental Data
y = 1.89E-05x - 1.66E-02
R² = 9.98E-01
Normalized Wear Rate (mm / mm)
Velocity (m/s)
0.010
0.008
0.006
0.004
0.002
0.000
800
900
1000
1100
1200
1300

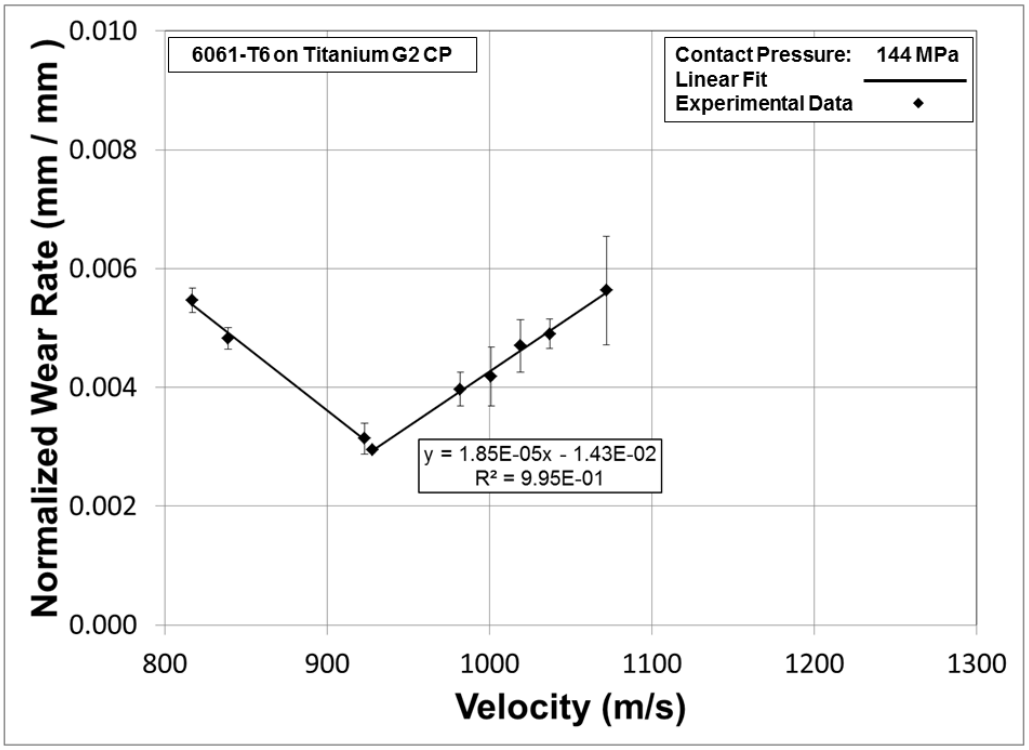
6061-T6 on Titanium G2 CP
Contact Pressure: 144 MPa
Linear Fit
Experimental Data
y = 1.85E-05x - 1.43E-02
R² = 9.95E-01
Normalized Wear Rate (mm / mm)
Velocity (m/s)
0.010
0.008
0.006
0.004
0.002
0.000
800
900
1000
1100
1200
1300

APPENDIX B

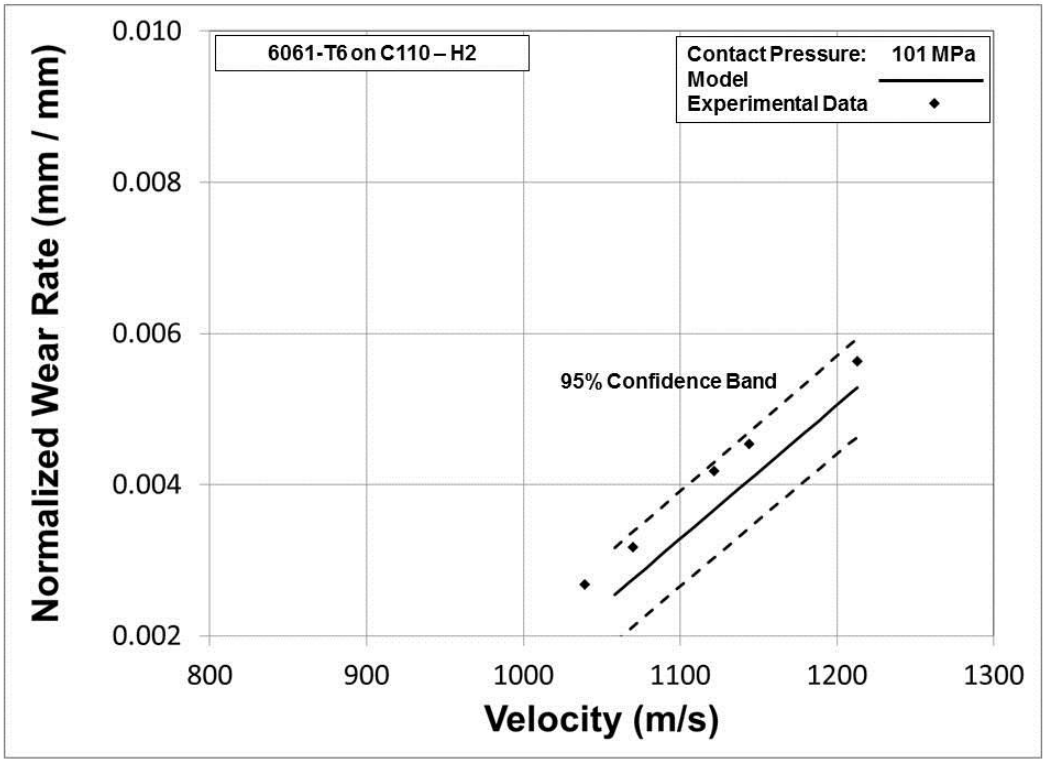
6061-T6 on C110 – H2
Contact Pressure: 101 MPa
Model
Experimental Data
95% Confidence Band
Normalized Wear Rate (mm / mm)
0.010
0.008
0.006
0.004
0.002
800
900
1000
1100
1200
1300
Velocity (m/s)

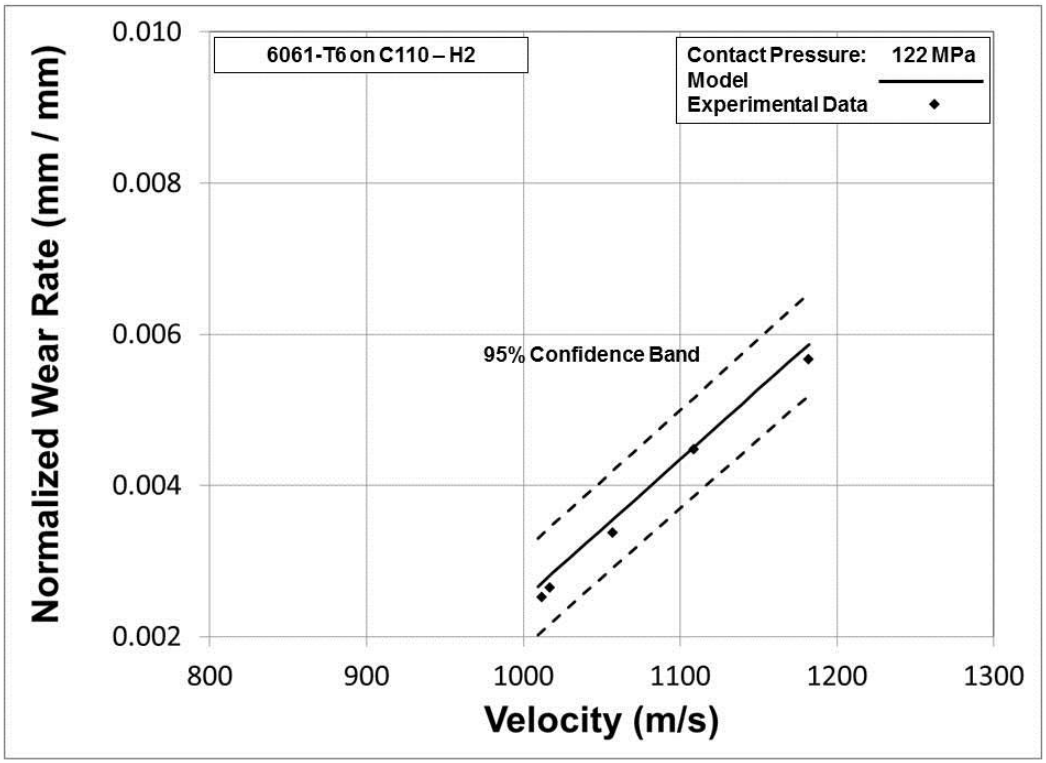
6061-T6 on C110 – H2
Contact Pressure: 122 MPa
Model
Experimental Data
95% Confidence Band
Normalized Wear Rate (mm / mm)
0.010
0.008
0.006
0.004
0.002
800
900
1000
1100
1200
1300
Velocity (m/s)

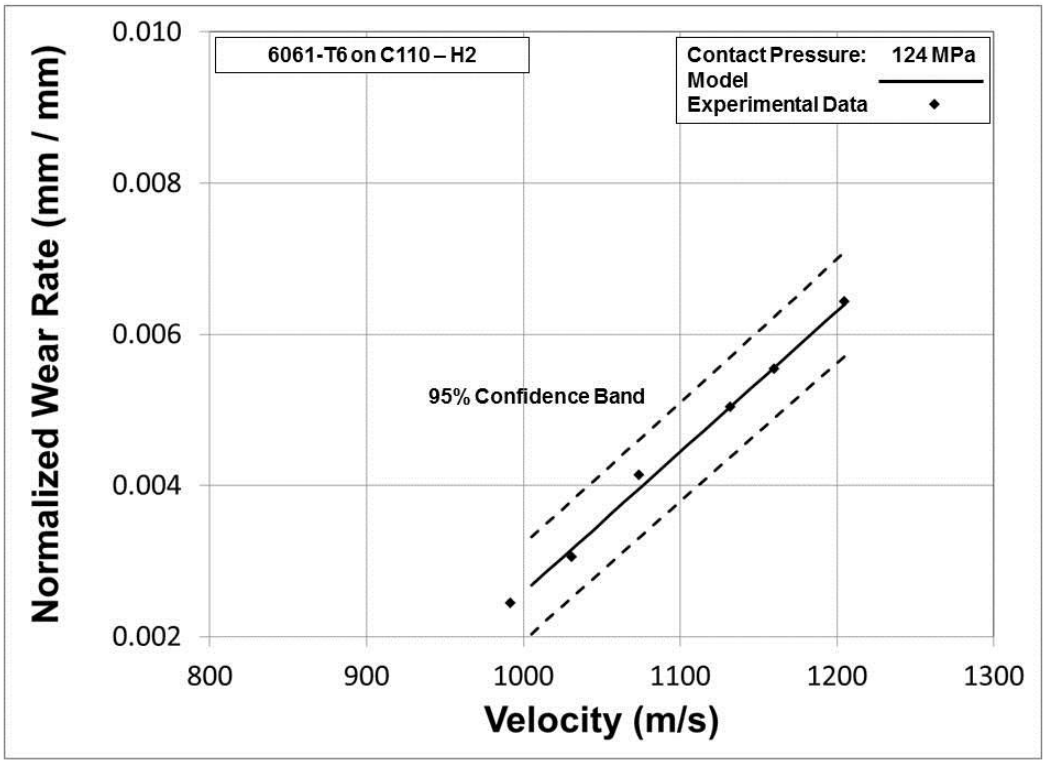
6061-T6 on C110 – H2
Contact Pressure: 124 MPa
Model
Experimental Data
95% Confidence Band
Normalized Wear Rate (mm / mm)
Velocity (m/s)
0.010
0.008
0.006
0.004
0.002
800
900
1000
1100
1200
1300

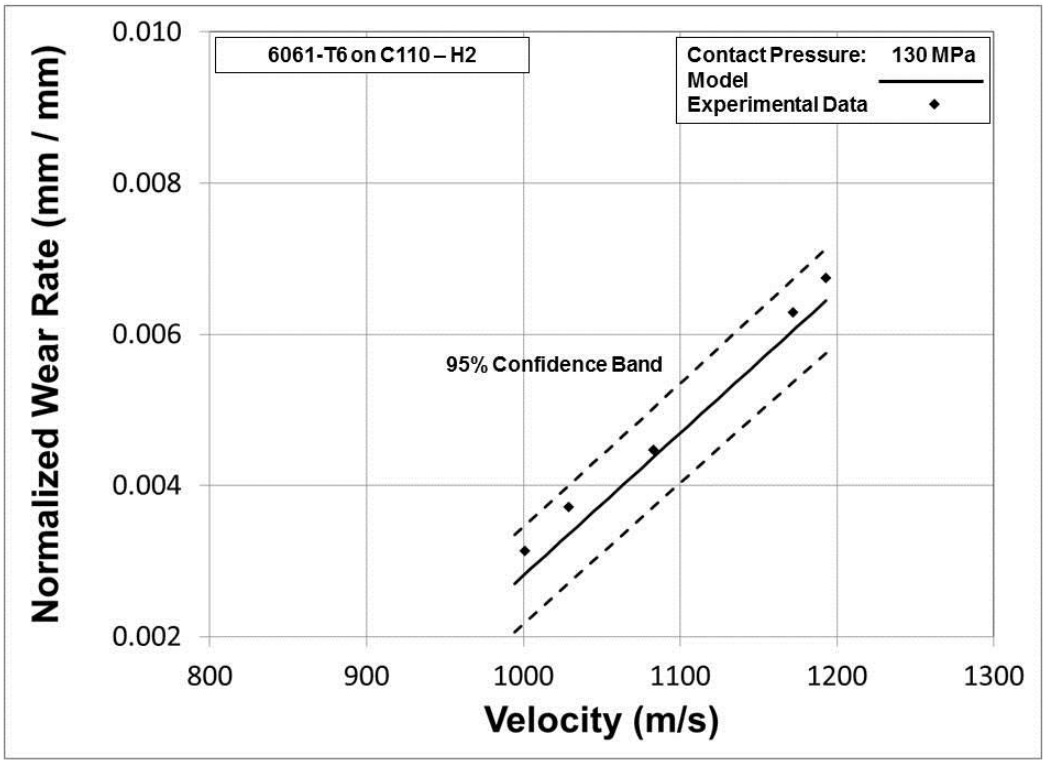
6061-T6 on C110 – H2
Contact Pressure: 130 MPa
Model
Experimental Data
95% Confidence Band
Normalized Wear Rate (mm / mm)
Velocity (m/s)
0.010
0.008
0.006
0.004
0.002
800
900
1000
1100
1200
1300

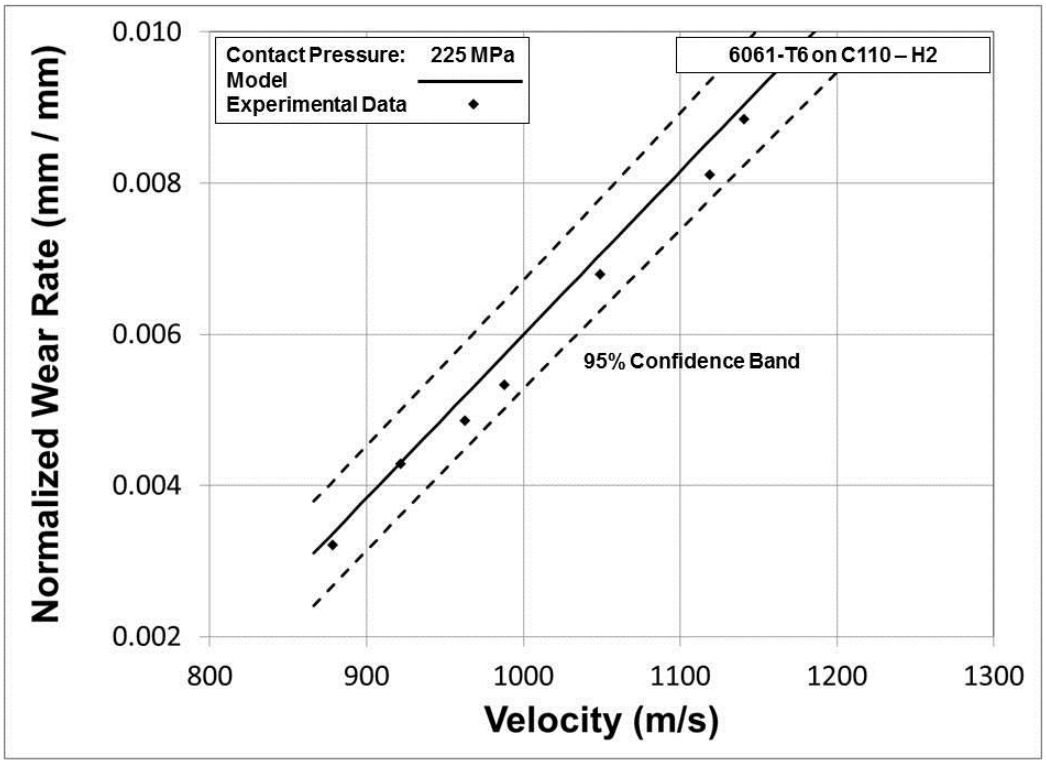
Contact Pressure: 225 MPa
Model
Experimental Data
6061-T6 on C110 – H2
95% Confidence Band
Normalized Wear Rate (mm / mm)
Velocity (m/s)
0.010
0.008
0.006
0.004
0.002
800
900
1000
1100
1200
1300

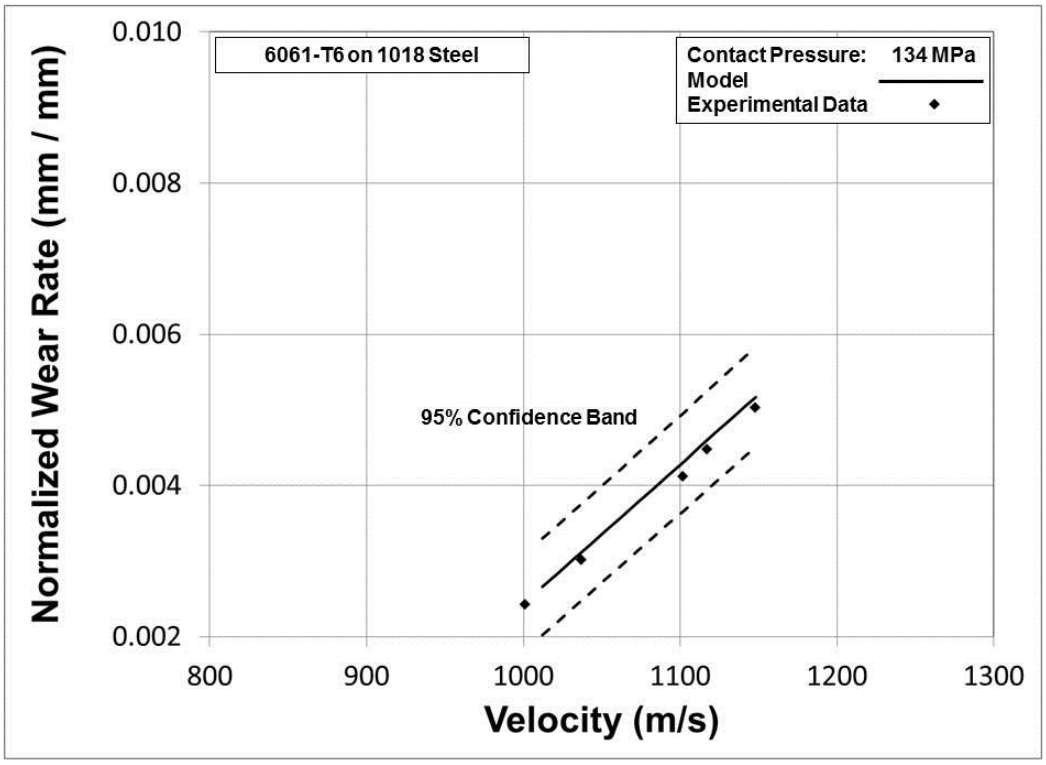
6061-T6 on 1018 Steel
Contact Pressure: 134 MPa
Model
Experimental Data
95% Confidence Band
Normalized Wear Rate (mm / mm)
Velocity (m/s)
0.010
0.008
0.006
0.004
0.002
800
900
1000
1100
1200
1300

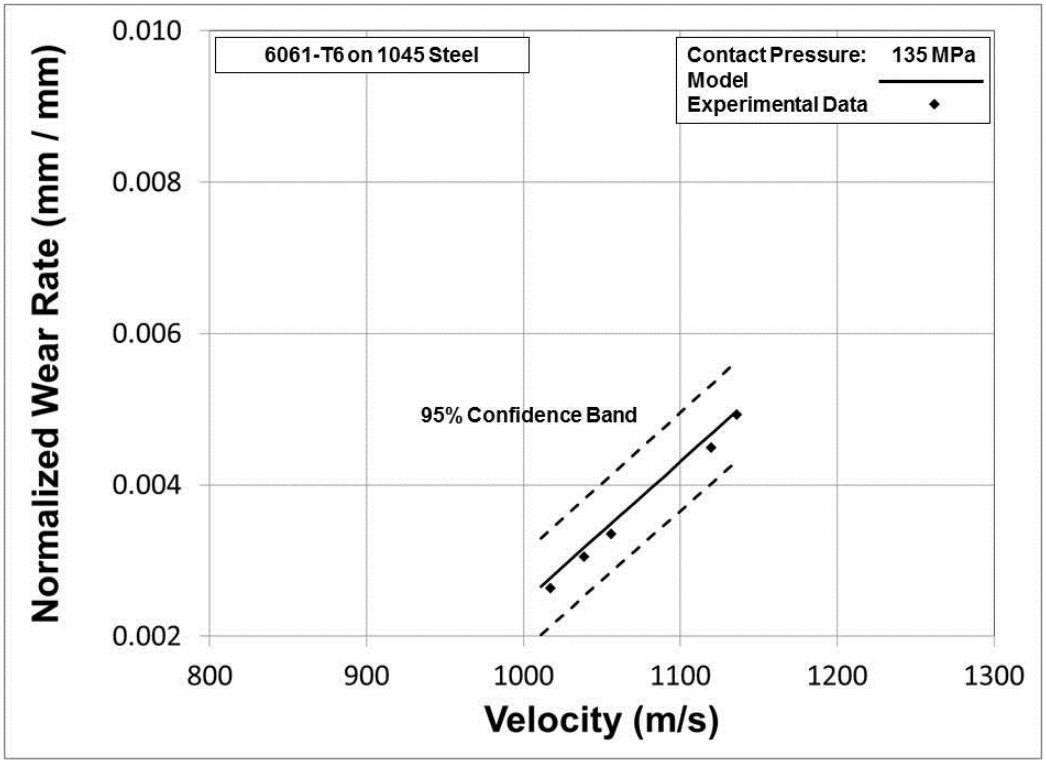
6061-T6 on 1045 Steel
Contact Pressure: 135 MPa
Model
Experimental Data
95% Confidence Band
Normalized Wear Rate (mm / mm)
0.010
0.008
0.006
0.004
0.002
800
900
1000
1100
1200
1300
Velocity (m/s)

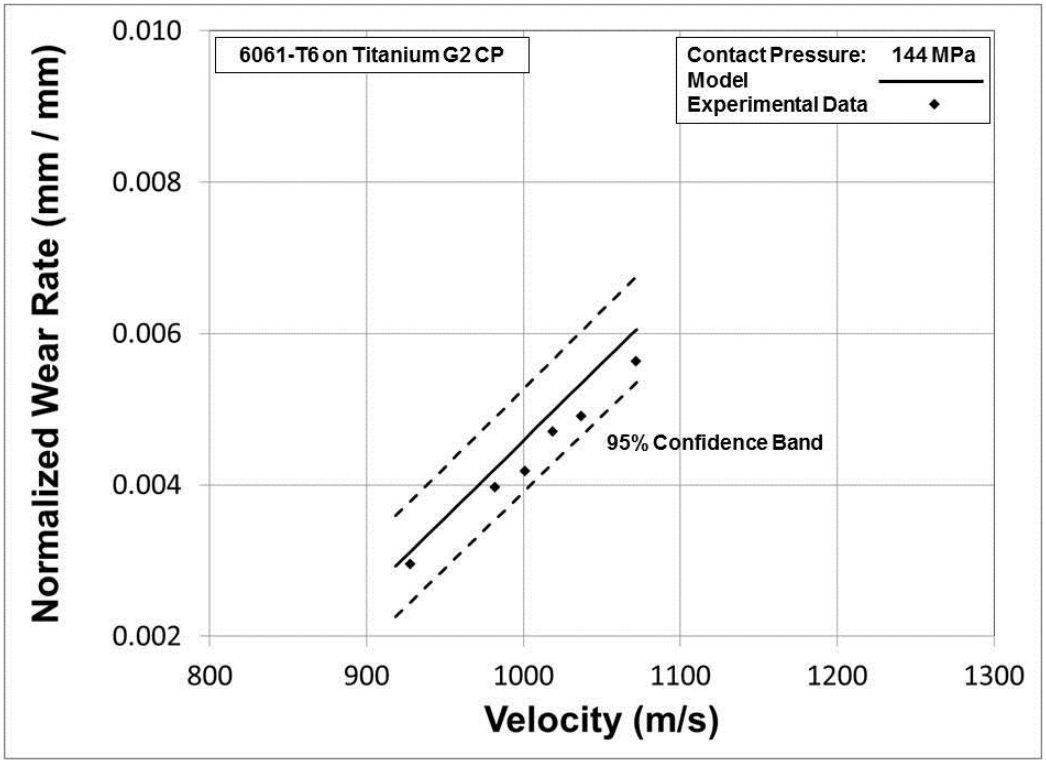
6061-T6 on Titanium G2 CP
Contact Pressure: 144 MPa
Model
Experimental Data
95% Confidence Band
Normalized Wear Rate (mm / mm)
0.010
0.008
0.006
0.004
0.002
800
900
1000
1100
1200
1300
Velocity (m/s)

APPENDIX C

Test No.	Tribomaterial Pairing		Length (mm)	Width (mm)	Location (cm)	Contact Pressure (Mpa)	Velocity (m/s)	Normalized Wear (mm/mm)	Error (95 % Confidence Interval)	Type of Wear
	Slider	Guider								
1	6061-T6	C110-H2	3.15	3.15	26.2	101	926	5.06E-03	2.97E-04	Severe Plastic Deformation Region
					28.5	101	966	3.98E-03	1.89E-04	
					31.5	101	1015	3.10E-03	1.28E-04	
					32.5	101	1031	2.81E-03	3.81E-04	
					---	101	1039	2.67E-03	---	Critical Velocity
					35	101	1070	3.16E-03	3.30E-04	Melt Lubrication
					38.5	101	1122	4.18E-03	2.99E-04	
					40	101	1144	4.54E-03	8.63E-04	
					45	101	1213	5.63E-03	1.88E-04	
2	6061-T6	C110-H2	2.41	2.44	31	122	930	3.70E-03	1.78E-04	Severe Plastic Deformation Region
					32	122	945	3.48E-03	1.91E-04	
					36	122	1003	2.61E-03	2.48E-04	
					---	122	1012	2.52E-03	---	Critical Velocity
					37	122	1017	2.64E-03	1.88E-04	Melt Lubrication
					40	122	1057	3.37E-03	1.61E-04	
					44	122	1109	4.48E-03	2.98E-04	
					50	122	1182	5.67E-03	4.24E-04	
3	6061-T6	C110-H2	3.15	3.18	29.5	124	972	3.47E-03	1.86E-04	
					30.5	124	988	2.63E-03	1.46E-04	
					---	124	992	2.44E-03	---	Critical Velocity
					33.2	124	1031	3.06E-03	1.65E-04	Melt Lubrication
					36	124	1074	4.13E-03	3.13E-04	
					40	124	1132	5.04E-03	6.06E-04	
					42	124	1160	5.54E-03	3.85E-04	
					45.3	124	1205	6.43E-03	2.92E-04	

Test No.	Tribomaterial Pairing		Length (mm)	Width (mm)	Location (cm)	Contact Pressure (Mpa)	Velocity (m/s)	Normalized Wear (mm/mm)	Error (95 % Confidence Interval)	Type of Wear
	Slider	Guider								
4	6061-T6	C110-H2	3.15	3.15	30	130	955	5.59E-03	2.57E-04	
					32	130	986	3.92E-03	2.64E-04	
					---	130	1001	3.13E-03	---	Critical Velocity
					34.8	130	1029	3.71E-03	1.66E-03	Melt Lubrication
					38.6	130	1083	4.46E-03	2.31E-04	
					45.2	130	1172	6.29E-03	2.06E-04	
					46.8	130	1193	6.74E-03	4.86E-04	
5	6061-T6	C110-H2	3.15	3.18	22.5	225	856	6.23E-03	2.48E-04	Severe Plastic Deformation Region
					23.7	225	878	3.65E-03	4.60E-04	
					---	225	879	3.20E-03	---	Critical Velocity
					26.1	225	922	4.28E-03	1.78E-04	Melt Lubrication
					28.5	225	963	4.86E-03	5.19E-04	
					30	225	988	5.32E-03	2.42E-04	
					33.8	225	1049	6.79E-03	2.36E-04	
					38.5	225	1119	8.11E-03	2.66E-04	
					40	225	1141	8.84E-03	1.44E-04	
					42.5	225	1176	9.60E-03	3.32E-04	
6	6061-T6	1045 Steel	3.15	3.15	26	135	952	6.51E-03	1.67E-04	Severe Plastic Deformation Region
					27	135	970	5.78E-03	5.37E-04	
					29	135	1005	3.35E-03	1.90E-04	
					---	135	1018	2.63E-03	---	Critical Velocity
					31	135	1039	3.05E-03	5.82E-04	Melt Lubrication
					32	135	1056	3.35E-03	2.13E-04	
					36	135	1120	4.49E-03	7.02E-04	
					37	135	1136	4.93E-03	6.60E-04	

Test No.	Tribomaterial Pairing		Length (mm)	Width (mm)	Location (cm)	Contact Pressure (Mpa)	Velocity (m/s)	Normalized Wear (mm/mm)	Error (95 % Confidence Interval)	Type of Wear
	Slider	Guider								
7	6061-T6	1018 Steel	3.15	3.18	25	134	931	6.82E-03	1.06E-03	Severe Plastic Deformation Region
					26	134	950	6.00E-03	2.65E-04	
					28	134	985	3.33E-03	2.56E-04	
					---	134	1001	2.42E-03	---	Critical Velocity
					31	134	1037	3.01E-03	2.05E-04	Melt Lubrication
					35	134	1102	4.12E-03	2.82E-04	
					36	134	1117	4.48E-03	5.02E-04	
					38	134	1148	5.03E-03	5.17E-04	
8	6061-T6	Titanium CP G2	3.15	3.15	18	144	817	5.47E-03	2.10E-04	Severe Plastic Deformation Region
					19	144	839	4.83E-03	1.80E-04	
					23	144	923	3.14E-03	2.62E-04	
					---	144	928	2.95E-03	---	Critical Velocity
					26	144	982	3.97E-03	2.82E-04	Melt Lubrication
					27	144	1001	4.18E-03	4.94E-04	
					28	144	1019	4.70E-03	4.40E-04	
					29	144	1037	4.90E-03	2.43E-04	
					31	144	1072	5.63E-03	9.13E-04	

REFERENCES

[1] R. W. Fox and A. T. McDonald, *Introduction to Fluid Mechanics*, 3rd ed. New York: Wiley, 1985.

[2] B. R. Munson, D. F. Young, and T. H. Okiishi, *Fundamentals of Fluid Mechanics*, 5th ed. Hoboken, NJ: J. Wiley & Sons, 2006.

[3] F. Stefani and J. V. Parker, "Experiments to Measure Gouging Threshold Velocity for Various Metals against Copper," *IEEE Transactions on Magnetics,* vol. 35, pp. 312-316, Jan 1999.

[4] F. Stefani and J. V. Parker, "Experiments to Measure Wear in Aluminum Armatures," *IEEE Transactions on Magnetics,* vol. 35, pp. 100-106, Jan 1999.

[5] "Granta Ces 2013," 12.2.13 ed. Cambridge, UK: Granta Design Limited, 2013.

[6] A. T. Dinsdale and P. N. Quested, "The Viscosity of Aluminium and Its Alloys - a Review of Data and Models," *Journal of Materials Science,* vol. 39, pp. 7221-7228, Dec 15 2004.

[7] T. Iida and R. I. L. Guthrie, *The Physical Properties of Liquid Metals*. Oxford: Clarendon Press, 1988.

[8] F. P. Bowden and P. A. Persson, "Deformation, Heating and Melting of Solids in High-Speed Friction," *Proceedings of the Royal Society of London Series A-Mathematical and Physical Sciences,* vol. 260, pp. 433-&, 1961.

[9] W. D. Callister, *Materials Science and Engineering : An Introduction*, 6th ed. New York, NY: John Wiley & Sons, 2003.

[10] S. C. Lim and M. F. Ashby, "Wear-Mechanism Maps," *Acta Metallurgica,* vol. 35, pp. 1-24, Jan 1987.

[11] F. P. Bowden and T. P. Hughes, "The Mechanism of Sliding on Ice and Snow," *Proceedings of the Royal Society of London Series a-Mathematical and Physical Sciences,* vol. 172, pp. 0280-0298, Aug 1939.

[12] F. P. Bowden and E. H. Freitag, "Friction of Solids at High Speeds," *Nature,* vol. 176, pp. 944-946, 1955.

[13] R. S. Montgomery, "Friction and Wear at High Sliding Speeds," *Wear,* vol. 36, pp. 275-298, 1976.

[14] B. Bhushan, *Introduction to Tribology*. New York: John Wiley & Sons, 2002.

[15] Y. Liu, R. Asthana, and P. Rohatgi, "A Map for Wear Mechanisms in Aluminum-Alloys," *Journal of Materials Science,* vol. 26, pp. 99-102, Jan 1 1991.

[16] D. Dowson, *History of Tribology*, 2nd ed. London: Professional Engineering Publishing, 1998.

[17] "Lubrication (Tribology) Education and Research. A Report on the Present Position and Industry's Needs," D. o. E. a. Science, Ed., ed. London: HMSO, 1966.

[18] O. Pinkus, D. F. Wilcock, American Society of Mechanical Engineers. Research Committee on Lubrication., and Mechanical Technology Incorporated. Tribology Department., *Strategy for Energy Conservation through Tribology*. New York: American Society of Mechanical Engineers, 1977.

[19] B. Bhushan, *Tribology and Mechanics of Magnetic Storage Devices*, 2nd ed. New York: Springer, 1996.

[20] H. P. Jost, "Tribology Micro & Macro Economics: A Road to Economic Savings," *Tribology & Lubrication Technology,* vol. 61, pp. 18-22, Oct 2005.
[21] S. Kalpakjian and S. R. Schmid, *Manufacturing Processes for Engineering Materials*, 5th ed. Upper Saddle River, N.J.: Pearson Education, 2008.
[22] K. F. Graff and B. B. Dettloff, "Gouging Phenomenon between Metal Surfaces at Very High Sliding Speeds," *Wear,* vol. 14, pp. 87-97, 1969.
[23] H. D. Fair, "Advances in Electromagnetic Launch Science and Technology and Its Applications," *IEEE Transactions on Magnetics,* vol. 45, pp. 225-230, Jan 2009.
[24] O. Reynolds, *Papers on Mechanical and Physical Subjects* vol. 2. Cambridge Eng.: The University Press, 1901.
[25] F. P. Bowden, "Friction on Snow and Ice and the Development of Some Fast-Running Skis," *Nature,* vol. 176, pp. 946-947, 1955.
[26] F. P. Bowden and K. E. W. Ridler, "Physical Properties of Surfaces. Iii. The Surface Temperature of Sliding Metals the Temperature of Lubricated Surfaces," *Proceedings of the Royal Society of London Series A-Mathematical and Physical Sciences,* vol. 154, pp. 640-656, May 1936.
[27] F. P. Bowden and T. P. Hughes, "Physical Properties of Surfaces. Iv. Polishing, Surface Flow and the Formation of the Beilby Layer," *Proceedings of the Royal Society of London Series A-Mathematical and Physical Sciences,* vol. 160, pp. 0575-0587, Jun 1937.
[28] J. W. Beams, "High Centrifugal Fields," *Journal of the Washington Academy of Sciences,* vol. 37, pp. 221-241, July 15, 1947 1947.
[29] F. P. Bowden and E. H. Freitag, "The Friction of Solids at Very High Speeds .1. Metal on Metal .2. Metal on Diamond," *Proceedings of the Royal Society of London Series A-Mathematical and Physical Sciences,* vol. 248, pp. 350-&, 1958.
[30] H. S. Carslaw and J. C. Jaeger, *Conduction of Heat in Solids*. Oxford Eng.: Clarendon Press, 1947.
[31] B. Sternlicht and H. Apkarian, "Investigation of Melt Lubrication," *ASLE Transactions,* vol. 2, p. 248, 1960.
[32] S. W. E. Earles and M. J. Kadhim, "Friction and Wear of Unlubricated Steel Surfaces at Speeds up to 665 Ft/S," *Proceedings of the Institution of Mechanical Engineers,* vol. 180, pp. 531-548, 1965.
[33] F. P. Bowden and P. H. Thomas, "The Surface Temperature of Sliding Solids," *Proceedings of the Royal Society of London Series A-Mathematical and Physical Sciences,* vol. 223, 1954.
[34] W. R. D. Wilson, "Lubrication by a Melting Solid," *Journal of Lubrication Technology-Transactions of the ASME,* vol. 98, pp. 22-26, 1976.
[35] V. Bicego, A. Figari, and G. Poletti, "Lubrication of a Melting Slider under Non-Isothermal Conditions," *Journal of Lubrication Technology-Transactions of the ASME,* vol. 103, pp. 436-442, 1981.
[36] A. K. Stiffler, "Friction and Wear with a Fully Melting Surface," *Journal of Tribology-Transactions of the ASME,* vol. 106, pp. 416-419, 1984.
[37] P. B. Parks, "Current Melt-Wave Model for Transitioning Solid Armature," *Journal of Applied Physics,* vol. 67, pp. 3511-3516, Apr 1 1990.

[38] J. P. Barber, A. Challita, B. Maas, and L. Thurmond, "Contact Transition in Metal Armatures," *IEEE Transactions on Magnetics,* vol. 27, pp. 228-232, Jan 1991.
[39] J. P. Barber and Y. A. Dreizin, "Model of Contact Transitioning with Realistic Armature-Rail Interface," *IEEE Transactions on Magnetics,* vol. 31, pp. 96-100, Jan 1995.
[40] L. C. Woods, "The Current Melt-Wave Model," *IEEE Transactions on Magnetics,* vol. 33, pp. 152-156, Jan 1997.
[41] R. E. Kothmann and F. Stefani, "A Thermal Hydraulic Model of Melt-Lubrication in Railgun Armatures," *IEEE Transactions on Magnetics,* vol. 37, pp. 86-91, Jan 2001.
[42] R. Merrill and F. Stefani, "A Turbulent Melt-Lubrication Model of Surface Wear in Railgun Armatures," *IEEE Transactions on Magnetics,* vol. 41, pp. 414-419, Jan 2005.
[43] Z. G. Wei and R. C. Batra, "Modeling and Simulation of High Speed Sliding," *International Journal of Impact Engineering,* vol. 37, pp. 1197-1206, Dec 2010.
[44] S. Bair, R. Cowan, G. Kennedy, R. Neu, M. Siopis, J. Streator, and N. Thadhani, "A Survey of Railgun Research at the Georgia Institute of Technology (USA)," *2012 16th International Symposium on Electromagnetic Launch Technology (EML),* 2012.
[45] D. Halliday, R. Resnick, and J. Walker, *Fundamentals of Physics*, 6th ed. New York: Wiley, 2001.
[46] B. Chung, "Finite-Element Analysis of Physical Phenomena of a Lab-Scale Electromagnetic Launcher," Masters, Georgia Institute of Technology, Atlanta, GA, 2007.
[47] N. S. M. El-Tayeb, B. F. Yousif, and P. V. Brevern, "On the Effect of Counterface Materials on Interface Temperature and Friction Coefficient of Gfre Composite under Dry Sliding Contact," *American Journal of Applied Sciences,* vol. 2, pp. 1533-1540, 2005.
[48] J. V. Parker, "Magnetic-Probe Diagnostics for Railgun Plasma Armatures," *IEEE Transactions on Plasma Science,* vol. 17, pp. 487-500, Jun 1989.
[49] B. J. Evans and L. M. Smith, "Determining Railgun Plasma Current Distribution Using Jansson Method to Deconvolve B-Dot Probe Signals," *IEEE Transactions on Plasma Science,* vol. 20, pp. 432-438, Aug 1992.
[50] Z. J. Wang, J. J. He, S. G. Xia, Z. Xiao, L. X. Chen, Z. Cheng, M. L. Dong, J. Li, and P. Yan, "Evaluation of Solid Armature's in-Bore Position, Velocity, and Current Distribution Using B-Dot Probes in Railgun Experiments," *IEEE Transactions on Magnetics,* vol. 45, pp. 485-489, Jan 2009.
[51] M. Podlesak, "Rogowski Coil Calibration on a Capacitive Discharge Rig without the Use of a Current Reference," *Review of Scientific Instruments,* vol. 61, pp. 892-896, Feb 1990.
[52] J. F. Archard, "Contact and Rubbing of Flat Surfaces," *Journal of Applied Physics,* vol. 24, pp. 981-988, 1953.
[53] R. Holm and A. V. Heijne, *Electric Contacts*. Stockholm,: H. Geber, 1946.
[54] U. Sanchez-Santana, C. Rubio-Gonzalez, G. Gomez-Rosas, J. L. Ocana, C. Molpeceres, J. Porro, and M. Morales, "Wear and Friction of 6061-T6 Aluminum

Alloy Treated by Laser Shock Processing," *Wear,* vol. 260, pp. 847-854, Apr 7 2006.
[55] R. W. Goldman, A. E. Segall, and J. C. Conway, "The Dry Sliding Behavior of Aluminum Alloys against Steel in Sheave Wheel Applications," *Journal of Tribology-Transactions of the ASME,* vol. 123, pp. 676-681, Oct 2001.
[56] N. P. Suh, "Delamination Theory of Wear," *Wear,* vol. 25, pp. 111-124, 1973.
[57] R. Stribeck, "Fundamental Characteristics of the Friction Bearing and the Roller Bearing.," *Zeitschrift Des Vereines Deutscher Ingenieure,* vol. 46, pp. 1341-1348, 1902.
[58] R. G. Budynas, J. K. Nisbett, and J. E. Shigley, *Shigley's Mechanical Engineering Design*, 8th ed. Boston: McGraw-Hill, 2008.
[59] R. L. Norton, *Machine Design : An Integrated Approach*, 2nd ed. Upper Saddle River, N.J.: Prentice Hall, 2000.
[60] A. Cameron, *Basic Lubrication Theory,* 2d ed. Chichester: E. Horwood, 1976.
[61] W. A. Gross and W. A. Gross, *Fluid Film Lubrication*. New York: Wiley, 1980.
[62] R. M. Gee and C. Persad, "The Response of Different Copper Alloys as Rail Contacts at the Breech of an Electromagnetic Launcher," *IEEE Transactions on Magnetics,* vol. 37, pp. 263-268, Jan 2001.
[63] K. P. Cooper, H. N. Jones, and R. A. Meger, "Analysis of Railgun Barrel Material," *IEEE Transactions on Magnetics,* vol. 43, pp. 120-125, Jan 2007.
[64] I. R. McNab, M. T. Crawford, S. S. Satapathy, F. Stefani, and T. J. Watt, "Iat Armature Development," *IEEE Transactions on Plasma Science,* vol. 39, pp. 442-451, Jan 2011.
[65] F. Stefani, M. Crawford, D. Melton, and T. Watt, "Experiments with Armature Contact Claddings," *IEEE Transactions on Magnetics,* vol. 43, pp. 413-417, Jan 2007.
[66] J. V. Parker, D. T. Berry, and P. T. Snowden, "The Iat Electromagnetic Launch Research Facility," *IEEE Transactions on Magnetics,* vol. 33, pp. 129-133, Jan 1997.
[67] G. G. Hirs, "Bulk-Flow Theory for Turbulence in Lubricant Films," *Journal of Lubrication Technology-Transactions of the ASME,* vol. 95, pp. 137-146, 1973.
[68] N. E. Dowling, *Mechanical Behavior of Materials : Engineering Methods for Deformation, Fracture, and Fatigue,* 3rd ed. Upper Saddle River, N.J.: Pearson/Prentice Hall, 2007.
[69] J. C. Jaeger, "Moving Sources of Heat and the Temperature at Sliding Contacts," *Journal and Proceedings of the Royal Society of New South Wales,* vol. 76, p. 22, 1943.
[70] H. Blok, "Theoretical Study of Temperature Rise at Surfaces of Actual Contact under Oiliness Lubricating Conditions," *Proceedings of the Institute of Mechanical Engineers General Discussion of Lubrication,* vol. 2, pp. 222-235, 1937.
[71] D. Bansal, "Tribological Investigations of Electrical Contacts," PhD, Georgia Institute of Technology, Atlanta, GA, 2009.
[72] F. P. Incropera and D. P. DeWitt, *Introduction to Heat Transfer*, 4th ed. New York: Wiley, 2002.

[73] J. F. Archard, "The Temperature of Rubbing Surfaces," *Wear,* vol. 2, pp. 438-455, 1958.
[74] A. K. Stiffler, "Projectile Sliding Forces in a Rifled Barrel," *International Journal of Mechanical Sciences,* vol. 25, pp. 105-119, 1983.
[75] J. P. Barber and D. P. Bauer, "Contact Phenomena at Hypervelocities," *Wear,* vol. 78, pp. 163-169, 1982.
[76] K. R. Tarcza and W. F. Weldon, "Metal Gouging at Low Relative Sliding Velocities," *Wear,* vol. 209, pp. 21-30, Aug 1997.
[77] T. Watt and D. T. Motes, "The Effects of Surface Coatings on the Onset of Rail Gouging," *IEEE Transactions on Plasma Science,* vol. 39, pp. 168-173, Jan 2011.
[78] T. J. Watt and D. L. Bourell, "Sliding Instabilities and Hypervelocity Gouging," *IEEE Transactions on Plasma Science,* vol. 39, pp. 162-167, Jan 2011.
[79] J. R. Asay and M. Shahinpoor, *High-Pressure Shock Compression of Solids*. New York: Springer-Verlag, 1993.
[80] R. S. Montgomery, "Muzzle Wear of Cannon," *Wear,* vol. 33, pp. 359-368, 1975.
[81] R. S. Montgomery and F. K. Sautter, "A Review of Recent American Work on Gun Erosion and Its Control," *Wear,* vol. 94, pp. 193-199, 1984.
[82] R. H. Carter, J. H. Underwood, J. J. Swab, A. A. Wereszczak, C. Leveritt, R. Emerson, and L. Burton, "Material Selection for Ceramic Gun Tube Liner," *Materials and Manufacturing Processes,* vol. 21, pp. 584-590, Aug 2006.
[83] R. S. Montgomery, "Evidence for the Melt-Lubrication of Projectile Bands," *ASLE Transactions,* vol. 28, pp. 117-122, 1985.
[84] R. A. Meger, K. Cooper, H. Jones, J. Neri, S. Qadri, I. L. Singer, J. Sprague, and K. J. Wahl, "Analysis of Rail Surfaces from a Multishot Railgun," *IEEE Transactions on Magnetics,* vol. 41, pp. 211-213, Jan 2005.
[85] T. Watt, F. Stefani, M. Crawford, H. Mark, and J. Parker, "Investigation of Damage to Solid-Armature Railguns at Startup," *IEEE Transactions on Magnetics,* vol. 43, pp. 214-218, Jan 2007.
[86] C. Persad, "Railgun Tribology - Chemical Reactions between Contacts," *IEEE Transactions on Magnetics,* vol. 43, pp. 391-396, Jan 2007.
[87] C. Persad, C. J. Lund, Z. Eliezer, D. R. Peterson, J. Hahne, and R. Zowarka, "Wear of Conductors in Railguns - Metallurgical Aspects," *IEEE Transactions on Magnetics,* vol. 25, pp. 433-437, Jan 1989.
[88] J. H. Underwood, G. N. Vigilante, and C. P. Mulligan, "Review of Thermo-Mechanical Cracking and Wear Mechanisms in Large Caliber Guns," *Wear,* vol. 263, pp. 1616-1621, Sep 10 2007.
[89] J. H. Underwood, A. P. Parker, G. N. Vigilante, and P. J. Cote, "Thermal Damage, Cracking and Rapid Erosion of Cannon Bore Coatings," *Journal of Pressure Vessel Technology-Transactions of the ASME,* vol. 125, pp. 299-304, Aug 2003.
[90] J. H. Underwood, M. D. Witherell, S. Sopok, J. C. McNeil, C. P. Mulligan, and G. N. Vigilante, "Thermomechanical Modeling of Transient Thermal Damage in Cannon Bore Materials," *Wear,* vol. 257, pp. 992-998, Nov 2004.
[91] A. G. Evans and J. W. Hutchinson, "The Thermomechanical Integrity of Thin-Films and Multilayers," *Acta Metallurgica et Materialia,* vol. 43, pp. 2507-2530, Jul 1995.

[92] G. R. Colombo, M. Otooni, M. P. Evangelisti, N. Colon, and E. Chu, "Application of Coatings for Electromagnetic Gun Technology," *IEEE Transactions on Magnetics*, vol. 31, pp. 704-708, Jan 1995.
[93] Z. Castro-Dettmer, R. M. Gee, and C. Persad, "Post-Test Characterization of a Chromium-Plated Copper Conductor," *Materials Characterization*, vol. 43, pp. 251-258, Oct 1999.
[94] M. F. Ashby, *Materials Selection in Mechanical Design*, 4th ed. Burlington, MA: Butterworth-Heinemann, 2011.